

---

# Laser System Technology for Quantum Experiments in Space and beyond

---

Dissertation

zur Erlangung des akademischen Grades  
„Doktor der Naturwissenschaften“

am Fachbereich Physik, Mathematik und Informatik  
der Johannes Gutenberg-Universität  
in Mainz

vorgelegt von  
**Moritz Mihm, M. Sc.**  
geb. in Kassel

Mainz, den 31. August 2020



---

## Abstract

---

Moritz Mihm

### Laser System Technology for Quantum Experiments in Space and beyond

This thesis includes technologies and techniques for the development of compact and robust laser systems for use in harsh environments, e.g. in space. Since the first laser was launched into space on Apollo 15 almost 50 years ago, laser technologies have been established for space applications such as optical communication, remote sensing, or quantum technologies. Many of the quantum technology applications are based on cold atom experiments and rely on laser systems, i.e. not only on laser light sources, but also on optical systems for beam guidance and manipulation. Operating a quantum apparatus in harsh environments places high demands on the experiment and especially the laser system in terms of mechanical and thermal stability. In addition, the systems typically have size, weight, and power budget restrictions.

For this purpose, I present developments that advance the state of the art towards more compact laser systems. In the framework of the underlying technology, fiber-coupled optical modules are assembled by mounting free-space optics on a baseplate made of Zerodur, a glass ceramic with vanishing coefficient of thermal expansion. To reduce the package size, I introduce an optical element which allows one to separate superimposed beams of different diffraction orders directly behind acousto-optic modulators, whereas the conventional approach of spatial separation requires a beam path of the order of at least 10 cm. The element was first implemented on the optical modules for the sounding rocket missions MAIUS-2 and MAIUS-3. During the approximately 6 min in reduced gravity on each flight, atom interferometry is performed with Bose-Einstein condensates of potassium and rubidium to test the weak equivalence principle. A further reduction of the package size is possible by implementing the technique presented for simultaneous laser frequency stabilization on transitions of multiple atomic species with a single optical setup. The method enables one to develop versatile and compact frequency reference modules for multi-species experiments.

Paving the way to fully integrated quantum optical systems, I also discuss efforts to build flange-less vacuum systems based on Zerodur. By combining vacuum chambers with the modular laser system technology, a platform for robust and compact quantum sensor applications is created.

With space-qualified technology also being suitable for other applications in harsh environments, I further present an optical module for transportable optical clocks. As this example demonstrates, there are numerous applications that would benefit from the advantages of the technologies and techniques presented – in space and beyond.



---

## Publications

---

### Scientific publications

1. **Mihm, M.**, K. Lampmann, A. Wenzlawski, and P. Windpassinger: ‘Simultaneous modulation transfer spectroscopy on transitions of multiple atomic species for compact laser frequency reference modules’. *Review of Scientific Instruments* (2018), vol. 89(9): p. 096101. DOI: 10.1063/1.5041782.
2. Frye, K., S. Abend, W. Bartosch, A. Bawamia, D. Becker, H. Blume, C. Braxmaier, S.-W. Chiow, M. A. Efremov, W. Ertmer, P. Fierlinger, N. Gaaloul, J. Grosse, C. Grzeschik, O. Hellmig, V. A. Henderson, W. Herr, U. Israelsson, J. Kohel, M. Krutzik, C. Kürbis, C. Lämmerzahl, M. List, D. Lüdtke, N. Lundblad, J. P. Marburger, M. Meister, **M. Mihm**, H. Müller, H. Müntinga, T. Oberschulte, A. Papakonstantinou, J. Perovšek, A. Peters, A. Prat, E. M. Rasel, A. Roura, W. P. Schleich, C. Schubert, S. T. Seidel, J. Sommer, C. Spindeldreier, D. Stamper-Kurn, B. K. Stuhl, M. Warner, T. Wendrich, A. Wenzlawski, A. Wicht, P. Windpassinger, N. Yu, and L. Wörner: *The Bose-Einstein Condensate and Cold Atom Laboratory*. Submitted for publication in European Physical Journal Quantum Technology. 2019. arXiv: 1912.04849 [physics.atom-ph].
3. **Mihm, M.**, O. Hellmig, A. Wenzlawski, K. Sengstock, and P. Windpassinger: ‘Highly angular resolving beam separator based on total internal reflection’. *Appl. Opt.* (July 2019), vol. 58(21): pp. 5770–5773. DOI: 10.1364/AO.58.005770.
4. **Mihm, M.**, J. P. Marburger, A. Wenzlawski, O. Hellmig, O. Anton, K. Döringshoff, M. Krutzik, A. Peters, P. Windpassinger, and the MAIUS Team: ‘ZERODUR® based optical systems for quantum gas experiments in space’. *Acta Astronautica* (2019), vol. 159: pp. 166–169. DOI: 10.1016/j.actaastro.2019.03.060.
5. Döringshoff, K., **M. Mihm**, A. Wenzlawski, O. Hellmig, and C. Kürbis: *Laser system for dual species atom-interferometry with Rubidium and Potassium on a sounding rocket*. In preparation. 2020.
6. Elsen, M., B. Piest, O. Anton, W. Bartosch, D. Becker, J. Boehm, K. Döringshoff, J. Grosse, O. Hellmig, C. Kürbis, M. Koch, M. D. Lachmann, **M. Mihm**, H. Müntinga, A. Pratisala, J. Perovsek, J. Sommer, M. Warner, T. Wendrich, T. Oberschulte, C. Spindeldreier, A. Wenzlawski, C. Braxmaier, M. Krutzik, C. Lämmerzahl, D. Lüdtke, A. Peters, E. M. Rasel, K. Sengstock, A. Wicht, P. Windpassinger, and H. Blume: *Towards a Dual-Species Atom Interferometer Payload for Operation on Sounding Rockets*. In preparation. 2020.

7. Hannig, S., B. Kraus, **M. Mihm**, A. Wenzlawski, O. Hellmig, P. Windpassinger, K. Sengstock, and P. O. Schmidt: *Zerodur-based Optical Systems for Transportable Quantum Sensors in the UV*. In preparation. 2020.
8. Marburger, J. P., C. Korn, **M. Mihm**, O. Hellmig, A. Wenzlawski, and P. Windpassinger: *Determining the stability and coupling efficiency degradation of ultra-stable optical benches under load*. Submitted for publication in Review of Scientific Instruments. 2020.

#### Submissions to international conferences

1. **Mihm, M.**, K. Lampmann, A. Wenzlawski, K. Döringshoff, M. Krutzik, A. Peters, and P. Windpassinger: ‘Zerodur-based optical systems for dual-species atom interferometry in space’. *Young Atom Opticians conference*. Munich and Garching, Germany, 2016.
2. Anton, O., K. Döringshoff, V. Schkolnik, S. Kanthak, C. Kürbis, J. Große, M. Elsen, A. Wenzlawski, **M. Mihm**, P. Windpassinger, M. Krutzik, and A. Peters: ‘Design of a compact diode laser system for dual-species atom interferometry with rubidium and potassium in space’. *2017 Conference on Lasers and Electro-Optics Pacific Rim (CLEO-PR)*. Singapore, Singapore, July 2017: pp. 1–4. DOI: 10.1109/CLEOPR.2017.8119018.
3. Adams, B., D. Gancheva, J. Hooper, and **M. Mihm**: ‘Space Ready: The Launchpad for Emerging Agencies’. *International Astronautical Congress (IAC)*. Bremen, Germany, 2018.
4. Marburger, P., **M. Mihm**, O. Hellmig, A. Wenzlawski, and P. Windpassinger: ‘Highly stable Zerodur based optical benches for microgravity applications and other adverse environments’. *International Conference on Space Optics (ICSO)*. Chania, Greece, 2018.
5. **Mihm, M.**, P. Marburger, A. Wenzlawski, O. Hellmig, O. Anton, K. Döringshoff, M. Krutzik, A. Peters, and P. Windpassinger: ‘Zerodur based optical systems for quantum gas experiments in space’. *International Astronautical Congress (IAC)*. Bremen, Germany, 2018.
6. **Mihm, M.**, S. Boles, P. Marburger, A. Wenzlawski, O. Hellmig, and P. Windpassinger: ‘Stable optical and vacuum systems for quantum technology applications in space’. *International Astronautical Congress (IAC)*. Washington, D.C., United States, 2019.
7. Piest, B., M. D. Lachmann, O. Anton, W. Bartosch, D. Becker, J. Böhm, K. Döringshoff, M. Elsen, J. Grosse, C. Kürbis, **M. Mihm**, M. Popp, T. Wendrich, A. Wenzlawski, C. Braxmeier, W. Ertmer, M. Krutzik, C. Lämmerzahl, A. Peters, A. Wicht, P. Windpassinger, and E. M. Rasel: ‘MAIUS-B: A system for two-species atom interferometry in space’. *ESA Symposium on European ROCKET & BALLOON programmes and related research*. Essen, Germany, 2019.

8. Schneider, S., **M. Mihm**, E. Madden, M. Davis, B. Adams, and T. Ryan: 'A Reunion for Colleagues, a Platform for Experts, an Opportunity for Stakeholders: The International Space University Adelaide Conference for Idea Exchange and Public Engagement'. *International Astronautical Congress (IAC)*. Cyberspace Edition, 2020.





---

# Contents

---

<b>1</b>	<b>Introduction</b>	<b>1</b>
1.1	Matter wave interferometry . . . . .	2
1.2	Matter wave interferometry in microgravity . . . . .	5
1.3	Joint research effort QUANTUS . . . . .	7
1.4	Outline of this thesis . . . . .	8
<b>2</b>	<b>Sounding rocket missions MAIUS-2 and MAIUS-3</b>	<b>11</b>
2.1	Conceptual experiment requirements . . . . .	11
2.2	Suborbital flight . . . . .	12
2.2.1	Launch vehicle . . . . .	12
2.2.2	Flight events . . . . .	13
2.2.3	Environmental conditions during flight . . . . .	14
2.3	Scientific payload . . . . .	16
2.3.1	Electronic systems . . . . .	17
2.3.2	Physics package . . . . .	17
2.4	Qualification procedure . . . . .	19
<b>3</b>	<b>Laser system for MAIUS-2/-3</b>	<b>21</b>
3.1	System functions and schematic structure . . . . .	21
3.2	System architecture . . . . .	24
3.3	Zerodur technology . . . . .	25
3.4	Zerodur-based optical modules . . . . .	26
3.4.1	Scientific modules . . . . .	28
3.4.2	Frequency reference modules . . . . .	32
3.5	Separating superimposed beams which only differ in angle . . . . .	38
<b>4</b>	<b>Technology development for future applications</b>	<b>41</b>
4.1	Simultaneous spectroscopy on transitions of multiple atomic species . . . . .	41
4.2	Zerodur-based vacuum systems . . . . .	45
4.2.1	Zerodur vacuum chambers . . . . .	45
4.2.2	Zerodur MOT chamber . . . . .	48
<b>5</b>	<b>Impact</b>	<b>53</b>
5.1	Zerodur-based optical modules for BECCAL . . . . .	53
5.2	Zerodur-based optical module for an $\text{Al}^+/\text{Ca}^+$ quantum logic optical clock . . . . .	54

<b>6 Conclusion and outlook</b>	<b>57</b>
<b>Publications</b>	<b>61</b>
<b>Bibliography</b>	<b>79</b>
<b>Appendix</b>	<b>95</b>
<b>A Main flight events</b>	<b>95</b>
<b>Curriculum vitae</b>	<b>97</b>

---

## Abbreviations and acronyms

---

<b>Notation</b>	<b>Description</b>
AMD	alkali metal dispenser
AOM	acousto-optic modulator
AR	anti-reflection
ARCS	attitude and rate control system
BEC	Bose-Einstein condensate
BECCAL	Bose-Einstein Condensate and Cold Atom Laboratory
CAD	computer-aided design
CAL	Cold Atom Laboratory
CCD	charge-coupled device
CDR	critical design review
CF	ConFlat
CTE	coefficient of thermal expansion
DDS	direct digital synthesis
DFB	distributed feedback
DKC	delta-kick collimation
DLR	Deutsches Zentrum für Luft- und Raumfahrt e. V.
DPS	differential pumping stage
ECDL	extended cavity diode laser
EOM	electro-optic modulator
FBH	Ferdinand-Braun-Institut, Leibniz-Institut für Höchstfrequenz-technik
FMS	frequency modulation spectroscopy

---

---

<b>Notation</b>	<b>Description</b>
FOKUS	Faserlaser basierter optischer Kammgenerator unter Schwerelosigkeit
GSE	ground support equipment
HUB	Humboldt-Universität zu Berlin
HV	high vacuum
HWP	half-wave plate
ICE	interférométrie atomique à sources cohérentes pour l'espace
iIPD	inline photodiode
ISS	International Space Station
JGU	Johannes Gutenberg University Mainz
JOKARUS	Jod Kamm Resonator unter Schwerelosigkeit
KALEXUS	Kalium Laserexperimente unter Schwerelosigkeit
LISA	Laser Interferometer Space Antenna
LLR	lunar laser ranging
LMA	large mode area
LUH	Leibniz University Hannover
MAIUS	Materiewelleninterferometer unter Schwerelosigkeit
MFD	mode field diameter
MICROSCOPE	micro-satellite à traînée compensée pour l'observation du principe d'équivalence
MOPA	master oscillator power amplifier
MOT	magneto-optical trap
MTS	modulation transfer spectroscopy
NEG	non-evaporable getter
NOA	Norland Optical Adhesive
OBST	optical beam steering technique
ODT	optical dipole trap

---

<b>Notation</b>	<b>Description</b>
OI	optical isolator
PBS	polarizing beam splitter
PCB	printed circuit board
PCF	photonic crystal fiber
PM	polarization maintaining
PSD	power spectral density
PTB	Physikalisch-Technische Bundesanstalt
QUANTUS	Quantengase unter Schwerelosigkeit
QWP	quarter-wave plate
RF	radio frequency
SNR	signal-to-noise ratio
SRD	systems requirements document
SSC	Swedish Space Corporation
SWaP	size, weight and power
TEXUS	Technologische Experimente unter Schwerelosigkeit
TUDA	Technical University of Darmstadt
UFF	universality of free fall
UHH	Universität Hamburg
UHV	ultra-high vacuum
ULE	Ultra-Low Expansion
UULM	Ulm University
WEP	weak equivalence principle
ZARM	Zentrum für angewandte Raumfahrttechnologie und Mikrogravitation

---



# CHAPTER 1

---

## Introduction

---

The story of laser technologies for space applications begins on 9 May 1962 with a pulsed beam, focused on the lunar surface and subsequent capturing of the echoes [1]. That is less than two years since Theodore Maiman first realized a laser on 16 May 1960 [2]. However, as the laser was operated from ground, no special requirements such as mechanical or thermal stability had to be met, and it took another nine years for the first laser to take off into space. This first laser in space was a flash-lamp-pumped Ruby laser used in 1971 for the Laser Altimeter experiment on Apollo 15 [3].

Nowadays, laser technologies are ubiquitous thanks to their advantages over traditional light sources such as beam properties, efficiency and low power consumption. Space applications include communication, optical pyrotechnics in propulsion and science, with important scientific applications being remote sensing, spectroscopy and quantum technologies [4]. A vast amount of quantum technology applications is based on cold atom experiments, e.g. for tests of the universality of free fall (UFF) [5], detection of gravitational waves [6], or Earth' gravity field monitoring [7].

All these cold atom experiments depend on laser systems, including optical systems for beam guidance and manipulation. Bringing an experiment from the laboratory to the field is a major technological challenge, especially for laser systems with their sensitive optics, as requirements for mechanical and thermal stability as well as size, weight and power (SWaP) constraints have to be met. To this end, I present a technology for robust fiber-coupled optical modules, consisting of Zerodur-based optical benches with free-space optics. The technology provides a complete toolkit that enables one to assemble modules for a variety of functions, including laser frequency stabilization as well as distribution, overlap and switching of laser beams. Although introduced elsewhere [8, 9], I contributed to a significant improvement by developing a new optical element that facilitates ever more compact laser systems. Moreover, I present a technique for frequency reference systems in multi-species experiments with less complexity and susceptibility to failures.

Paving the way to fully integrated, i.e. flange-less, quantum optical systems/sensors, I also showcase current efforts to build Zerodur-based vacuum systems. The combination of miniaturized and robust vacuum chambers with the modular laser system technology allows the development of integrated quantum optical systems for applications outside laboratory environments.

Some of the innovations presented in this thesis were implemented for the first time on the Zerodur-based optical modules for the sounding rocket missions MAIUS-2 and MAIUS-3. Even more, the developments were geared to the requirements of space missions in general and the MAIUS missions in particular, both from a technological and a scientific point of view. The MAIUS missions are designed to test the weak equivalence principle (WEP) during ballistic flights with approximately 6 min in reduced gravity. The weak equivalence principle states that the trajectory of any free-falling object is independent of its internal structure and composition. Violations of the WEP are typically quantified by the Eötvös ratio which compares the free-fall accelerations  $a_A$  and  $a_B$  of two test bodies A and B:

$$\eta = 2 \left| \frac{a_A - a_B}{a_A + a_B} \right|. \quad (1.1)$$

The Eötvös ratio is named after the Hungarian physicist Roland v. Eötvös, who designed a torsion balance to test the WEP without finding any violation [10]. The benchmark for highest precision in WEP tests with respect to the Eötvös ratio is set by torsion balance and lunar laser ranging (LLR), an experiment based on accurate distance information between the Earth and Moon to determine whether they accelerate towards the Sun at the same rate. However, a new type of experiments promises unprecedented precision. This type of experiments also lays the foundation for the sounding rocket mission program, as the acronym MAIUS already suggests: *matter wave interferometer under weightlessness* (ger. Materiewelleninterferometer unter Schwerelosigkeit).

### 1.1 Matter wave interferometry

Atom interferometry has become a versatile tool for testing the WEP, among others. In analogy to an optical light interferometer, the interference pattern of an atom interferometer holds information about the phase difference of atomic matter waves along the different paths. The phase difference in turn depends on the (gravitational) acceleration of the atoms which makes atom interferometry a highly sensitive tool and complementary approach to test the WEP.

The concept of matter waves dates back to 1924, when Louis de Broglie extended Albert Einstein's interpretation of the photoelectric effect to electrons, i.e. massive particles, by attributing wave-like properties and a corresponding wavelength to them [11]. Although wave-like properties have been demonstrated for many types of massive particles, atoms have become the first choice for matter wave interferometry. Atoms offer precise controllability as their internal structure is well understood and can be addressed with electromagnetic fields. Also, the electrical neutrality ensures little interaction with external influences like electric or magnetic fields.

Many atom interferometers conceptually resemble an optical Mach-Zehnder interferometer (see figure 1.1(a) for a space-time diagram), with light and matter changing roles. A laser pulse initially excites half the atoms of an atomic cloud by means of Rabi oscillations [12]. That is, for a pulse duration  $\pi/(2\Omega)$  with Rabi frequency  $\Omega$ , the excitation probability is 50 % (see figure 1.1(b)). The momentum transfer associated with the photon absorption



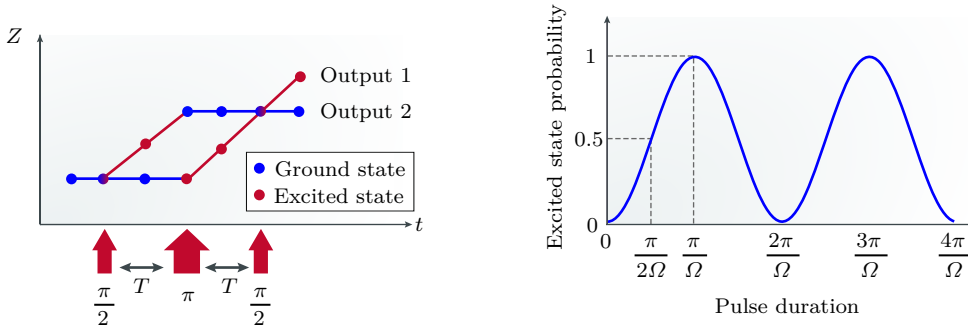
results in a different trajectory of the excited atoms, i.e. the pulse acts as a beamsplitter. Similarly, the following pulse of length  $\pi/\Omega$  after a time  $T$  inverts the population of ground and excited states, thereby acting as a mirror. The associated momentum transfers result in an overlap of both clouds after another time  $T$ . A last pulse with excitation probability 50% (second beamsplitter) mixes the population in both states and thus creates an interference pattern in both output ports. The distribution of atoms in the two states depends sinusoidally on the phase difference  $\Delta\phi$  accumulated along the trajectories. For one of the states, the relative atom number is given by

$$P = \frac{1}{2} [1 + C \cos(\Delta\phi)] , \quad (1.2)$$

where  $C$  is the contrast. The leading order phase shift due to an acceleration  $\vec{a}$  of the atoms along the direction of the laser axis ( $Z$  axis in fig 1.1(a)) reads [13]:

$$\Delta\phi = \vec{k}_{\text{eff}} \cdot \vec{a}T^2 . \quad (1.3)$$

Here  $\vec{k}_{\text{eff}}$  is the effective wavevector (and  $\hbar\vec{k}_{\text{eff}}$  the momentum transfer). In the case of gravitational acceleration, i.e. the different trajectories differ in height, the phase depends on the gravitational potential difference and the atom interferometer becomes a highly sensitive gravity sensor or “gravimeter”. The first gravimeter based on atom interferometry was realized 1991 and the gravitational acceleration of laser-cooled sodium atoms was measured with a resolution of  $3 \times 10^{-6}$  [13]. Since then, work has been done to increase the precision and bring gravimeters out of the laboratory, e.g. for use in the field [14], on ships [15] or on board aircraft [16].



(a) Space-time diagram of an atom interferometer in Mach-Zehnder configuration. The cloud of atoms initially in the ground state is subject to three laser pulses of different interaction times, acting as beamsplitters and mirrors.

(b) Probability of finding a two-level system in the excited state as a function of interaction time with a resonant light field. The system undergoes Rabi oscillations of frequency  $\Omega$ .

**Figure 1.1:** Building blocks of an atom interferometer. Adapted from reference [17].

One can now test the UFF or WEP by comparing the gravitational acceleration of two or more atomic clouds. For that matter, the use of quantum test bodies has several advantages over classical test masses. In addition to the intrinsic isotopic purity, the test

bodies can also be based on atomic elements which might not be usable for macroscopic test masses. Moreover, the atomic clouds can overlap spatially and therefore be subject to the same gravitational acceleration, while simultaneously being imaged in situ. Last but not least, the quantum nature allows test of the WEP without classical analogue by preparing the samples e.g. in superposition states [18].

An overview of state of the art experiments to test the WEP is given in table 1.1. Three categories of experiments can be distinguished. The first category summarizes the already mentioned classical tests based on lunar laser ranging and torsion balances, given here for reference. Experiments of the second category, called hybrid, compare the acceleration obtained by an atom interferometer to the one measured with a (commercial) absolute gravimeter in which the free-fall trajectory of a corner cube is observed with an optical light interferometer. Experiments of the third category directly compare the gravitational acceleration of atomic clouds, either of different species or of the same species, but different isotopes or hyperfine states. While the comparison of different species allows higher sensitivity to WEP violations with respect to some theoretical models [19], comparing the acceleration of the same species suppresses systematic uncertainties related to the species. An exception is the experiment described in reference [20] which does not compare the gravitational acceleration based on propagating matter waves, but on the difference in Bloch frequency of the matter waves confined in an optical lattice.

**Table 1.1:** Overview of state of the art WEP test experiments [21–23].

Category	Experiment	Species	$T$ in ms	Eötvös ratio
Classical	Torsion balance [24]	Be/Ti		$(0.3 \pm 1.8) \times 10^{-13}$
	Lunar laser ranging [25]			$(0.8 \pm 1.3) \times 10^{-13}$
Hybrid	Peters et al. [26]	Cs/Corner cube	160	$(7 \pm 7) \times 10^{-9}$
	Merlet et al. [27]	$^{87}\text{Rb}$ /Corner cube	100	$(4.4 \pm 6.5) \times 10^{-9}$
Quantum	Zhou et al. [28]	$^{85}\text{Rb}/^{87}\text{Rb}$	71	$(2.8 \pm 3.0) \times 10^{-8}$
	Fray et al. [29]	$^{85}\text{Rb}/^{87}\text{Rb}$	40	$(1.2 \pm 1.7) \times 10^{-7}$
	Bonnin et al. [30]	$^{85}\text{Rb}/^{87}\text{Rb}$	40	$(1.2 \pm 3.2) \times 10^{-7}$
	Schlippert et al. [19]	$^{39}\text{K}/^{87}\text{Rb}$	20	$(0.3 \pm 5.4) \times 10^{-7}$
	Tarallo et al. [20]	$^{87}\text{Sr}/^{88}\text{Sr}$	<sup>a</sup>	$(0.2 \pm 1.6) \times 10^{-7}$
	Rosi et al. [18]	$^{87}\text{Rb}/^{87}\text{Rb}$	80	$(1.0 \pm 1.4) \times 10^{-9}$
	Asenbaum et al. [31]	$^{85}\text{Rb}/^{87}\text{Rb}$	955	$(1.6 \pm 1.8(\text{stat}) \pm 3.4(\text{syst})) \times 10^{-12}$

<sup>a</sup> The effect of gravity was examined on atoms confined in an optical lattice, where no propagation time can be stated.

While classical experiments still set the benchmark for highest precision with respect to the Eötvös ratio, there are pathways to achieve unprecedented precision with experiments based on atom interferometry. One way to increase the precision of atom interferometry experiments is presented below.

## 1.2 Matter wave interferometry in microgravity

As can be seen from equation (1.3), the accumulated phase difference in the interferometer scales with  $T^2$  and the sensitivity of atom interferometers therefore greatly benefits from long interrogation times. While the free-fall time in ground-based experiments is ultimately limited by the height of the apparatus, extended interrogation times can be achieved in a microgravity environment. A comparison of the available time in reduced gravity as well as the microgravity level on different research platforms is summarized in table 1.2. The longest time in reduced gravity and the lowest microgravity levels can be found on the International Space Station (ISS) and satellites.

**Table 1.2:** Comparison of microgravity research platforms [32].

Microgravity platform	Reduced gravity time	Microgravity level
Drop tower	2 s–9 s	$10^{-2}$ g– $10^{-5}$ g
Parabolic flights (aircraft)	25 s	$10^{-2}$ g– $10^{-3}$ g
Sounding rocket	6 min	$10^{-3}$ g– $10^{-4}$ g
Space station/(recoverable) satellite in low Earth orbit	> months	$10^{-5}$ g– $10^{-6}$ g

Long interrogation times, however, also bring new challenges and one of the largest uncertainty factors with respect to atom interferometers are wavefront aberrations [33]. Interrogating the atomic cloud with interferometer pulses with non-planar wavefronts results in inhomogeneous phase shifts over the extent of the cloud. Although methods to correct wavefront aberrations have been reported [34], an important mitigation strategy remains the use of ultra-cold atoms. By cooling the atoms, the expansion rate of the cloud is minimized and the atoms are thus subject to the same part of the wavefront. It is therefore favorable to condense the atoms to a Bose-Einstein condensate (BEC)<sup>1</sup>, especially for atom interferometry with long interrogation times.

An overview of experiments to test the WEP on different microgravity platforms is given in table 1.3. The interférométrie atomique à sources cohérentes pour l'espace (ICE) experiment has demonstrated simultaneous atom interferometry with cold potassium and rubidium atoms on board an aircraft during parabolic flights. To perform interferometry, however, the atoms are not condensed but laser-cooled to a magneto-optical trap (MOT).

QUANTUS-1/-2 are the two drop tower experiments within the Quantengase unter Schwerelosigkeit (QUANTUS) collaboration (see next section). While atom interferometry with BECs of  $^{87}\text{Rb}$  atoms in microgravity has already been demonstrated with the first apparatus QUANTUS-1 [37], WEP tests will only be possible with the second generation experiment. QUANTUS-2 was also previously only operated with rubidium BECs [38], but is currently being prepared for the integration of the potassium laser system [39].

<sup>1</sup> A Bose-Einstein condensate is a state of matter formed when a large portion of bosons in an ensemble occupy the ground state and thus become indistinguishable. Bose-Einstein condensates were first demonstrated experimentally in 1995 by Eric Cornell and Carl Wieman [35] as well as Wolfgang Ketterle [36].

NASA's Cold Atom Laboratory (CAL) was launched on the ISS in May 2018 and a Bose-Einstein condensate was created a few months after installation. Similar to its successor Bose-Einstein Condensate and Cold Atom Laboratory (BECCAL) from Deutsches Zentrum für Luft- und Raumfahrt e. V. (DLR) and NASA, it enables a variety of experiments with ultra-cold or condensed clouds of potassium and rubidium atoms, including WEP tests [40].

The micro-satellite à traînée compensée pour l'observation du principe d'équivalence (MICROSCOPE) satellite tests the WEP classically. However, it greatly benefits from the quiet environment as well as the long measurement times in space and is given here as benchmark for space-based experiments. Launched in April 2016 into a circular orbit at 710 km altitude, the satellite carries two differential accelerometers. While both accelerometers compare the free-fall accelerations of two test masses, one serves as reference with test masses of the same composition [41].

**Table 1.3:** Overview of WEP test experiments on different microgravity platforms.

Experiment	Platform	Species	$T$ in ms	Eötvös ratio [projected]
ICE [42, 43]	Aircraft	$^{39}\text{K}/^{87}\text{Rb}$	2	$(0.9 \pm 3.0) \times 10^{-4}$ [ $10^{-11}$ ]
QUANTUS-1/-2 [37]	Drop tower	$^{41}\text{K}/^{87}\text{Rb}$	1000	$[6 \times 10^{-11}]$
CAL [44, 45]	ISS	$^{39}\text{K}/^{87}\text{Rb}$ and $^{41}\text{K}/^{87}\text{Rb}$		
BECCAL [40]	ISS	$^{41}\text{K}/^{87}\text{Rb}$		
MICROSCOPE [41]	Satellite	Ti/Pt (classical)		$(1 \pm 9(\text{stat}) \pm 9(\text{syst})) \times 10^{-15}$

In summary, it can be said that atom interferometry in microgravity permits long interrogation times and, eventually, unprecedented precision [46]. However, this entails enormous technological challenges to reduce the experiments' size, weight and power (SWaP) budget and allow for autonomous operation. Important contributions along this path were made by the QUANTUS collaboration, briefly presented hereafter.

### 1.3 Joint research effort QUANTUS

The Quantengase unter Schwerelosigkeit (QUANTUS) consortium is an association of several German universities and research institutes,<sup>1</sup> supported by the German Space Agency DLR with funds provided by the Federal Ministry for Economic Affairs and Energy (BMWi). Established in 2004, its main purpose is the investigation of BECs as the source for matter wave interferometry in microgravity.

The first two generations of experiments use the drop tower Bremen as microgravity platform. That is, dedicated capsules experience 4.74 s free-fall time corresponding to a height of 110 m in an evacuated drop tube. The time in free fall can be extended to more than 9 s by using a pneumatic catapult system to shoot the capsule upwards [47].

The first generation apparatus QUANTUS-1 demonstrated a BEC in microgravity for the first time [48]. A Bose-Einstein condensate of about  $10^4$   $^{87}\text{Rb}$  atoms could be generated by means of an atom chip [49]. In addition, the system was used for the first demonstration of atom interferometry with BECs in microgravity [37]. Delta-kick collimation (DKC) [50–52] was employed to reduce the kinetic energy and thus the expansion rate of the atomic cloud, a prerequisite to achieve long interrogation times. Not least, the first gravimeter based on an atom chip could be realized with this apparatus [53]. While so far only operated with rubidium [38], the second generation experiment QUANTUS-2 will soon employ potassium to enable WEP tests with BECs of  $^{41}\text{K}$  and  $^{87}\text{Rb}$  in microgravity.

On the ladder of increasing times in microgravity (see table 1.2), the next step was skipped and the sounding rocket mission program Materiewelleninterferometer unter Schwerelosigkeit (MAIUS) was introduced. On board a sounding rocket, the experimental payload performs a ballistic flight with an apogee at an altitude of about 260 km corresponding to a time in reduced gravity of approximately 6 min<sup>2</sup>. New technological challenges had to be overcome and only one species was initially employed to benefit from the expertise of the previous generations.

On 23 January 2017, the first BEC in space was created as part of the mission MAIUS-1. A Bose-Einstein condensate of about  $10^5$   $^{87}\text{Rb}$  atoms was produced in 1.6 s and 110 experiments central to atom interferometry were performed [54]. The payload for the follow-up missions MAIUS-2/-3, scheduled for 2021 and 2022, is currently being integrated. Sharing the same payload [55, 56], the experiments will perform atom interferometry with BECs of  $^{41}\text{K}$  and  $^{87}\text{Rb}$  sequentially (MAIUS-2) and simultaneously (MAIUS-3).

---

<sup>1</sup> Project partners in the QUANTUS consortium currently are DLR, Ferdinand-Braun-Institut, Leibniz-Institut für Höchstfrequenztechnik (FBH), Humboldt-Universität zu Berlin (HUB), Johannes Gutenberg University Mainz (JGU), Leibniz University Hannover (LUH), Technical University of Darmstadt (TUDA), Universität Hamburg (UHH), Ulm University (UULM) and the Zentrum für angewandte Raumfahrttechnologie und Mikrogravitation (ZARM).

<sup>2</sup> The Kármán line at an altitude of 100 km serves as definition for the boundary to space, where the experimental phase and thus the time counted in microgravity begins and ends.

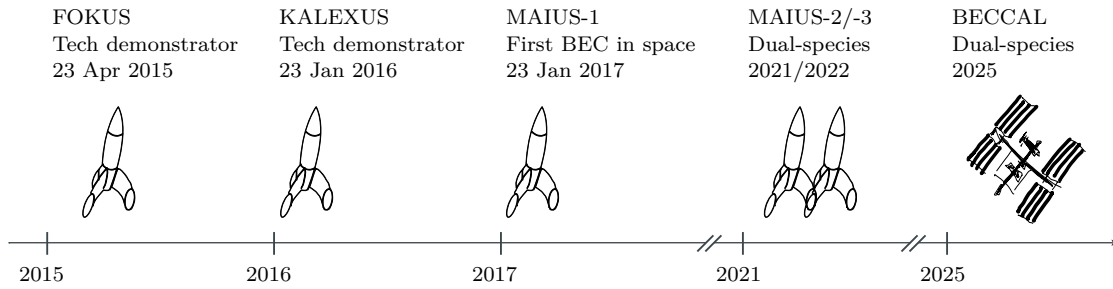


**Figure 1.2:** Space missions of the QUANTUS consortium with (scheduled) launch dates.

Complementary to the MAIUS missions, technology demonstrator missions were carried out as part of the Technologische Experimente unter Schwerelosigkeit (TEXUS) program of the DLR, namely Faserlaser basierter optischer Kammgenerator unter Schwerelosigkeit (FOKUS) [57] and Kalium Laserexperimente unter Schwerelosigkeit (KALEXUS) [58]. An overview of the QUANTUS consortium’s space missions with (scheduled) launch dates is given in figure 1.2.

Following the ladder of increasing microgravity times, DLR and NASA have joined forces to develop a quantum gas experiment for the International Space Station (ISS). Developed by the QUANTUS consortium, the Bose-Einstein Condensate and Cold Atom Laboratory (BECCAL) is designed as multi-user and multi-purpose apparatus for experiments based on BECs of  $^{41}\text{K}$  and  $^{87}\text{Rb}$  and quantum degenerate gases of  $^{40}\text{K}$  [40]. The launch to the ISS is scheduled for 2025.

#### 1.4 Outline of this thesis

Since its advent some 25 years ago, atom interferometry has matured into a versatile tool that is about to leave the laboratory for use in areas such as metrology, geophysics, space, civil engineering, and navigation [17]. The operation outside protected environments is accompanied by an increasing demand for robust and compact laser systems. And although each system is tailored to the specific requirements of the corresponding platform and application, there are technologies applicable to a wide range of systems. This is where this thesis makes a contribution. Originated in the context of laser system development for the missions MAIUS-2/-3, some technologies have already been implemented while others are candidates for future applications in space or other adverse environments. The most important results, which have been published and are part of this thesis (see publication I, publication II and publication III), are complemented by further manuscripts at different stages of publication (see scientific publications).

After the general motivation and the introduction of the QUANTUS consortium, chapter 2 gives an overview of the sounding rocket missions MAIUS-2 and MAIUS-3. The conceptual requirements are derived from the scientific objectives, before the hardware implementation in form of the scientific payload as well as the launch vehicle and flight parameters are discussed. The laser system for MAIUS-2/-3 is presented in chapter 3. A general overview of the functionality and architecture is followed by a more detailed discussion of

---

the underlying technologies. Early-stage developments and proof of concepts for future applications independent of MAIUS are presented in chapter 4. These technologies facilitate the adoption of quantum optical systems for environments where system size and robustness are key. Chapter 5 outlines proposals and systems building on the results presented in publication I, publication II and publication III. The thesis concludes in chapter 6 with a summary and a current status overview of the MAIUS missions, including the next steps as an outlook.

Some sections are summaries or based at least in part on the publications. This is indicated in italics at the beginning of respective sections.





## CHAPTER 2

---

### Sounding rocket missions MAIUS-2 and MAIUS-3

---

The sounding rocket mission program MAIUS is the logical continuation of the work in the QUANTUS consortium to investigate BECs as the source for matter wave interferometry with parameters not accessible on ground. Following the successful MAIUS-1 mission, which created the first BEC in space, the two sounding rocket missions MAIUS-2 and MAIUS-3 are currently planned to extend the parameter range to potassium and mixtures of potassium and rubidium. MAIUS-2 and MAIUS-3 share the same scientific payload, but perform different experiments.

The mission MAIUS-2 has the following scientific objectives:

1. demonstration of atom interferometry with a potassium BEC,
2. performing measurements on delta-kick collimation of rubidium, and
3. sequential interferometry with potassium and rubidium.

Building on the results of MAIUS-2, the scientific objectives of the mission MAIUS-3 are:

1. simultaneous generation and manipulation of quantum degenerate gases in space, and
2. simultaneous dual-species interferometry.

The conceptual requirements for the experiment result from the laser cooling scheme to achieve these objectives, and are presented next. The conceptual requirements are translated into functional requirements as starting point for the development of a hardware implementation, taking into account the SWaP budget of the launch vehicle and the environmental conditions during flight. Both the launch vehicle and the flight parameters are presented after the laser cooling scheme, before introducing the experiment hardware in the form of the scientific payload. Finally, the procedure to qualify the experiment for use on a sounding rocket is discussed.

#### 2.1 Conceptual experiment requirements

The scheme for cooling and manipulating the atoms as defined in the scientific objectives lays the foundation for the hardware development. While this is purely conceptual in the first instance, an apparatus based on an atom chip was assumed to benefit from the heritage of previous experiments in the consortium. The apparatus is required to perform a series of experiments during flight, of which a typical sequence is briefly described below (for further details, see e.g. references [23, 38, 55, 56]).

An experiment sequence starts with cooling and trapping atoms of  $^{41}\text{K}$  and/or  $^{87}\text{Rb}$  in a 3D MOT. No single cooling transition for potassium can be addressed here since the hyperfine splitting of the upper state ( $^2\text{P}_{3/2}$ ) is comparable to the natural linewidth of the  $\text{D}_2$  line ( $\approx 6$  MHz). Therefore, two laser frequencies (cool and re-pump) with similar and relatively high intensities detuned to the whole manifold of transitions from the ground states  $F = 1$  and  $F = 2$  to the upper state are necessary [59].

From the 3D MOT, the atoms are shifted towards the atom chip and further cooled below the Doppler limit by means of optical molasses schemes [60, 61]. In order to be able to load the atoms into the atom chip magnetic trap, they have to be prepared in a magnetically sensitive state in which they are attracted to the field minimum (low-field seeking). This is realized by optical pumping the atoms with light which is also used for detection. Once loaded into the magnetic trap, evaporation cooling with a microwave is employed to condense the rubidium atoms which in turn sympathetically cools the potassium atoms as reported for the CAL atom chip setup [44]. After generation of a Bose-Einstein condensate, the atoms are released for atom interferometry as discussed in section 1.1. Additionally, a single-beam optical dipole trap (ODT) at 1064 nm allows one to study mixtures of dual-species BECs.

To implement these concepts in a scientific payload, both the SWaP budget of the launch vehicle and the environmental conditions during flight must be taken into account and are presented next.

## 2.2 Suborbital flight

All MAIUS missions fly on a VSB-30 sounding rocket, launched from the Swedish Space Corporation (SSC)-operated Esrange Space Center in northern Sweden. Unlike most rocket ranges, this site near the mining town of Kiruna in the midst of the Swedish tundra enables the retrieval of payloads for scientific evaluation. After a brief overview of the VSB-30 and its SWaP budget, the main events and environmental conditions during flight are described.

### 2.2.1 Launch vehicle

The VSB-30 is a two-stage, unguided and rail launched rocket. The entire rocket consists basically of three parts, the first and second stage as well as the payload, whereby the payload includes the recovery system and service module in addition to the actual experiment.

The first and second stage each contain a motor with propellant (solid HTPB/AP/Al) and have an outer diameter of 557 mm and a length of 3214 mm and 3294 mm, respectively [62]. The payload has a diameter of 500 mm which is slightly larger than usual payloads on VSB-30 rockets due to constraints of the experiment [63]. The length of the scientific payload of 2806.08 mm leads to an overall vehicle length of 11.97 m and the mass of the scientific payload is approximately 330 kg.

The service module on top of the scientific payload handles the bidirectional communication with the ground station and monitors housekeeping and flight performance data. The service module also houses the attitude and rate control system (ARCS) which controls the payload orientation and rate above an altitude of 100 km by means of cold gas thrusters [63].

Spin stabilization is achieved by canted fins and three spin up motors. The roll rate at burnout of the second stage is approximately 3 Hz (see section 2.2.3) [64, 65]. A so-called Yo-Yo is used to de-spin the vehicle before the experimental phase. The Yo-Yo consists of two masses connected by a steel cable which is wrapped around the payload adapter before launch. At release, the masses are accelerated centrifugally, therefore compensating for the rocket's torque.

### 2.2.2 Flight events

The main flight events are visualized in figure 2.1 and summarized in tabular form in appendix A. The specified time and altitude values were calculated for MAIUS-1 and will slightly vary for MAIUS-2/-3 as the payload has a different length and mass.

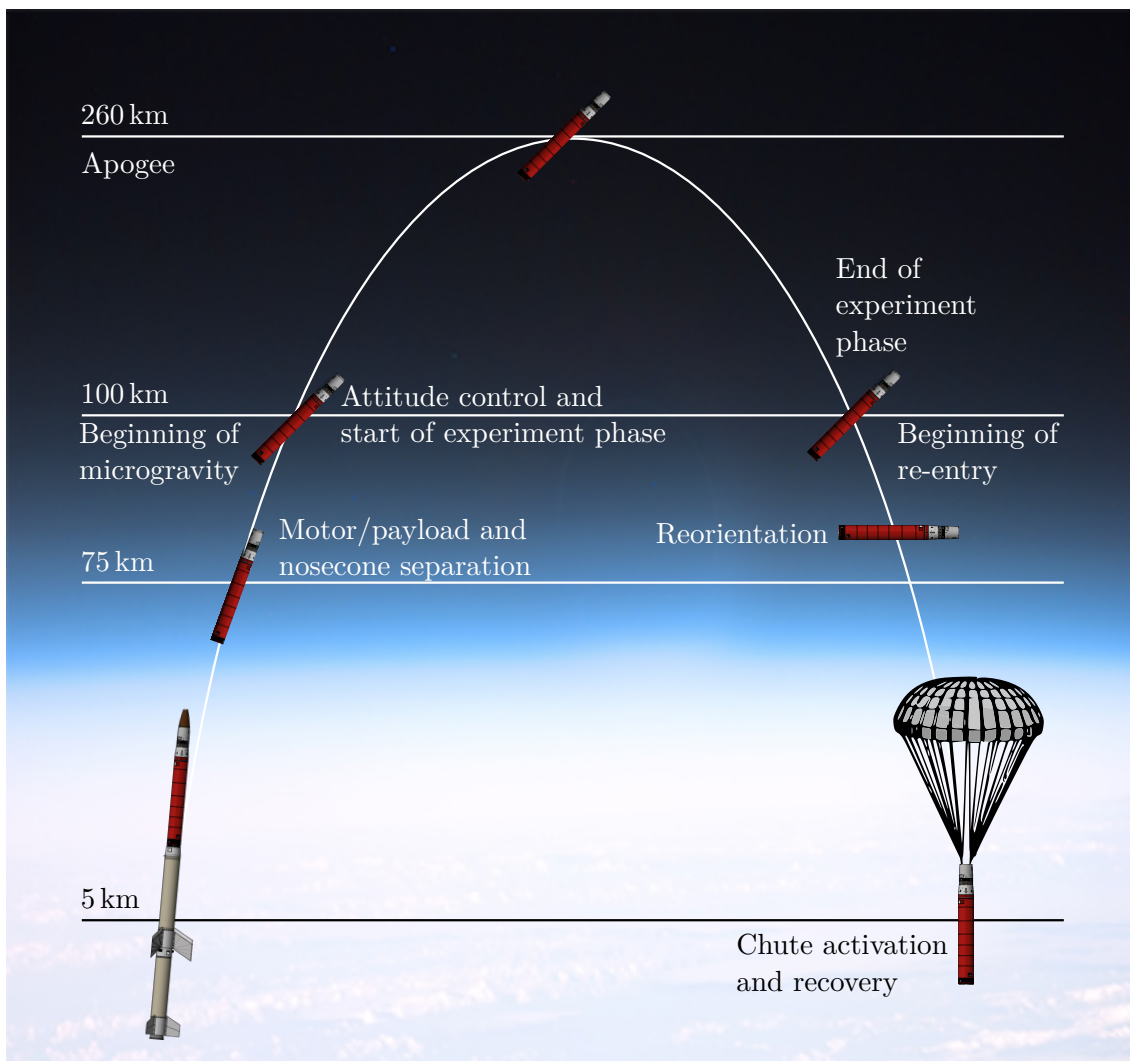


**Figure 2.1:** Illustration of main flight events, altitude values calculated for MAIUS-1. Adapted from reference [66].

The flight sequence starts with the ignition of the first stage and lift-off at  $t = 0.0$  s. After 13.5 s, the first stage is burned out and separates by drag from the second stage. The second stage ignites 1.5 s after burnout of the first stage and burns for 29.0 s. The ballistic flight begins at an altitude of 43.40 km after burnout of the second stage. The vehicle is de-spun by ejecting the Yo-Yo before the nosecone is separated from the payload 58.0 s after lift-off and separation of the motor 60.0 s after lift-off. One second later, the attitude and rate control system starts to control the attitude of the vehicle and aligns the interferometer axis to the gravity vector of Earth.

The microgravity phase begins 75.0 s after lift-off at an altitude of 101.02 km. The attitude is regulated two more times, once before and once after reaching the apogee at an altitude of around 260 km.

The experiment phase ends at an altitude of 100.00 km and the atmospheric re-entry begins. The payload is oriented horizontally and spun up to equally distribute the thermal load. At an altitude of 4.70 km, the recovery system heat shield is ejected and the payload is recovered with a two-stage parachute system.

### 2.2.3 Environmental conditions during flight

The environmental conditions during flight play a crucial role when designing a rocket payload in terms of stability requirements to be met. Mechanical and thermal conditions are particularly important for the construction of the laser system and are discussed below.

#### Mechanical loads

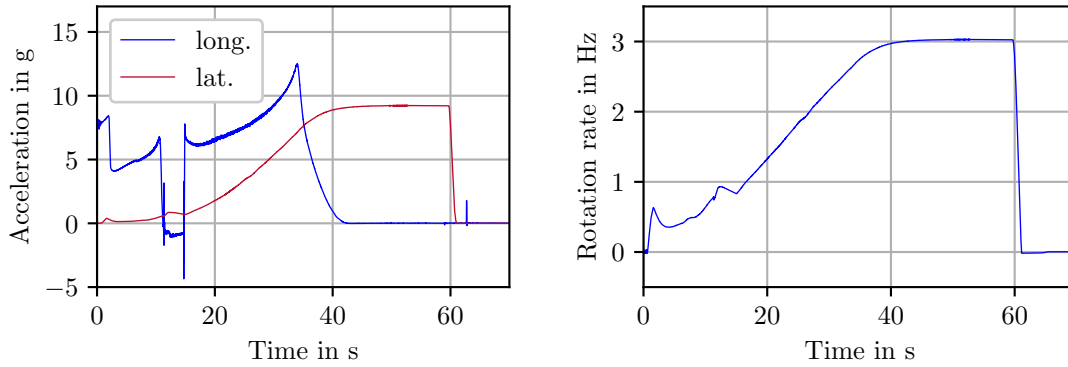
Mechanical loads acting on the payload mainly stem from motor burning during the launch phase and atmospheric drag during re-entry. The longitudinal and lateral accelerations during the launch phase of MAIUS-1 are shown in figure 2.2(a). While the longitudinal accelerations are measured values, the lateral accelerations are calculated from the rotation rate, shown in figure 2.2(b), according to  $a_{\text{lat.}} = \omega^2 r$  with  $r = 0.25$  m corresponding to the outer radius of the payload hull. Again, the loads on MAIUS-2/-3 are expected to be slightly different.

The drop in longitudinal acceleration after 10 s is caused by the separation of the first and second stage, the maximum acceleration of 12.5 g is reached after 34 s. The maximum lateral acceleration is 9.3 g.

In addition to static loads, the motor burn also causes vibrations of the payload. The vibrations measured on the first flight of the VSB-30 do not exceed  $2 g_{\text{RMS}}$  [67].

The accelerations measured along all spacial axes during the re-entry of MAIUS-1 are shown in figure 2.3. The maximum of 14.8 g was reached 472 s after lift-off, a bit earlier than the predicted 487 s (see table A.1 in appendix A), along the pitch axis. The maximum accelerations during re-entry occur in lateral direction because the payload is oriented with the roll axis horizontally (see section 2.2.2).

The mechanical loads during launch and re-entry are summarized in table 2.1.



(a) Longitudinal and lateral accelerations as a function of flight time.

(b) Rotation rate around the roll axis as a function of flight time.

**Figure 2.2:** Measured payload accelerations and rotation rate during the launch phase of MAIUS-1 with lift-off at  $t = 0.0$  s [68].

**Table 2.1:** Mechanical loads during launch and re-entry, measured during the first flight of the VSB-30 (vibrations) and the mission MAIUS-1 (remaining values).

Event	Duration	Level
Motor acceleration longitudinal	<44s	12.5 g max.
Spin acceleration (lateral)	<62s	9.3 g max.
Motor vibrations [67]	<44s	< 2 grms
Re-entry acceleration (lateral)	<50s	14.8 g max.

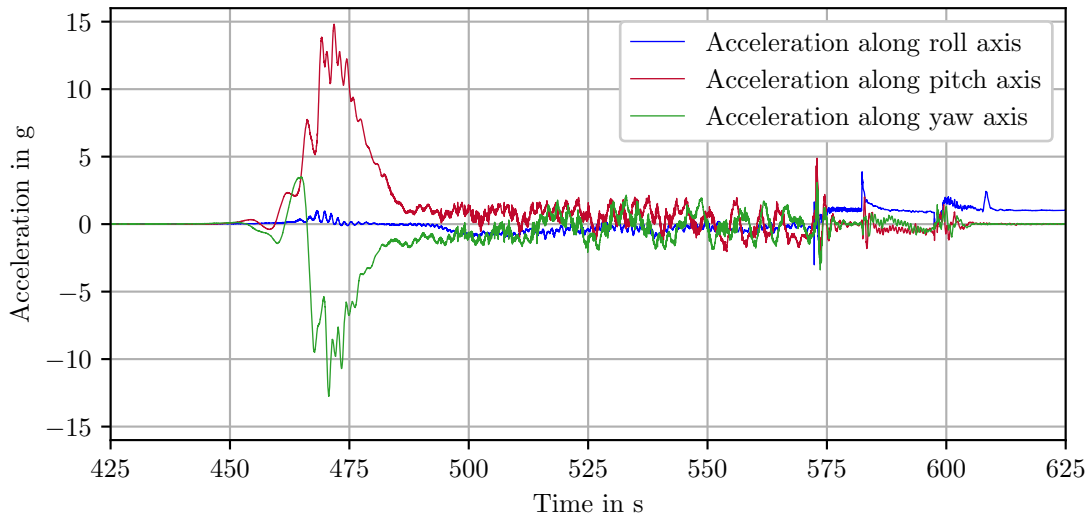


**Figure 2.3:** Measured payload accelerations as a function of flight time during the re-entry of MAIUS-1 with lift-off at  $t = 0.0$  s [68].

### Thermal loads

While the payload is actively cooled by the ground support equipment (GSE) when operated on ground, no active cooling is possible during flight. In contrast to the mechanical loads, the payload structure (see next section for a detailed description) must be taken into account when determining the thermal loads, since only little heat is generated by atmospheric heating of the hull. Most of the thermal load is generated by the control electronics and the laser modules within the payload itself [69]. An overview of the internally generated thermal loads is given in table 2.2.

**Table 2.2:** Thermal loads generated within the payload for MAIUS-2/-3 [69].

Subsystem	Thermal load in W
Electronics	174
Physics package	50
Laser system	100
Laser electronics	380
Batteries	23
Sum	727

All subsystems have a heat sink to absorb thermal loads during the flight. The laser system heat sink is designed to keep the temperature rise during flight within 5 K with an initial heat sink temperature of 20 °C [69]. The design of the heat sink and thus the temperature rise during flight is the result of an optimization process, based on a feedback loop of hardware development, software simulation and experimental validation.

Taking into account the SWaP budget of the VSB-30 and the outlined environmental conditions during flight, the scientific payload was developed to meet the conceptual requirements derived from the scientific objectives, and is presented hereafter.

### 2.3 Scientific payload

The scientific payload for the missions MAIUS-2/-3 consists of five subsystems, interconnected with electrical cables and optical fibers: electronics, physics package, laser system, laser electronics and batteries (from top to bottom, see computer-aided design (CAD) rendering in figure 2.4). The subsystems are built on intermediate platforms which are connected to the hull by mounting brackets with vibration dampers. The hull is divided into 7 segments with an outer diameter of 500 mm and a wall thickness of 4 mm. The hull is sealed at both ends with sealing plates so that the payload can be pressurized to atmospheric level with artificial air (20 % oxygen, 80 % nitrogen) before launch. This allows the ambient pressure of a laboratory environment on ground to be maintained during flight. For transportation, the scientific payload with an overall length of 2806.08 mm can be separated between the laser system and the laser electronics.

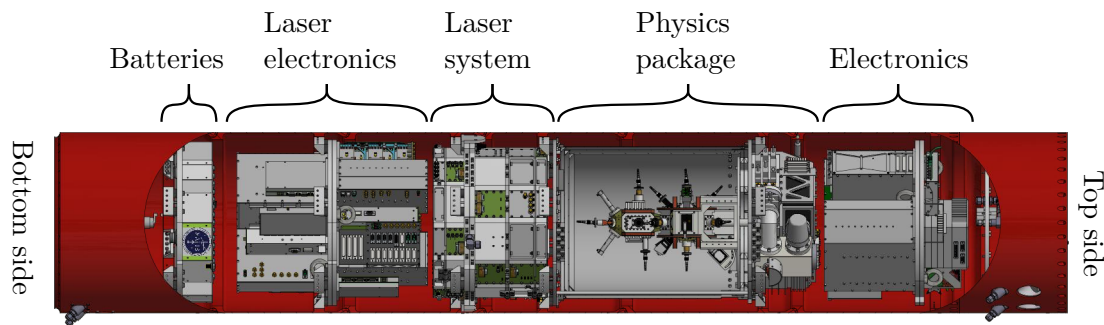


**Figure 2.4:** CAD rendering of the scientific payload for MAIUS-2/-3 with 500 mm diameter and 2806.08 mm length. Adapted from reference [69].

The electronic systems and the physics package are developed by project partners and are therefore only briefly presented below, further details can be found in references [55, 56]. However, a summary of relevant features in particular of the physics package is necessary to understand the required system functions of the laser system, which is discussed in greater detail in chapter 3.

### 2.3.1 Electronic systems

The electronic systems are the backbone of the experiment and the interface to the rest of the payload. The systems are divided into electronics, laser electronics and batteries so that the payload's center of mass is as close as possible to the atoms [55]. This is to prevent unwanted accelerations of the atoms due to residual rotations of the vehicle in microgravity.

The electronics subsystem comprises the on-board computer, the low-noise current drivers for the coils and the atom chip as well as their batteries.

The dedicated laser electronics subsystem contains all the electronics required to control the laser system. This includes the current drivers and temperature controllers for operating the laser modules as well as the drivers for acousto-optic modulators (AOMs) and electro-optic modulators (EOMs). The analog monitoring data such as temperature and optical power values are also digitized here.

Eight lithium iron phosphate ( $\text{LiFePO}_4$ ) batteries with a capacity of 15 Ah each supply power for operating the experiment during flight. The battery subsystem also includes tools for battery protection and monitoring of all currents, voltages and temperatures.

### 2.3.2 Physics package

The physics package contains the vacuum chamber, the pumping system including control electronics as well as a microwave and radio frequency (RF) source for evaporative cooling and state manipulation of the atomic ensembles. The pumping system comprises two titanium sublimation pumps and one ion getter pump. A CAD rendering of the physics package is depicted in figure 2.5.

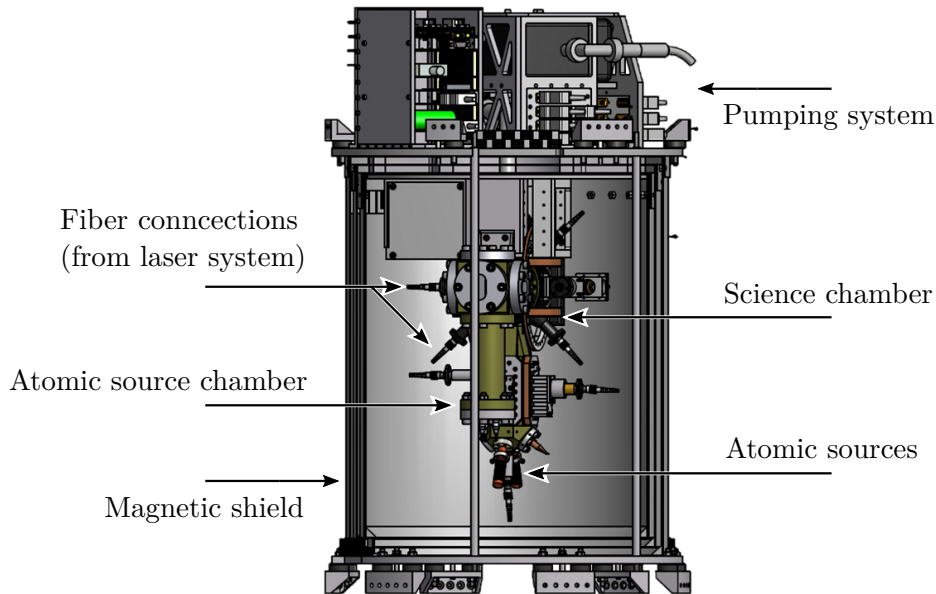


**Figure 2.5:** CAD rendering of the physics package for MAIUS-2/-3 with 458 mm diameter and 735 mm height (without mounting brackets). Adapted from reference [69].

The design of the vacuum chamber is based on the chamber for MAIUS-1 [70] and comprises two parts, the science chamber and the atomic source chamber, separated by a differential pumping stage (DPS). The atomic sources with 1 g of the respective species in natural isotope abundancies are attached to the source chamber. Heating wires around the atomic sources allow control of the temperature and thereby the partial pressure in the chamber. A 2D MOT [71] atom beam generated in the source chamber is transferred through the DPS to the 3D MOT in the science chamber by means of pusher/retarder beams (a so-called  $2D^+$  MOT). This is an additional pair of laser beams with comparatively low and independently adjusted beam intensities, whose unbalanced radiation pressure permits the atom transfer [72]. The science chamber contains the atom chip composed of three layers of microstructures. The chip allows fast transport of the atomic clouds to feed the atom interferometer [73]. The surface of the chip has a high-reflective coating and thus acts as a mirror, reducing the number of beams necessary for the 3D MOT to four. This type of MOT is known as mirror-MOT [74].

Spatially resolved detection of the atomic clouds is realized by charge-coupled device (CCD) cameras, whereby simultaneous absorption and fluorescence imaging is possible. A fluorescence photodiode allows fast imaging during the MOT phase.

The interferometer axis, along which the acceleration is measured, consists of a collimator on one end and a mirror on the other end. The mirror is attached to an accelerometer which constantly measures vibrations and thereby allows post correction of the acquired phase signal. Placing a quarter-wave plate (QWP) in front of the mirror enables one to switch between different interferometer schemes including Bragg double diffraction [75, 76] and Raman double diffraction [77].



Previous flight campaigns have shown that the strength of Earth’s magnetic field during flight can vary by up to  $50 \mu\text{T}$  [78]. The vacuum chamber is therefore surrounded by a three-layer magnetic shield made of mu-metal to insulate the magnetically sensitive atoms. Originally designed for MAIUS-1, the magnetic shield provides a shielding factor of at least 1000 in all spatial directions [78].

Alongside the payload development, vibration tests are necessary to qualify (commercial) components and systems for use on a sounding rocket. The corresponding procedures are briefly presented below.

#### 2.4 Qualification procedure

As outlined in section 2.2.3, the payload is exposed to motor vibrations of  $< 2 g_{\text{RMS}}$  and accelerations of maximum 12.5 g in longitudinal direction due to the thrust, and maximum 9.3 g in lateral direction due to the spin of the vehicle during launch phase. To ensure reliable operation under these conditions, the system and its components must undergo vibration tests in all spatial directions at component, subsystem and payload level [66]. That is, random vibrations for 60 s per axis with a power spectral density (PSD) at qualification (for components) and acceptance level (for subsystems and the entire payload) and in the frequency range given in table 2.3. To this end, the test item is mounted on a shaker table and both the test item and the table are equipped with accelerometers for response monitoring and acceleration control, respectively.

**Table 2.3:** Power spectral densities and respective frequency ranges of the different vibration test levels [66].

Frequency	PSD qualification level	PSD acceptance level	PSD flight level
20 Hz to 399 Hz	$0.0045 \text{ g}^2/\text{Hz}$	$0.002 \text{ g}^2/\text{Hz}$	$0.0003 \text{ g}^2/\text{Hz}$
400 Hz to 599 Hz	$0.0675 \text{ g}^2/\text{Hz}$	$0.03 \text{ g}^2/\text{Hz}$	$0.004 \text{ g}^2/\text{Hz}$
600 Hz to 1299 Hz	$0.0045 \text{ g}^2/\text{Hz}$	$0.002 \text{ g}^2/\text{Hz}$	$0.0003 \text{ g}^2/\text{Hz}$
1300 Hz to 2000 Hz	$0.0675 \text{ g}^2/\text{Hz}$	$0.03 \text{ g}^2/\text{Hz}$	$0.004 \text{ g}^2/\text{Hz}$
RMS value	8.1 g	5.4 g	2.0 g
Duration	60 s	60 s	60 s

Before and after each random vibration test run, sinusoidal frequency sweeps at 0.25 g level are performed with a sweep rate of 2 oct/min to measure the resonance spectrum of the test item. Deviations in the frequency response before and after a random vibration test would indicate a failure of the equipment under test.



# CHAPTER 3

---

## Laser system for MAIUS-2/-3

---

In the previous chapter, the sounding rocket mission program MAIUS and its scientific objectives were introduced. In addition to the launch vehicle and the flight parameters, the structure and qualification procedure of the payload and especially the scientific payload was addressed.

On this basis, the laser system as one of five subsystems of the scientific payload is presented in this chapter. The main task of the laser system is to provide light for laser cooling, atom interferometry and detection as well as the optical dipole trap (ODT). First, a general overview of the functionality and hardware implementation is given before the underlying technologies and developments are discussed in more detail.

### 3.1 System functions and schematic structure

The laser system is designed to meet the conceptual requirements outlined in section 2.1. To this end, the system must provide light to the physics package, described in section 2.3.2, in order to fulfill the following functions at the number of fiber ports mentioned:

- initial cooling of potassium and rubidium atoms in the 2D MOT with light provided at two fiber ports for a retro-reflex configuration,
- transfer of the atoms through the DPS with pusher and retarder beams from one port, respectively,
- laser cooling in the 3D MOT using four beams (mirror-MOT) from four separate fiber ports,
- optical state preparation for the magnetic trap using the single-port detection beam,
- generation of interferometry pulses with light from one fiber port,
- simultaneous absorption and fluorescence detection, and
- provision of the single-beam ODT.

Since the optical power levels required to achieve these functionalities cannot be clearly defined, they were specified at component level and will only be discussed using one example (see section 3.4.1). A detailed review of the cooling procedure and its (power) optimization based on the physics package for MAIUS-1 can be found in reference [23]. The light is guided linearly polarized via optical polarization maintaining (PM) fibers to the physics package and the polarization is adjusted in situ.

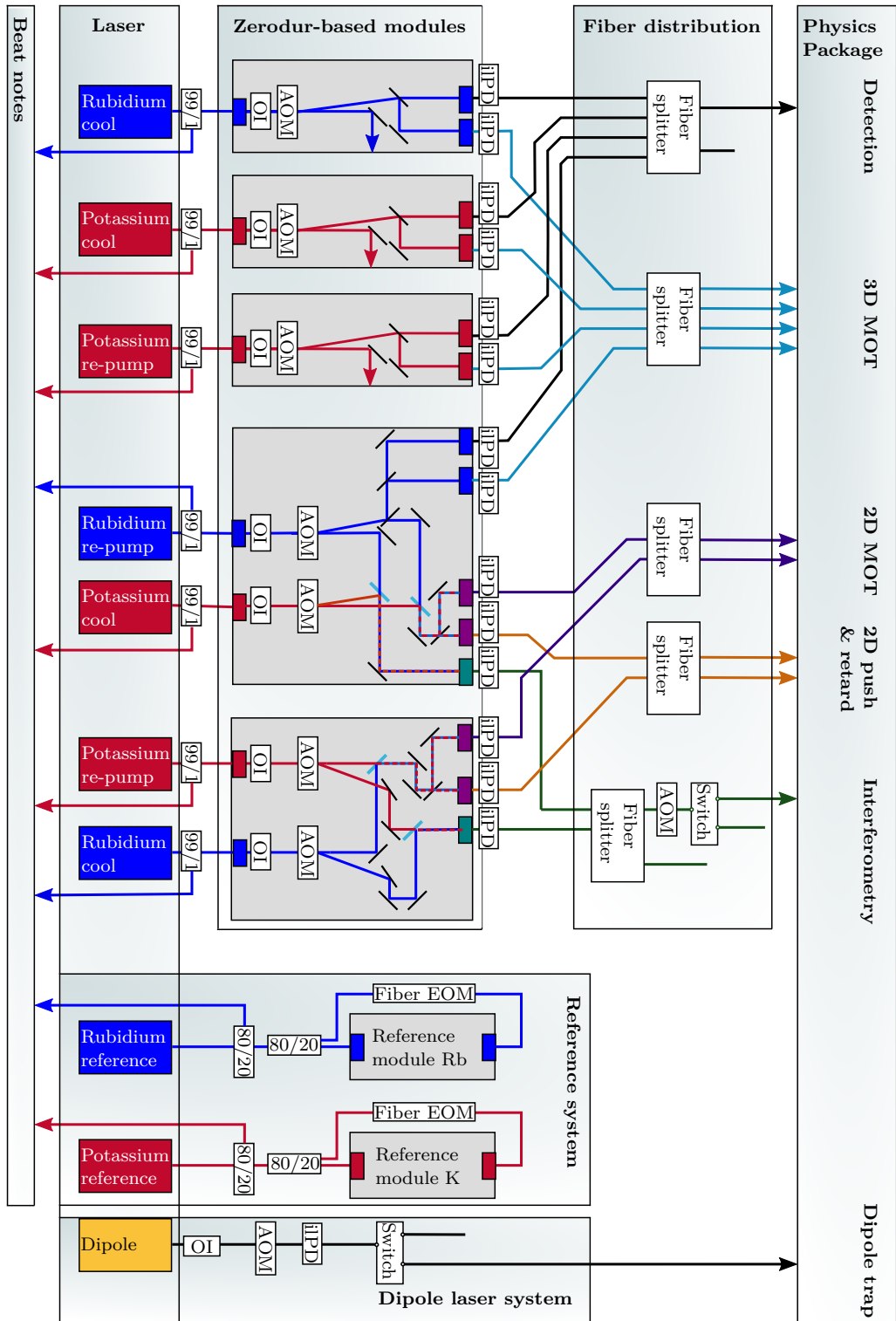


**Figure 3.1:** Schematic structure of the laser system for MAIUS-2/-3. AOM: acousto-optic modulator; EOM: electro-optic modulator; iPPD: inline photodiode; OI: optical isolator; 99/1, 80/20: splitting ratios. Adapted from reference [79].

The schematic structure of the laser system is shown in figure 3.1. All fiber-based components maintain polarization and are spliced together to minimize losses. The fiber links to the physics package and their respective functionalities are indicated in the upper part. A total of ten lasers, shown in the lower part, generate the necessary light. Eight of these lasers are extended cavity diode laser (ECDL) master oscillator power amplifier (MOPA) modules [80, 81], four of which operate at wavelengths around 767 nm to address potassium and three at wavelengths around 780 nm to address rubidium transitions, respectively. The asymmetry results from the higher re-pump intensities required for potassium (see section 2.1) and thus a dedicated re-pump laser for both the 2D and 3D MOT. The light for the ODT is provided by the remaining ECDL MOPA module operating at a wavelength around 1064 nm. Two distributed feedback (DFB) lasers [82] are dedicated frequency reference lasers, one for each species.

Apart from the free-running dipole laser, all other ECDL MOPA modules are frequency stabilized with respect to the two reference lasers via offset beat notes. For this purpose, about 1% of the light directed towards the physics package is split off with fiber splitters. The remaining share is guided to fiber-coupled Zerodur-based optical modules (hereinafter referred to as “scientific modules”, shown in the central part in figure 3.1) for distribution, overlap and switching in free space. Still on the modules, the light is coupled back into optical fibers before passing inline photodiodes (ilPDs). Here a fixed amount of light is directed from the fiber core on a photodiode at the cladding surface for monitoring and troubleshooting purposes [83]. The main part of the light is superimposed with fiber splitters and directed to the corresponding ports of the physics package.

The reference system shown on the right-hand side in figure 3.1 provides the frequency references for all lasers except the dipole laser. To this end, about 20% of the light emitted by the two reference lasers is split off with fiber splitters for the beat notes, while the remaining 80% are stabilized on atomic transitions of potassium and rubidium by means of modulation transfer spectroscopy (MTS) or frequency modulation spectroscopy (FMS) (see section 3.4.2). The light passes a vapor cell of the respective species, implemented on Zerodur-based optical modules, and is detected on a photodiode for electronic generation of a frequency discriminant.

The laser system for the ODT shown on the far right in figure 3.1 is purely fiber-based. Behind an optical isolator (OI), the optical power is detected on a photodiode for stabilization via the AOM diffraction efficiency, i.e. the RF power applied. A switch permits one to block the light with high extinction ratio.

### 3.2 System architecture

The hardware of the laser system schematics is implemented in a dodecagonal aluminum housing with 458 mm diameter and 319 mm height. The housing contains five stacked levels, each accessible via hinges. The main platform connecting the laser system to the hull acts as water-cooled heat sink. A CAD rendering of the system is shown in figure 3.2.

The levels from top to bottom are “distribution level”, “Zerodur level”, “reference level”, “laser level” and “beat level”. The distribution level contains the fiber splitters to superimpose light for detection, 2D<sup>+</sup> MOT, 3D MOT and interferometry. The fiber switches for slow switching with high extinction ratio and fiber AOMs for fast switching of interferometry and dipole trap beams are also located on this level. All single-input and one of the double-input Zerodur-based optical modules as well as the optical isolator of the dipole trap are located on the Zerodur level below. The reference level on top of the heat sink houses the other double-input Zerodur-based optical module, the dipole laser and the reference system including the reference lasers, the frequency reference modules and the fiber EOMs. Seven lasers, four at wavelengths around 767 nm and three around 780 nm, are mounted on the underside of the heat sink in the laser level. The lowest level contains the fiber splitter and photodiode assembly for the beat note detection.



**Figure 3.2:** CAD rendering of the laser system for MAIUS-2/-3 with 458 mm diameter and 319 mm height (without mounting brackets). Adapted from reference [79].

In addition to the functional requirements, the laser system must also meet the stability requirements and fit within the SWaP budget. The environmental conditions the system is exposed and required to withstand to have been presented in section 2.2.3, the qualification procedure in section 2.4. The SWaP budget on the other hand is given by the launch vehicle as presented in section 2.2.1. An already extended inner hull diameter of 492 mm and a maximum mass budget of 330 kg are available for the entire scientific payload.

To meet the stability requirements as well as the payload constraints of sounding rocket experiments, we have developed a technology for miniaturized and robust fiber-coupled optical modules, presented next.

### 3.3 Zerodur technology

*This section is based on publication II.*

Our technology for miniaturized and robust fiber-coupled optical modules is based on Zerodur, a lithium aluminum silicon oxide glass ceramic from Schott. Zerodur consists of evenly distributed nanocrystals within a residual glass phase. By compensating the positive coefficient of thermal expansion (CTE) of the glass matrix with the negative CTE of the nanocrystals, a mean CTE as low as  $(0.00 \pm 0.02) \times 10^{-6} / \text{K}$  (expansion class 0) in the range between  $0^\circ\text{C}$  and  $50^\circ\text{C}$  is achieved [84, 85].<sup>1</sup>

Different low CTE materials were compared in terms of density, machinability and suitability for bonding techniques before choosing Zerodur as the base material for our optical bench technology [8]. Following the decision, we developed a toolkit of optical elements including fixed and adjustable mirrors as well as PM fiber collimators and couplers made from Zerodur that we can mount on a Zerodur baseplate. Building stable optical modules by mounting optical elements on a baseplate requires a jointing technique which permits stable bonds and precise alignment of the components. Common techniques include hydroxide-catalysis and adhesive bonding.

Hydroxide-catalysis bonding, also known as silicate bonding, was invented and patented [87, 88] at Stanford University for the telescope of the Gravity Probe-B mission [89]. Further application examples include the optical benches for the Laser Interferometer Space Antenna (LISA) Pathfinder [90] and the LISA candidate system [91]. The bonding process is based on a hydroxide solution (typically sodium or potassium hydroxide or sodium silicate) and requires a cleanroom environment and flat polished surfaces with an overall flatness of at least  $\lambda/10$ . While alignment of components has to be done in approximately 120 s, it takes about four weeks at ambient temperature to reach full bonding strength [92, 93].

Adhesive bonding with the two-component epoxy Hysol EA 9313 on the other hand can be performed in a laboratory environment on matte surfaces [94]. Full bonding strength is reached after five days at ambient temperature, handling strength after 8 h. Adhesive bonding was used to build e.g. the optical bench of the Jod Kamm Resonator unter Schwerelosigkeit (JOKARUS) payload [95, 96].

Another technology for building robust fiber-coupled optical modules was recently presented [97]. Beam steering is here performed by simple optical elements like plates and wedges. Fiber-to-fiber coupling based on the optical beam steering technique (OBST) has been demonstrated, but proof of suitability for (space) experiments is still pending.

Our technology, firstly presented in references [8, 9], leverages the long processing times of two light-curing adhesives. This allows for precise alignment while curing only takes 1 min once radiated at the appropriate wavelengths. With Zerodur being optically transparent at the corresponding wavelengths, we can build components sequentially, i.e. apply adhesive to inner parts of complex components and cure them in situ. The first

---

<sup>1</sup> There are now expansion class 0 SPECIAL and expansion class 0 EXTREME with CTEs in the range between  $0^\circ\text{C}$  and  $50^\circ\text{C}$  of  $(0.00 \pm 0.01) \times 10^{-6} / \text{K}$  and  $(0.000 \pm 0.007) \times 10^{-6} / \text{K}$ , respectively, but we continue to use expansion class 0 [86].

light-curing adhesive, which we use to glue optical elements like lenses or waveplates to Zerodur, is the Norland Optical Adhesive (NOA) 63. NOA 63 cures at wavelengths around 365 nm and its high viscosity allows for precise application. To glue Zerodur to Zerodur we use Fusion Flo, a nanocomposite which fills the micro-roughness between the surfaces and cures at wavelengths around 460 nm.

We use an additional adhesive, which becomes reversibly viscous when heated, in order to glue re-adjustable components such as waveplates and adjustable mirrors. Crystalbond 509 has a softening point of 71 °C and allows us to conveniently re-align components whenever necessary.

To account for CTE mismatches when gluing Non-Zerodur components to Zerodur, we use the two-component epoxy Hysol Tra-Bond F112 which can endure thermal stress.

The suitability of our technology has been demonstrated on multiple sounding rocket missions, namely FOKUS, KALEXUS and MAIUS-1. However, we have replaced components of our toolkit and added new ones for MAIUS-2/-3. We have replaced the AOMs (formerly Crystal Technology AOMO 3080-125, now MT80-A1.5-IR from AA) because of extensive beam steering effects during heat-up, and we have replaced the fiber-based optical isolators (Thorlabs IO-J-780) by free-space isolators (Medium Power Faraday Isolator from Electro-Optics Technology) due to multiple failures. To maintain a beam height of 8 mm on the optical benches, both the AOMs and the isolators are mounted in milled cutouts of the baseplate. The complete Zerodur-based optical modules for MAIUS-2/-3 are presented in the next section.

### 3.4 Zerodur-based optical modules

Based on our Zerodur technology introduced in the previous section, the fiber-coupled optical modules for MAIUS-2/-3 permit laser frequency stabilization as well as distribution, overlap and switching of laser beams. Compared to a solely fiber-based system, the use of free-space optics as part of optical benches has several advantages, including lower optical power losses along the chain of components such as AOMs or optical isolators, some flexibility in re-alignment after assembly, and easier availability of e.g. wavelength-selective components. All modules are mounted in the laser system housing on 3 mm rubber mats and fixed with screws. The through holes in the baseplates are arranged so that they bend as little as possible when tightened.

Compared to the system for MAIUS-1, one prominent innovation is the more modular approach of using multiple modules instead of only one [98]. This allows the thickness of the baseplates to be reduced (dimensions of the baseplate for MAIUS-1 210 mm × 180 mm × 50 mm) without losing mechanical stability. However, the optical modules for MAIUS-2/-3 are much more complex than the single one for MAIUS-1, not least to include the second species. But since we are using the same launch vehicle, there is an effort to facilitate SWaP budget compliance. To this end, we have developed an optical element which allows us to reduce the lengths of beam paths and thus to decrease system size and complexity. The element was implemented for the first time on the optical modules for MAIUS-2/-3 and is introduced in section 3.5.



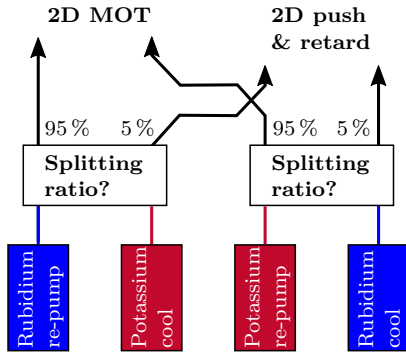


**Fig. 3.3:** There is no splitter configuration to direct 95 % of the optical power of all lasers to the 2D MOT.

which can be realized by splitters without losses. As illustrated in figure 3.3, 95 % of the optical power of all lasers must be directed towards the 2D MOT, while only 5 % is required for the push and retard beam.<sup>1</sup> Moreover, all beams must be superimposed in the same polarization state to enable polarization cleaning at the physics package.

**Table 3.1:** Optical powers (ex fiber) required at the physics package for the 2D<sup>+</sup> MOT.

Laser	2D MOT		2D push & retard		Sum
	Fiber 1	Fiber 2	Fiber 1	Fiber 2	
Rb re-pump	5 mW	5 mW	0.4 mW	0.1 mW	10.5 mW
K cool	95 mW	95 mW	8 mW	2 mW	200 mW
K re-pump	60 mW	60 mW	4 mW	1 mW	125 mW
Rb cool	95 mW	95 mW	8 mW	2 mW	200 mW

Ultimately, the superposition is realized with dichroic mirrors on the optical modules.<sup>2</sup> Chromatic aberrations of the coupling lens, however, lead to a focal difference of the beams due to the wavelength-dependent refraction (dispersion). The dependence of the refractive index  $n$  on the wavelength  $\lambda$  can be described by the Schott dispersion formula [99]:

$$n(\lambda) = \sqrt{A_0 + A_1\lambda^2 + A_2\lambda^{-2} + A_3\lambda^{-4} + A_4\lambda^{-6} + A_5\lambda^{-8}}. \quad (3.1)$$

The constants  $A_i$  are determined by least squares fits to measured data and specified by the glass manufacturers. For the plano-convex coupling lens used (Thorlabs 355230-B)

<sup>1</sup> The ratio is based on the experience of the project partners and can be justified by the low intensities required for the transfer of the atoms compared to their cooling, see section 2.3.2.

<sup>2</sup> Needless to say, the novelty here is the integration of dichroic mirrors in our technology, not the dichroic mirror itself.

Another innovation is the realization of the required power ratios for the 2D<sup>+</sup> MOT. Simultaneous cooling and manipulation of potassium and rubidium atoms requires guiding of superimposed beams with a total of four different frequencies (cool and re-pump for both species) via optical PM fibers to the physics package.  $2 \times 2$  splitters (free-space as well as fiber-based) split the input power of one port in any ratio between the two output ports, the input power of the other port in inverse ratio. For the required power ratios of the 2D<sup>+</sup> MOT, given in table 3.1, there is no configuration

with a radius of curvature  $R$  on the optical axis, the focal length is given by [100]:

$$f(\lambda) = \frac{R}{n(\lambda) - 1}. \quad (3.2)$$

The glass type being D-ZLaF52LA by CDGM [101] and  $R = 3.576$  mm [102], the focal difference between both wavelengths reads:

$$f(780.2 \text{ nm}) - f(766.7 \text{ nm}) \approx 4 \mu\text{m}. \quad (3.3)$$

In practice, the fiber end-face is aligned on the optical axis in-between the two foci. The resulting loss in coupling efficiency can be calculated based on a mode-matching model, i.e. the overlap of a virtual light field mode originating from the fiber and the one to be coupled into the fiber. Distinguishing between longitudinal, radial and angular displacements of these modes  $d$ ,  $r$  and  $\theta$  respectively, and taking into account Gaussian beam profiles as observed for the step-index fiber type used (Nufern PM780-HP) [103], the transmission is given by [8, 104]:

$$T = \frac{1}{1 + \left(\frac{\lambda d}{2\pi w^2}\right)^2} \cdot e^{-\left(\frac{r}{w}\right)^2} \cdot e^{-\left(\frac{\pi w \theta}{\lambda}\right)^2}. \quad (3.4)$$

Here  $w$  is half the mode field diameter (MFD) of the fiber. While the theoretical loss of coupling efficiency due to the chromatic aberrations at the respective wavelengths for  $w=2.5 \mu\text{m}$  with otherwise perfect coupling is below 1 %, we observe a loss of 3 % to 5 % in practice.

The superposition of light at different wavelengths for simultaneous cooling and manipulation of potassium and rubidium atoms is implemented on only two of the five scientific modules. In the following, however, all Zerodur-based optical modules for MAIUS-2/-3 are presented, differentiated by scientific and frequency reference modules.

### 3.4.1 Scientific modules

*This section is based on publication II.*

The scientific modules comprise three single-input and two double-input modules, all equipped with an optical isolator behind the collimators to prevent back reflections into the laser light source. The single-input and one of the double-input modules are located on the same level in the laser system (see section 3.2). The schematic layouts of the modules on this “Zerodur level” as a cutout of figure 3.1 are shown in figure 3.4, photos with marked beam paths can be found in publication II. The height of the baseplates was chosen so that the fibers of the double-input module (baseplate dimensions  $205 \text{ mm} \times 165 \text{ mm} \times 40 \text{ mm}$ ) can be guided and stored on plexiglass covers over the single-input modules (baseplate dimensions  $150 \text{ mm} \times 80 \text{ mm} \times 20 \text{ mm}$ ). This saves space and allows us to arrange the modules closer together. The modules have beveled edges so that they better fit into the laser system housing and the footprint is minimized.

All single-input modules (number i–iii in figure 3.4) have one input port and two output ports, providing light for the 3D MOT and detection, respectively. Two modules are

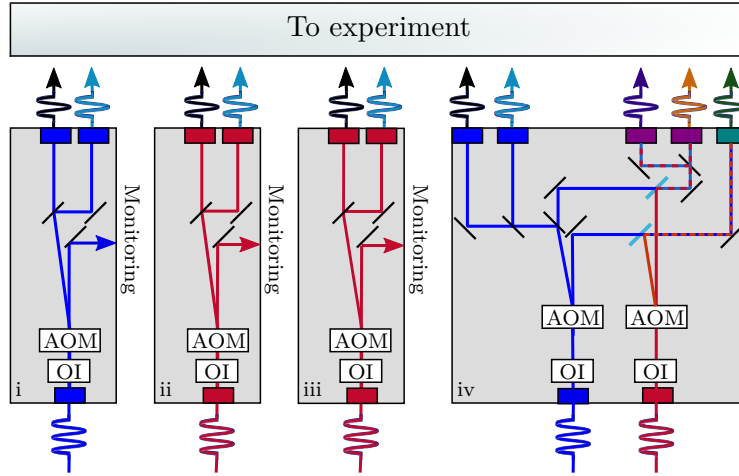


**Figure 3.4:** Schematic layouts of the optical modules on the Zerodur level. Light at 767 nm is drawn in blue, light at 780 nm in red. AOM: acousto-optic modulator; OI: optical isolator. Some components in the figure are adapted from reference [105].

operating at 767 nm, the remaining one at 780 nm. This asymmetry is again due to the additional re-pump laser for potassium, which is required to achieve the necessary beam intensities in the 2D and 3D MOT. Each module features an AOM, whereby the undiffracted beam is used for monitoring purposes while the diffracted beam is split in an adjustable power ratio for the two output ports.

The double-input module on the Zerodur level (number iv in figure 3.4) has one input port at 767 nm, one input port at 780 nm and a total of five output ports. Two of the output ports provide light with adjustable power ratio at 780 nm for the 3D MOT and detection, respectively. The remaining three output ports provide superimposed light at 767 nm and 780 nm, two times for the  $2D^+$  MOT and the last time for interferometry.

The other double-input module with baseplate dimensions  $170 \text{ mm} \times 170 \text{ mm} \times 50 \text{ mm}$ , located on the same level as the frequency reference modules (“reference level”), also has one input port at 767 nm and one input port at 780 nm, but only three output ports. All output ports provide superimposed light at 767 nm and 780 nm, two times for the  $2D^+$  MOT and the last time for interferometry. Figure 3.5 shows a photo of the module with marked beam paths together with its schematic layout as a cutout of figure 3.1.

### Characterization

The most important information with regard to the actual experiment is how much optical power can be expected at which port of the physics package at the respective wavelength. To answer this question, the power budgets of all scientific modules were thoroughly investigated. For this purpose, the optical power along the beam paths was measured to determine the splitting ratios at polarizing beam splitters (PBSs) and the individual losses of all components. The results are shown here for one of the single-input modules operating at 767 nm, of which a technical drawing with marked beam paths is shown in figure 3.6.

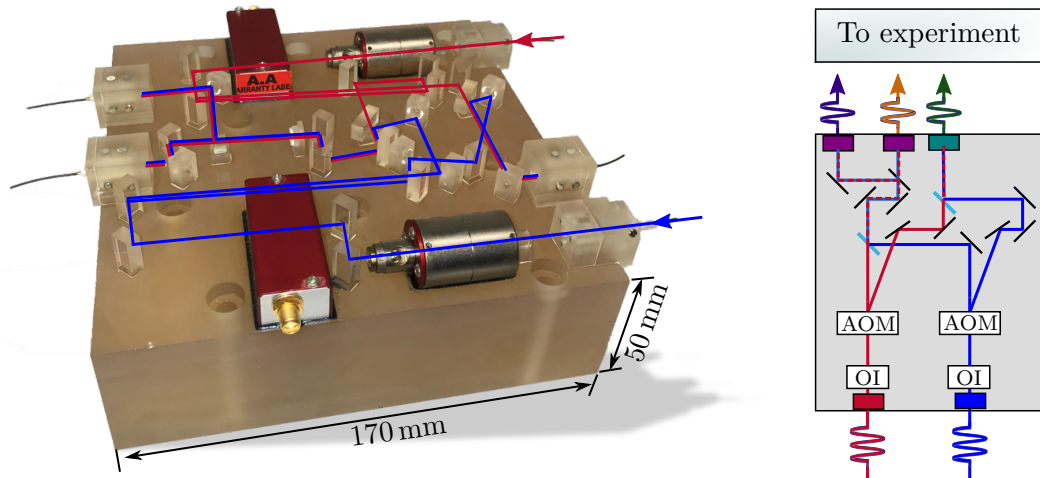


**Figure 3.5:** Photo of the double-input module on the reference level with marked beam paths (left) together with its schematic layout (right). Light at 767 nm is drawn in blue, light at 780 nm in red. The baseplate dimensions are 170 mm  $\times$  170 mm  $\times$  50 mm. AOM: acousto-optic modulator; OI: optical isolator. Some components in the figure are adapted from reference [105].

To estimate the power budget during the experiment design phase, an optical transfer of each component was assumed in the categories “maximum”, “average” and “minimum” based on manufacturer specifications and test data. This estimate together with the experimental validation is summarized in the tables 3.2 and 3.3 for beam path 1 and 2, respectively (see figure 3.6). If no physical access is possible behind one or more individual components, a joint measurement value for the transfer of several components is specified.

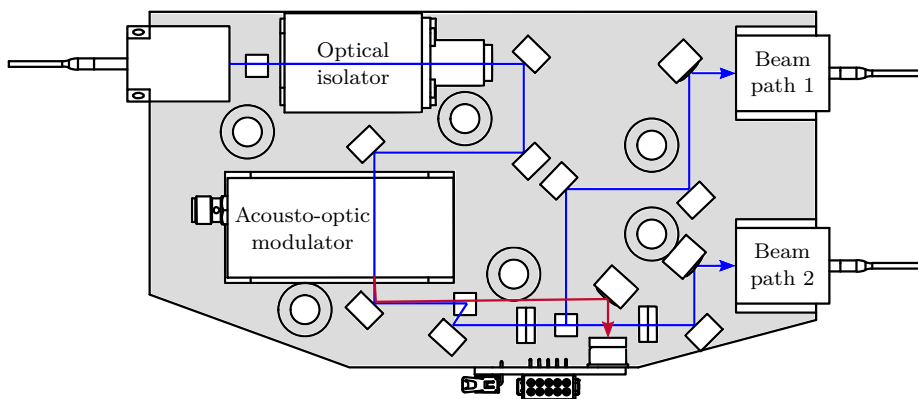


**Figure 3.6:** Technical drawing of the single-input modules with marked beam paths towards the experiment (blue) and for monitoring purposes (red).

**Table 3.2:** Estimated and measured power budget of beam path 1 of a single-input module operating at 767 nm. A joint measurement value is specified if no physical access is possible behind one or more individual components. The transmission through waveplates and the reflection of the beam separator (see section 3.5) is assumed to be loss-free. AOM: acousto-optic modulator; PBS: polarizing beam splitter.

Beam path 1	Estimate			Measurement
	Maximum	Average	Minimum	
PBS	97.0 %	95.0 %	90.0 %	} 93.3 %
Optical isolator	92.0 %	88.0 %	85.0 %	
Mirror	99.5 %	99.0 %	99.0 %	
Mirror	99.5 %	99.0 %	99.0 %	99.6 %
Mirror	99.5 %	99.0 %	99.0 %	} 82.4 %
AOM, first order	88.0 %	85.0 %	75.0 %	
Mirror	99.5 %	99.0 %	99.0 %	
Mirror	99.5 %	99.0 %	99.0 %	
PBS, reflection	76.9 %	73.9 %	67.6 %	71.7 %
Mirror	99.5 %	99.0 %	99.0 %	100.0 %
Mirror	99.5 %	99.0 %	99.0 %	98.8 %
Mirror	99.5 %	99.0 %	99.0 %	95.1 %
Fiber coupling	77.0 %	70.0 %	65.0 %	} 80.0 %
Splice	99.0 %	97.0 %	95.0 %	
Total transfer	44.2 %	32.9 %	22.1 %	41.3 %

**Table 3.3:** Estimated and measured power budget of beam path 2 (from the PBS) of a single-input module operating at 767 nm. “PBS, transmission” only includes the transmission losses, not the splitting ratio. A joint measurement value is specified if no physical access is possible behind one or more individual components. The transmission through waveplates and the reflection of the beam separator (see section 3.5) is assumed to be loss-free. AOM: acousto-optic modulator; PBS: polarizing beam splitter.

Beam path 2	Estimate			Measurement
	Maximum	Average	Minimum	
PBS, transmission	97.0 %	95.0 %	90.0 %	} 94.3 %
Mirror	99.5 %	99.0 %	99.0 %	
Mirror	99.5 %	99.0 %	99.0 %	90.0 %
Fiber coupling	77.0 %	70.0 %	65.0 %	} 66.7 %
Splice	99.0 %	97.0 %	95.0 %	
Total transfer	73.2 %	63.2 %	54.5 %	56.6 %

As can be seen in table 3.2, the measured total transfer along beam path 1 is close to the estimated maximum. In contrast, the total transfer along beam path 2 as shown in table 3.3 is at the lower end of the estimate. This can be explained with the AOM being operated at a different frequency during the measurement than during the assembly of the module. At the special request of a project partner, the AOM should not be operated with 80 MHz for both beam paths, but for one with 90 MHz. Driving the AOM at a different frequency  $f$  results in a different diffraction angle, given for the first order by

$$\theta = \frac{\lambda f}{2\nu}, \quad (3.5)$$

with  $\lambda$  being the wavelength in the crystal and  $\nu$  the acoustic velocity. The changed angle in turn reduces the fiber coupling efficiency, which cannot be fully recovered if the module was assembled using a different frequency. The advantage of different frequencies, however, is that there is no crosstalk between the paths, i.e. there is no light coupled into the fiber of beam path 1 if the AOM is operated at 90 MHz and vice versa. Recalling that beam path 1 and 2 are used for cooling and detection of the atomic clouds (see above), this prevents a disturbance of the imaging of the atoms. Furthermore, the total transfer of beam path 2 is still above the required minimum.

For the minimum specified laser power of 350 mW and based on the measured power budget, the module provides 144.7 mW for cooling and 35.0 mW for detection. Taking into account the fiber splitters (see laser system schematic in figure 3.1), this corresponds to a power per fiber of 36.2 mW for cooling and 8.8 mW for detection.

### 3.4.2 Frequency reference modules

Like many quantum technology applications, the systems for MAIUS rely on lasers, referenced to an atomic transition. Common techniques for frequency stabilization like modulation transfer spectroscopy (MTS) or frequency modulation spectroscopy (FMS) are based on saturated absorption spectroscopy. To this end, a relatively intense pump and weak probe beam from the same source are counter-propagating in a vapor cell. Atoms with velocity vectors perpendicular to the optical axis can be resonant with both beams simultaneously. If the laser frequency is tuned to the resonance, atoms excited by the pump beam show reduced absorption of the probe beam, giving rise to features known as Lamb dips in transmission.

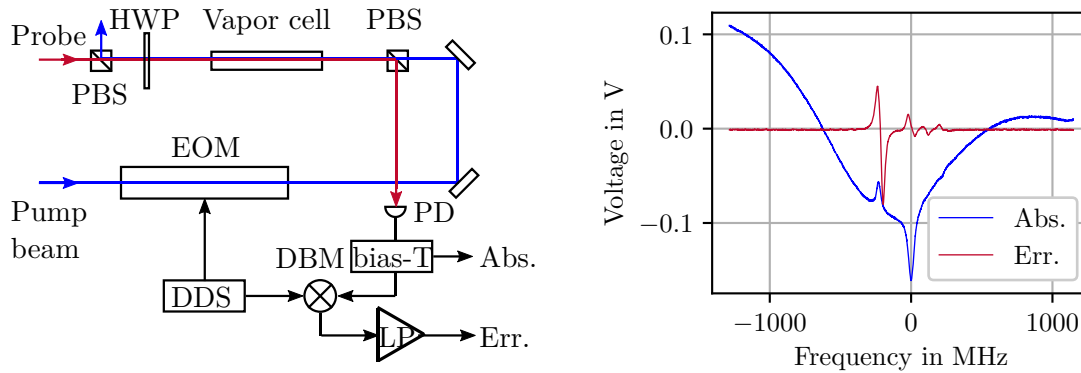
By phase modulation of either the pump or the probe beam, an electronic frequency discriminant for laser stabilization can be generated, similar to the Pound-Drever-Hall method for stabilizing lasers to optical cavities [106–108]. Depending on whether the pump or the probe beam is modulated, the method is known as MTS or FMS.

Both methods MTS and FMS have been thoroughly investigated for potassium and rubidium [109–113] and are briefly discussed in the following, before presenting the hardware implementation in the form of the Zerodur-based frequency reference modules for MAIUS-2/-3.

### Modulation transfer spectroscopy

A schematic setup for MTS is depicted in figure 3.7(a). The counter-propagating pump and probe beam are orthogonal linear polarized. The pump beam is modulated using an EOM, driven by direct digital synthesis (DDS).

The probe beam is detected on a photodiode, and a bias-T separates low and high frequency components of the electrical signal. The low frequency part representing the saturated absorption spectrum is directly monitored while the high frequency part is mixed down with the DDS signal and filtered to generate the heterodyne or error signal.



(a) Schematic setup for MTS with modulated pump beam (blue) and unmodulated probe beam (red). DBM: double-balanced mixer; DDS: direct digital synthesis; EOM: electro-optic modulator; HWP: half-wave plate; LP: low pass filter; PBS: polarizing beam splitter; PD: photodiode.

(b) Comparison of saturated absorption signal (Abs.) and error signal (Err.) using potassium as example. The cell was heated to 55 °C at the windows, modulation voltage  $U_{\text{EOM}} = 600 \text{ mV}_{\text{RMS}}$  at 12.5 MHz.

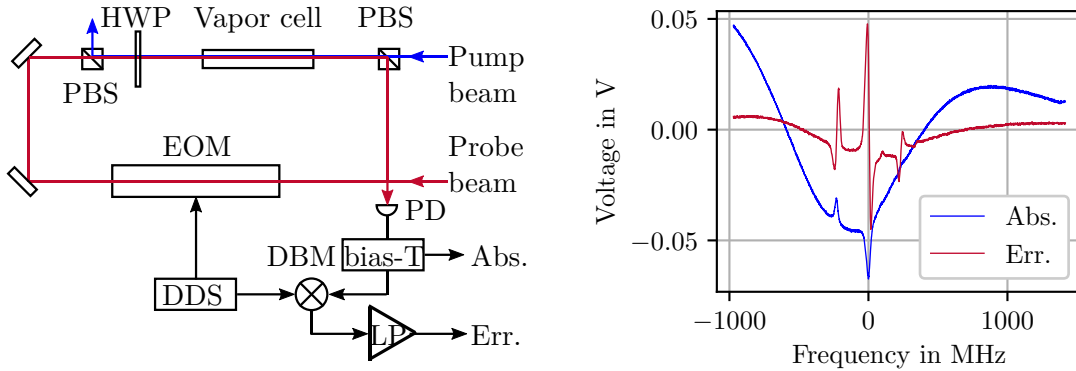
**Figure 3.7:** Schematic MTS setup and signals using potassium as example.

A typical saturated absorption signal and respective error signal using potassium as example is shown in figure 3.7(b). To acquire the signals, a laser (Toptica Photonics DL pro) was scanned in frequency across the atomic transitions. The temperature of the vapor cell (VC-K-09-50-Q from Sacher Lasertechnik) was stabilized with a home-built heating to 55 °C at the windows. The electro-optic modulator (Photline NIR-MPX800) was driven with  $U_{\text{EOM}} = 600 \text{ mV}_{\text{RMS}}$  at 12.5 MHz by a DDS-based frequency generator (Rigol DG1022) which allowed adjustment of the phase between the local oscillator and the photodiode signal. The silicon photodiode with 500 MHz bandwidth (Hamamatsu S5972) was mounted on a home-built printed circuit board (PCB) with low and high frequency ports, where the high frequency port was connected to a mixer (Mini-Circuits ZFM-3-S+) and subsequent low pass filter with cutoff frequency 1.9 MHz (Mini-Circuits SLP-1.9+). The probe beam power was adjusted to approximately 140  $\mu\text{W}$ .

As can be seen in figure 3.7(b), the error signal shows no Doppler background which can be explained by the four-wave mixing of the pump and probe beam [109]. Also, the signal is strongest on  $^{39}\text{K}$ ,  $F = 2 \rightarrow F'$ , where  $F = x \rightarrow F'$  indicates the set of transitions from state  $x$  in the manifold of excited states (which cannot be resolved individually). The frequency axis was calibrated using the absorption spectrum, and the ground state crossover  $F = 1,2 \rightarrow F'$  was set to zero.

### Frequency modulation spectroscopy

Apart from the modulation of the probe beam, the FMS setup is identical to that for MTS (see figure 3.8(a)). Moreover, the same components have been used to acquire the signals shown in figure 3.8(b). The modulation voltage was set to  $U_{\text{EOM}} = 600 \text{ mV}_{\text{RMS}}$  at 12.5 MHz and the probe beam power was adjusted to approximately  $30 \mu\text{W}$ .



(a) Schematic setup for FMS with unmodulated pump beam (blue) and modulated probe beam (red). All notations are as in figure 3.7(a).

(b) Comparison of saturated absorption signal (Abs.) and error signal (Err.) using potassium as example. The cell was heated to  $55^\circ\text{C}$  at the windows, modulation voltage  $U_{\text{EOM}} = 200 \text{ mV}_{\text{RMS}}$  at 12.5 MHz.

**Figure 3.8:** Schematic FMS setup and signals using potassium as example.

The error signal looks like the derivative of the absorption signal and is therefore a suitable frequency discriminant as it is almost linear around the lock point. Compared to MTS, however, the signal shows more Doppler background which causes a shift of the lock point. The signal is strongest on the ground state crossover transition  $^{39}\text{K}$ ,  $F = 1,2 \rightarrow F'$ , which in turn is set to zero on the frequency axis. Note that the ordinate axis is scaled differently than for MTS in figure 3.7(b).

### Zerodur-based implementation

One Zerodur-based reference module provides a frequency reference for each of the two species. Both modules have the same design and use the same components, except for the cell assembly. To increase the vapor pressure inside the potassium cell, a resistance wire is used as heater and thermistors can be employed to stabilize the temperature. A photo of both frequency reference modules with marked beam paths is shown in figure 3.9, the footprint of each baseplate being  $150 \text{ mm} \times 40 \text{ mm}$ .



Light for the two counter-propagating spectroscopy beams is guided to the modules via optical fibers, the light in one fiber being modulated by a fiber-based EOM. After collimation, polarizers minimize power fluctuations in both beams and units of half-wave plates (HWPs) and PBS allow the adjustment of beam power. In contrast to the schematics in figures 3.7(a) and 3.8(a), two quarter-wave plates on each side of the vapor cell instead of one half-wave plate rotate the polarization planes. Due to the combined rotation by  $90^\circ$ , the beams are reflected at the subsequent PBS and directed onto PCBs with photodiodes, provided by project partners from HUB. Since the signals of both beam paths are recorded, FMS and MTS can be performed (simultaneously). However, the beam power levels must be adjusted accordingly for a maximum signal-to-noise ratio (SNR).

Similar to the physics package (see section 2.3.2), changing external magnetic fields during the flight can result in unwanted shifts of transition frequencies. The vapor cells are therefore embedded in a magnetic shielding made of mu-metal. Estimates of the frequency shift indicate that this is probably not necessary [114]. We have nevertheless opted for a shielding as the impact on the SWaP budget is negligible.

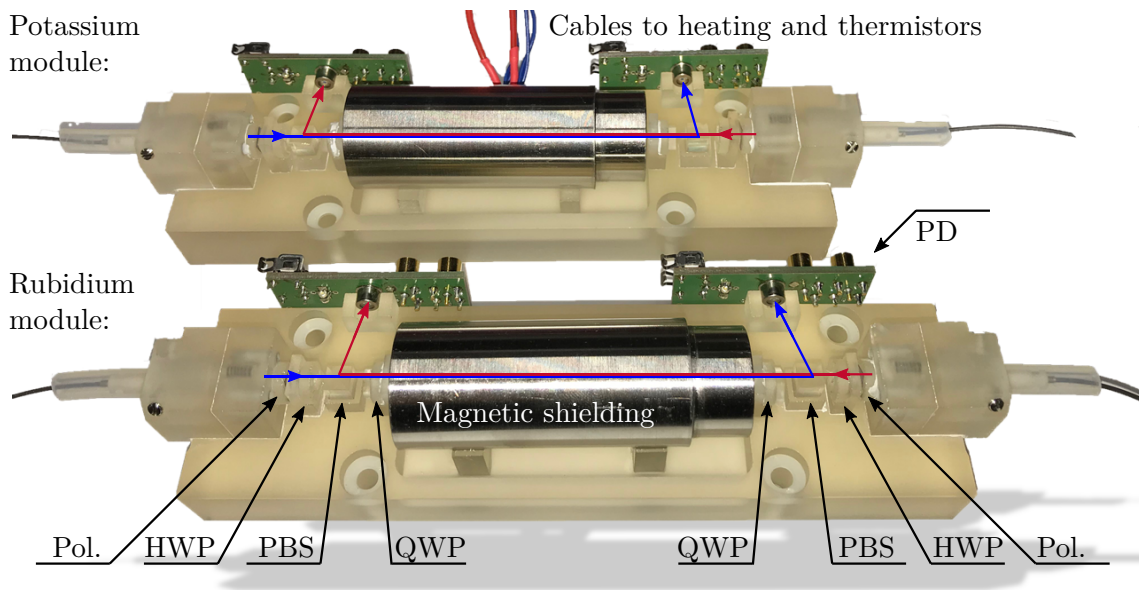


**Figure 3.9:** Photo of the frequency reference modules for MAIUS-2/-3 with marked beam paths. The footprint of each baseplate is  $150\text{ mm} \times 40\text{ mm}$ . HWP: half-wave plate; PBS: polarizing beam splitter; PD: photodiode; Pol.: polarizer; QWP: quarter-wave plate.

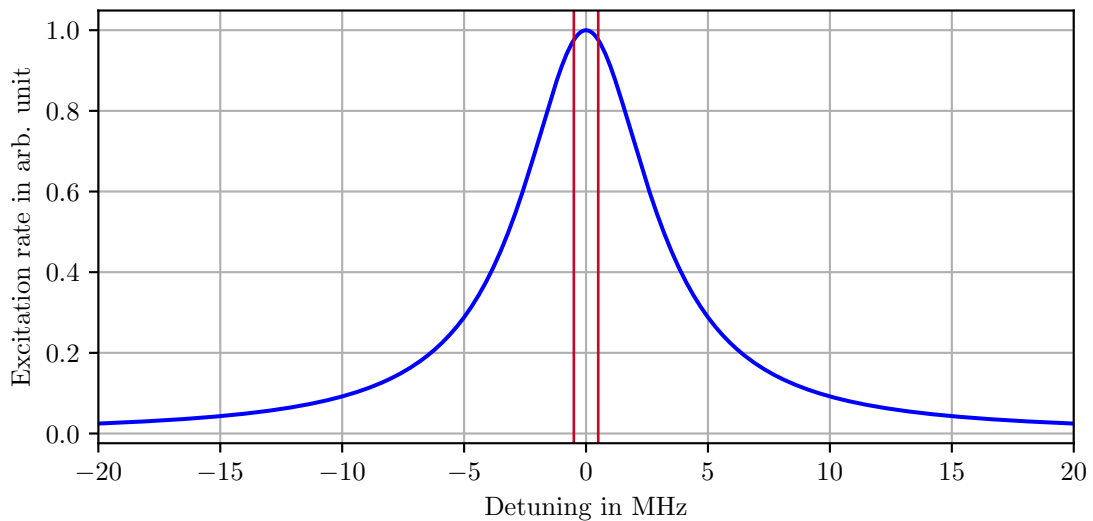
### Characterization

Figure of merit of frequency reference systems is the frequency stability. Since no requirements are defined for the MAIUS systems, the relative stability of  $3 \times 10^{-9}$  required for BECCAL as defined in the systems requirements document (SRD) is used as benchmark. The relevant time scale is the length of the flight with a few 100 s (see section 2.2.2).

A stability of  $3 \times 10^{-9}$  can be justified by translating it into variations of the number of atoms imaged in the BEC. For this purpose, one can first determine the frequency fluctuation range by multiplying the required stability with the absolute transition frequency of the transitions used for frequency stabilization ( $^{39}\text{K D}_2$ ,  $F = 2 \rightarrow F'$  and  $^{85}\text{Rb D}_2$ ,  $F = 3 \rightarrow F' = 4$ ). Transition frequencies of 391.016 THz (potassium) [115] and 384.229 THz (rubidium) [116] both result in a fluctuation range of about 1 MHz. As a large portion of atoms in a BEC occupies the ground state, the number of atoms excited by the detection pulses scales with the resonant photon scattering rate (excitation rate) of the imaging transition<sup>1</sup>, given in a two-level system by [71]:

$$\gamma = \frac{s_0 \Gamma / 2}{1 + s_0 + (2\delta / \Gamma)^2}. \quad (3.6)$$

Here  $s_0 = I/I_s$  denotes the on-resonance saturation parameter,  $\delta$  the detuning and  $\Gamma$  the natural linewidth of the respective transition. The excitation rate is a Lorentzian distribution, shown in figure 3.10 as a function of the detuning.

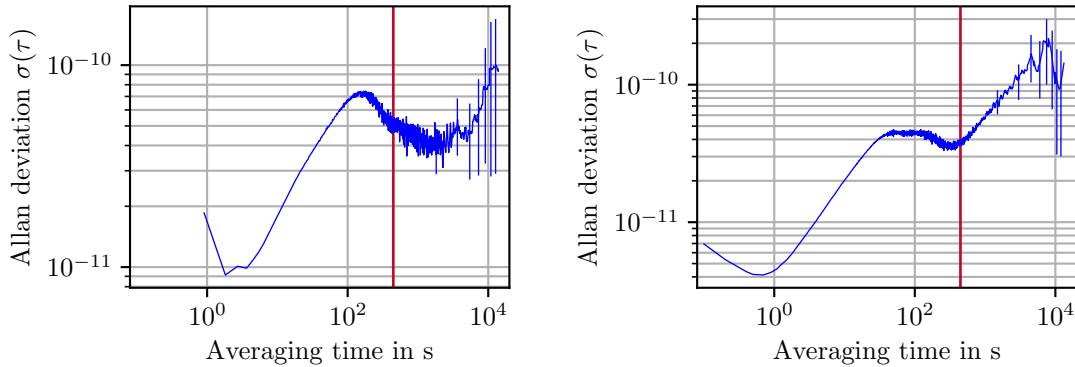


**Figure 3.10:** Normalized excitation rate of a two-level system as a function of detuning for  $s_0 = 0.1$  and  $\Gamma = 6.0666$  MHz ( $^{85}\text{Rb D}_2$  line). Vertical lines indicate a detuning of  $\pm 0.5$  MHz.

<sup>1</sup> More precisely, the number of excited atoms scales with the convolution of the excitation rate and the laser linewidth. However, since the (technical) linewidth of the lasers used for detection is only a few 10 kHz [81], it can be neglected at first approximation.

The number of atoms excited by the detection pulses can be calculated by comparing the values on the ordinate within the frequency fluctuation range. For natural linewidths of 6.035 MHz ( $^{39}\text{K D}_2$ ) and 6.0666 MHz ( $^{85}\text{Rb D}_2$ ), the values at  $\pm 0.5$  MHz as indicated by the vertical lines in figure 3.10 are approximately 97.6 % of the maximum, i.e. a frequency fluctuation range of 1 MHz corresponds to variations of the atom number of less than 3 %. Therefore, the required frequency stability of  $3 \times 10^{-9}$  seems a reasonable order of magnitude.

The frequency stability has been experimentally determined by recording the beat note frequency of the systems for MAIUS-2/-3 and laboratory systems. For this purpose, the Zerodur-based frequency reference modules and the corresponding lasers were screwed into the laser system housing and the laser light frequency-stabilized on the MTS signals of the respective atomic transitions (see above). Part of the light was superimposed with light from frequency-stabilized laboratory lasers and the beat note frequency was recorded over several hours. As the most common time domain measure of frequency stability [117], the Allan deviation of the beat note frequency was calculated. The results are shown in figure 3.11(a) and 3.11(b).



(a) Allan deviation of the beat note frequency of the potassium system and a laboratory system as a function of averaging time (blue) and expected flight duration (red).

(b) Allan deviation of the beat note frequency of the rubidium system and a laboratory system as a function of averaging time (blue) and expected flight duration (red).

**Figure 3.11:** Allan deviations as a measure of frequency stability of the frequency reference systems for MAIUS-2/-3 and expected flight duration (lift-off until beginning of atmospheric re-entry according to table A.1).

As can be seen in figure 3.11, the relative frequency stability of both the potassium and the rubidium system is well below  $1 \times 10^{-10}$  within the expected flight duration, and therefore complies with the BECCAL requirements.

With the measurement setup used, however, it cannot be determined whether the frequency stability is limited by the MAIUS or the laboratory systems and therefore represents an upper limit.

### 3.5 Separating superimposed beams which only differ in angle

*This section is a summary of publication I.*

In response to the growing need for ever more compact systems, we have developed an optical beam splitter (“beam separator”) for the separation of superimposed beams which only differ in angle. A typical use case is the separation of superimposed beams of different diffraction orders directly behind AOMs, where the angle between two diffraction orders is only about  $1^\circ$  for an 80 MHz-AOM in the near-infrared. While the conventional approach of spatial separation in this case requires a beam path in the order of at least 10 cm (beam waist 0.5 mm, separation by twice the waist), the space required when using the beam separator is limited to its size of less than 1 cm edge length.

The beams are angularly resolved and separated by total internal reflection at an air gap between two prisms. When tuned to the critical angle of total internal reflection, the beam of one diffraction order is reflected at the interface between the first prism with index of refraction  $n_1$  and the air gap with index of refraction  $n_2 < n_1$  (see figure 3.12 for a schematic top view). The beam of the other diffraction order is refracted according to Snell’s law. When entering the second prism, this beam is refracted again in the original direction of propagation and hence transmitted through the beam separator.

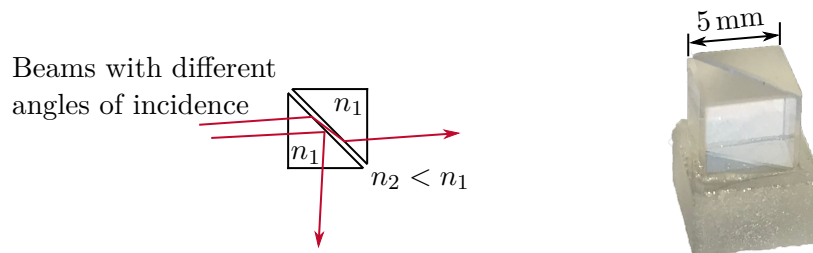


**Figure 3.12:** Schematic top view and a photo of the beam separator on a Zerodur base. Adapted from publication I.

As part of the publication, we have produced a beam separator with an edge length of 5 mm and an operating wavelength of 800 nm. However, both the component size and the operating wavelength can easily be adapted as they only depend on the prism size and the coating, respectively. To ensure a fixed width of the air gap (of  $125 \mu\text{m}$ ), we have glued the prisms on a Zerodur base, a photo of which is depicted in figure 3.12.

The reflected beam is completely reflected regardless of the polarization, i.e. there is no crosstalk in transmittance. The transmitted beam, however, is not only refracted but also reflected when leaving the first prism and entering the second one according to Fresnel equations (see figure 3.13). We have developed an anti-reflection (AR) coating to suppress these reflections at the critical angle from over 60 % to below 1 %. Thanks to this AR coating, we achieve a

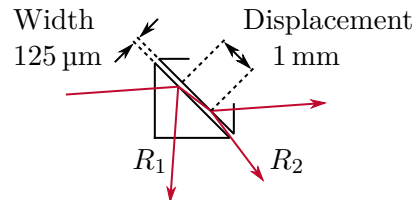


**Fig. 3.13:** Unwanted reflections  $R_1$  and  $R_2$  of the transmitted beam when leaving the first prism and entering the second. Adapted from publication I.

maximum transmittance of over 90% at the operating wavelength. The measured transmittance spectrum together with the calculated spectrum is shown in figure 3.14. The calculated spectrum is given by the squared transmittance of the AR coating at the incidence angle of minimum reflectance ( $41.1^\circ$ ) and was computed using OpenFilters [118].

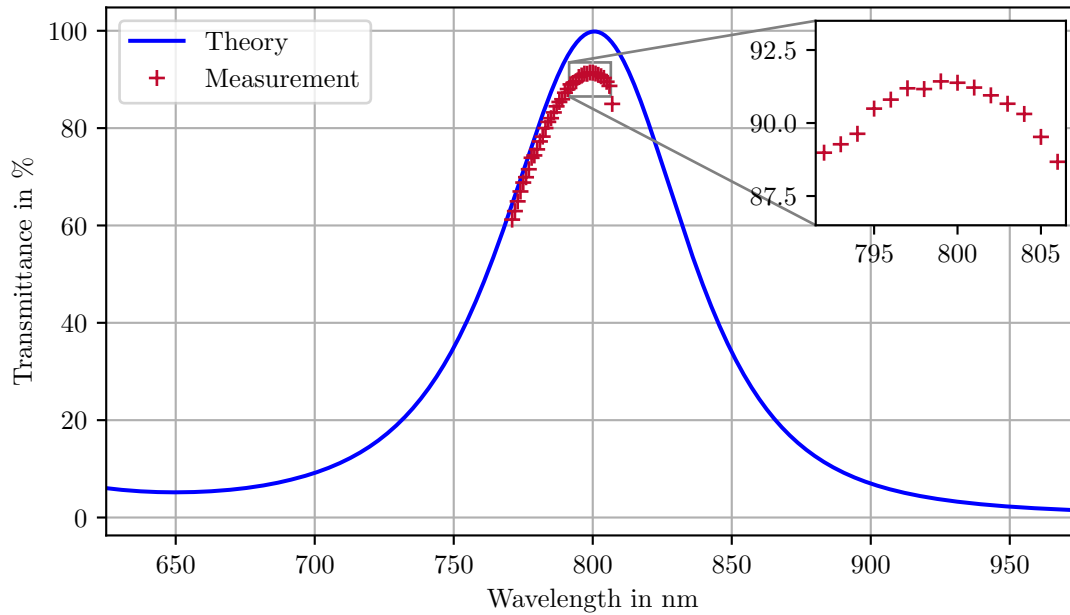


**Figure 3.14:** Calculated and measured transmittance spectrum of the beam separator. Adapted from publication I.

The beam separator was implemented for the first time on the single-input Zerodur-based optical modules for MAIUS-2/-3 (see section 3.4.1). In contrast to the version produced for publication I, however, the beam separators for MAIUS-2/-3 are designed for operating wavelengths of 767 nm and 780 nm.



# CHAPTER 4

---

## Technology development for future applications

---

So far the missions MAIUS-2 and MAIUS-3 have been presented. The launch vehicle and flight parameters have been introduced and the SWaP budget and stability requirements derived. On this basis, the scientific payload in general and the laser system in particular have been discussed in detail, including the Zerodur-based optical modules and respective developments.

In this chapter, early-stage developments and proof of concepts for future applications independent of MAIUS are presented. Although there are proposals for applications (see chapter 5), the developments have not yet been implemented in experiments.

The first development is a technique for simultaneous laser frequency stabilization on multiple transitions of different atomic species with a single optical setup. Furthermore, current efforts to build Zerodur-based vacuum systems are presented. The miniaturization of the chamber in combination with our laser system technology would allow for highly robust and fully integrated quantum optical systems on a single technological basis for space and other adverse environments.

### 4.1 Simultaneous spectroscopy on transitions of multiple atomic species

*This section is a summary of publication III.*

Inspired by the observation of spectroscopic rubidium features in a potassium vapor cell, we have developed a technique for simultaneous heterodyning on multiple transitions of different atomic species with a single optical setup. The technique is intended for laser frequency stabilization in multi-species experiments where every species and transition requires a frequency reference, i.e. a dedicated optical setup for heterodyne detection. By reducing the number of components, we facilitate compact and robust systems with less complexity and susceptibility to failures.

As a proof of concept, we demonstrate heterodyne detection of the potassium  $D_1$ ,  $D_2$  and rubidium  $D_2$  transitions on a single photodiode simultaneously. We use a potassium vapor cell, which also contains atomic rubidium, with a heating to increase the vapor pressure and thus the signal-to-noise ratio. The signals are separated by modulation/demodulation at different frequencies and electronic filtering. As MTS and FMS only differ in which beam is modulated, our technique works equally well for both methods. However, we demonstrate the principle using the example of MTS.

Based on the setup shown in figure 3.7(a), a schematic of our setup is depicted in figure 4.1. The light of three lasers (two home-built DFB lasers with diodes from eagleyard Photonics and one Toptica Photonics DL pro) at 770.1 nm, 766.7 nm and 780.2 nm is coupled into PM fibers to excite the corresponding potassium  $D_1$ ,  $D_2$  and rubidium  $D_2$

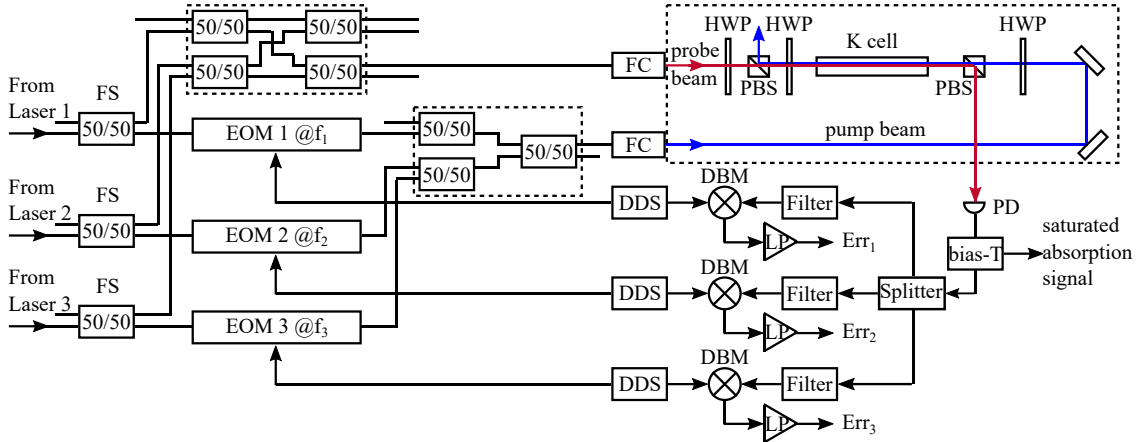


**Figure 4.1:** Schematic setup for simultaneous MTS of the potassium  $D_1$ ,  $D_2$  and rubidium  $D_2$  transitions. DBM: double-balanced mixer; DDS: direct digital synthesis; EOM: electro-optic modulator; FC: fiber collimator; FS: fiber splitter; 50/50: splitting ratio; HWP: half-wave plate; LP: low pass filter; PBS: polarizing beam splitter; PD: photodiode. Adapted from publication III.

transitions, respectively. The separation of the individual pump and probe beams as well as the superposition of all pump and all probe beams is realized by fiber splitters (Evanescence Optics 954P), the pump beams being guided through fiber EOMs (Photline NIR-MPX800) before the superposition. The electro-optic modulators are driven by DDS-based frequency generators (Rigol DG1022) at modulation frequencies of 4.5 MHz, 11.5 MHz and 16 MHz.

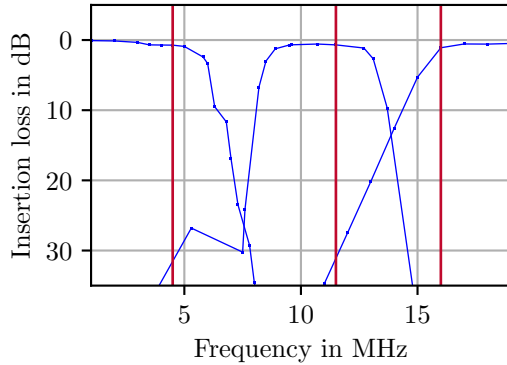


**Fig. 4.2:** Modulation frequencies (red) and corresponding filter spectra (blue) as per the data sheets to separate the PD signals for simultaneous heterodyning on multiple transitions.

The chosen modulation frequencies allow the high frequency components of the photodiode signal to be separated with standard Mini-Circuits filters and are not multiples of each other. We use the low, high and band-pass filter Mini-Circuits BLP-5+, SHP-20+ and SBP-10.7+, respectively. A plot of the filter spectra as per the data sheets with marked modulation frequencies is shown in figure 4.2.

The superimposed pump and probe beams are guided to a single free-space optical setup which is nearly identical to the one shown in figure 3.7(a). In fact, the collimated beams pass the same cell assembly including the heating, the temperature at the windows being  $65^\circ\text{C}$ . The only difference between the free-space setups are two additional half-wave plates to allow for power adjustments of the pump and probe beams, and the photodiode used (here: Thorlabs PDA10A-EC with 150 MHz bandwidth). In contrast to single-frequency heterodyning, we



use a three way power splitter (Mini-Circuits ZFSC-3-1W-S+) behind the bias-t (Mini-Circuits ZFBT-6GW+) to split the high frequency signal. Each of the high frequency signals then passes a low, high or bandpass filter corresponding to the modulation frequency (see above). By amplification (Mini-Circuits ZFL-500+), mixing (Mini-Circuits ZFM-3-S+) with the respective local oscillator and filtering (Mini-Circuits SLP-1.9+), the three individual error signals are generated.

In our setup, the power ratios between pump and probe per laser are predetermined by the splitting ratios of the fiber splitters and cannot be optimized individually. However, this is a limitation due to our setup, not the technique itself, and we can still adjust the power by free-space optics for all pump and all probe beams together. As the power ratios are a trade-off between power broadening and SNR of the error signals, we set the pump/probe powers to 0.5 mW/1 mW for K D<sub>1</sub> and 1 mW/2 mW for K D<sub>2</sub> and Rb D<sub>2</sub>.

By scanning the laser frequencies across the respective atomic transitions and optimizing the phases between local oscillators and photodiode signal, we were able to acquire the spectra shown in figure 4.3. As expected, the saturated absorption spectrum in figure 4.3(a) is a superposition of the individual spectra where the D<sub>1</sub> and D<sub>2</sub> transitions of the most abundant potassium isotope <sup>39</sup>K can be easily identified. The scan range of the rubidium D<sub>2</sub> transition was chosen so that only the  $F = 2 \rightarrow F'$  of <sup>87</sup>Rb and  $F = 3 \rightarrow F'$  of <sup>85</sup>Rb set of transitions are visible for the sake of clarity.

The isolated error signals are shown in figure 4.3(b)-4.3(d). The main peak of K D<sub>1</sub> can be identified as the crossover  $F = 1,2 \rightarrow F'$  transition which is set to zero on the frequency axis. As already shown in figure 3.7(b), the K D<sub>2</sub> signal is strongest on the transition  $F = 2 \rightarrow F'$ , but the ground state crossover  $F = 1,2 \rightarrow F'$  (at zero) and the  $F = 1 \rightarrow F'$  set of transitions can be identified as well. In the error signal of Rb D<sub>2</sub>, the closed transition  $F = 2 \rightarrow F' = 3$  of <sup>87</sup>Rb is set to zero on the frequency axis while the transition  $F = 3 \rightarrow F' = 4$  of <sup>85</sup>Rb is also clearly visible.

In conclusion, we successfully demonstrated simultaneous heterodyning on multiple transitions of different atomic species for laser frequency stabilization with a single optical setup. Referring to the frequency reference modules for MAIUS-2/-3 (see section 3.4.2), one module would have been sufficient to provide the necessary frequency reference for both species (given the electronic system supports modulation/demodulation at appropriate frequencies). Alternatively, one of the modules could have been used as redundancy with appropriate guiding of light at the different wavelengths. In principle, an improvement in signal-to-noise ratio can also be expected when using vapor cells filled with all required atomic species, whereas our cell was intended for potassium spectroscopy only.

We are now focusing on developments not only independent of MAIUS, but also beyond laser systems. Many quantum applications require a vacuum system and given our experience with Zerodur-based systems, the question raises whether vacuum chambers can be built from Zerodur. We address this question in the next section.

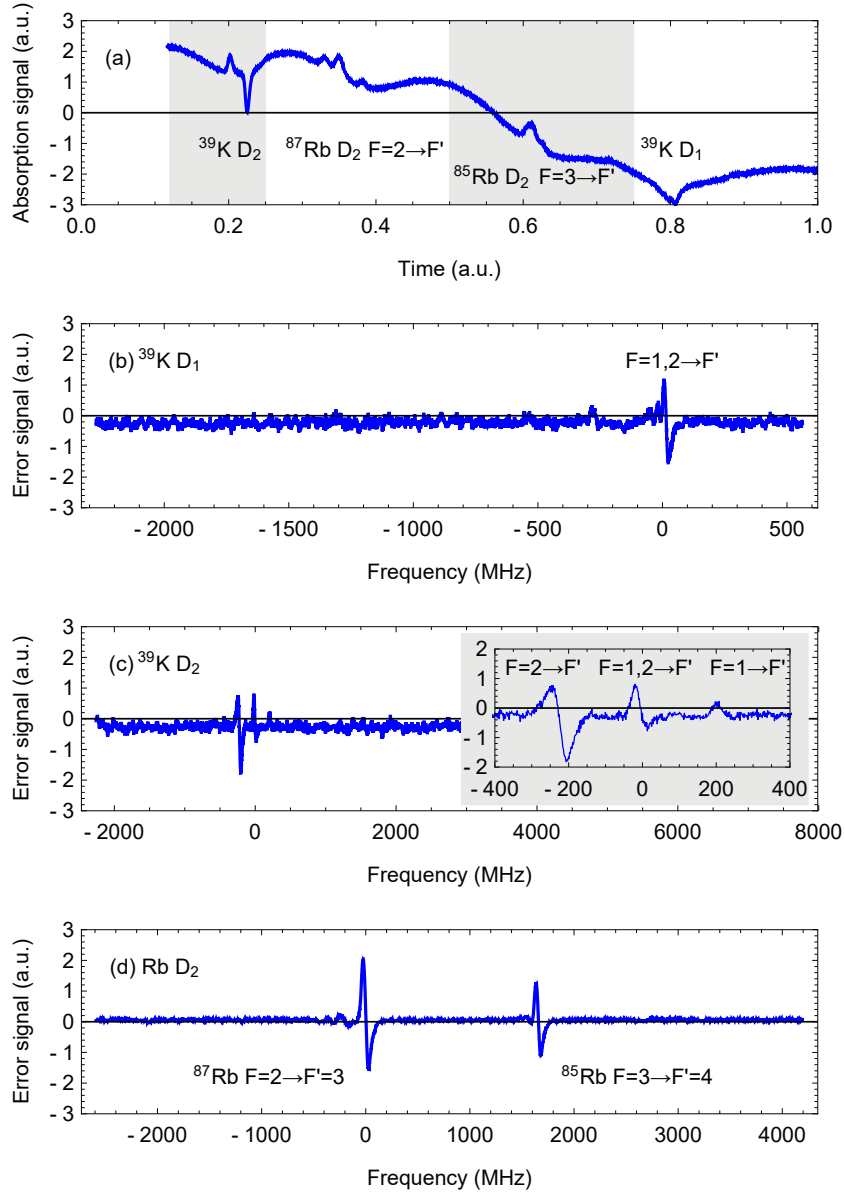


**Figure 4.3:** Comparison of saturated absorption signal and error signals of the potassium  $\text{D}_1$ ,  $\text{D}_2$  and rubidium  $\text{D}_2$  transitions. The cell was heated to  $65^\circ\text{C}$  at the windows, modulation voltages  $U_{\text{EOM}} = 800 \text{ mV}_{\text{RMS}}$  at 4.5 MHz (K  $\text{D}_1$ ), 11.5 MHz (Rb  $\text{D}_2$ ) and 16 MHz (K  $\text{D}_2$ ), respectively. Adapted from publication III.

## 4.2 Zerodur-based vacuum systems

*This section is based on work carried out as part of a master's thesis [119]. Results have been presented at the 70th International Astronautical Congress, 21-25 October 2019, Washington, D.C., United States [120].*

In addition to a laser system, many quantum applications require a high vacuum (HV) ( $10^{-3}$  mbar– $10^{-8}$  mbar [121]) or ultra-high vacuum (UHV) ( $10^{-8}$  mbar– $10^{-11}$  mbar [121]) environment. The vacuum environment shields the quantum systems like cold atomic gases or trapped ions against external influences, but also increases the mean free path and thereby reduces collisions. Building on our experience with laser systems, we are expanding our repertoire to include Zerodur-based vacuum systems. The combination of optical and vacuum systems on a single technological platform allows the development of highly robust and fully integrated quantum optical systems.

Zerodur is not only characterized by a negligible CTE and high mechanical stability, but is also electrically non-conductive and therefore does not interfere with applied magnetic fields. Furthermore, the helium permeability of Zerodur compared to other low expansion glasses is more than two orders of magnitude lower than the permeability of Ultra-Low Expansion (ULE) glass and fused silica [84]. The helium permeability is a good indicator for vacuum suitability as helium easily diffuses through materials.

There have already been attempts to realize quartz- and even Zerodur-based vacuum chambers, using different bonding techniques (see section 3.3) to connect windows and pumps to a quartz or Zerodur chamber [122–124]. The quartz or Zerodur metal transition at the pump connection, however, exhibits a CTE mismatch which can lead to mechanical stress especially under varying temperatures e.g. during bake-out. The omission of active pumps, and eventually all flange connections and feedthroughs, allows one to avoid this mismatch and permits further miniaturization of the chamber and the overall system, while providing improved optical access. The feasibility of miniaturized and integrated, i.e. flange-less, quantum optical systems as well as the maintenance of a sealed UHV environment for at least 1000 days was intensively studied [125]. Integrated systems have even been realized [126], yet not based on Zerodur.

Our goal is to combine the favorable properties of Zerodur with the advantages of an integrated system to build a quantum sensor demonstrator. Before building a flange-less Zerodur chamber, tests regarding the vacuum suitability of Zerodur-based systems in general are necessary. Therefore, we have set up two chambers with different flange designs, presented hereafter.

### 4.2.1 Zerodur vacuum chambers

The first step on the way to an integrated system is to investigate how optical components like windows can be connected vacuum-tight to a Zerodur chamber. The measurement of pressure curves and leak rates, however, requires connection to a traditional pumping system and this in turn requires a flange. As the brittleness of Zerodur forbids traditional sealing concepts like copper gaskets, new developments are necessary for both the flange and the gaskets of flanges and windows. Moreover, the Zerodur metal transition forces a CTE mismatch which must be taken into account in the flange design. Another design criterion is the miniaturizability of the chamber and flange.

Two different flange designs as part of Zerodur vacuum chambers of the same size are presented, one screw-based and detachable, the other one epoxy-based and non-detachable but miniaturizable. We have designed dedicated metal counterparts in the form of an adapter for both designs. Opposite the Zerodur metal transition, the adapters feature a ConFlat (CF) flange for connection to pumps and pressure sensors. Connected to a pumping system, the chambers serve as test platform for leak tests of the window and flange connections.

#### Screw-based flange design

The detachable screw-based flange is inspired by a CF DN16 flange featuring a bolt circle for six M4 screws. The contact surface, however, is plane and the outer diameter of the flange is 42 mm. The flange is designed as part of a cuboid Zerodur chamber of  $50\text{ mm} \times 50\text{ mm} \times 70\text{ mm}$  with a cylindrical cutout of 32 mm diameter running through the chamber volume. The tube connecting the flange with the chamber has an outer diameter of 22 mm and an inner diameter of 12 mm. A cutout opposite the flange serves as recess for a window of 40 mm diameter. An illustration of the flange and a photo of the chamber with mounted adapter are shown in figure 4.4.

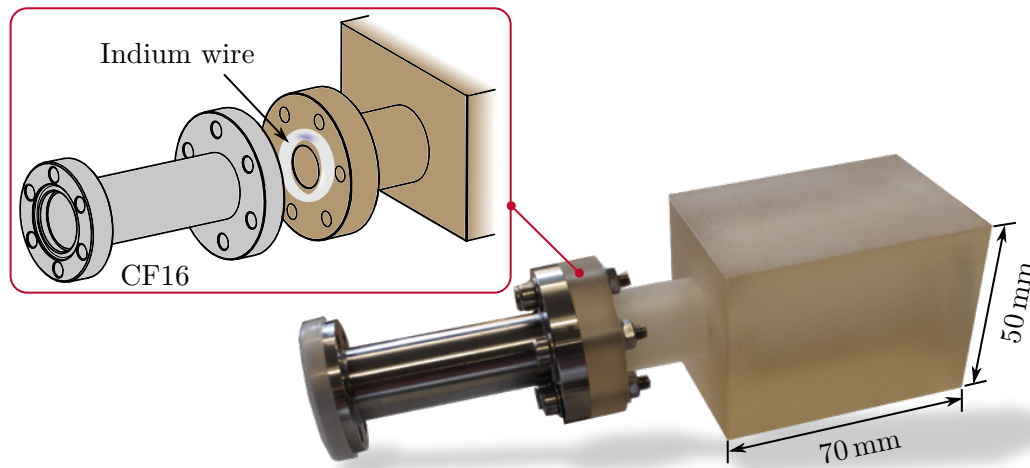


**Figure 4.4:** Illustration of the screw-based flange and photo of the Zerodur chamber with mounted metal adapter, the cuboid dimensions being  $50\text{ mm} \times 50\text{ mm} \times 70\text{ mm}$ . Photo reprinted from reference [119].

We use an O-ring shaped indium wire (0.5 mm diameter) as gasket between the plane Zerodur flange and its metal counterpart. The six M4 screws were tightened with increasing torque from 0.1 Nm to 0.6 Nm over several days.

To glue the window, we used NOA 63 which we already successfully used to glue optical components in the context of our laser system technology (see section 3.3). As a light-curing adhesive, NOA 63 allows check of the adhesive layer for air ducts prior to curing. For first tests we used simple glass (N-BK7) windows.

After assembly, we connected the chamber to a turbomolecular pump (Agilent TwisTorr 304 FS, pumping speed 300 l/s) for evacuation and bake-out. The bake-out temperature

is limited by the maximum temperature of 60 °C NOA 63 can withstand, while only temperatures above 130 °C affect the CTE of Zerodur [127]. The achieved background pressure of  $7 \times 10^{-9}$  mbar is in the same order of magnitude as the reference pressure measured with a blind flange, i.e. the pumping rate exceeds the leak rate of the chamber. To directly measure leak rates of the flange and the window connection, we used a helium leak detector. While the leak rate at the window connection corresponded to the reference leak rate without sprayed helium of  $1 \times 10^{-10}$  mbar l/s, the flange connection showed an increased leak rate of  $4 \times 10^{-8}$  mbar l/s. However, we were able to achieve the reference leak rate by embedding the indium wire gasket in a polymer.

### Conical flange design

The second flange is conical and again designed as part of a cuboid Zerodur chamber with the same dimensions as the first one. An illustration of the flange and a photo of the chamber with mounted adapter are depicted in figure 4.5. The Zerodur part of the flange is a cone with a half aperture angle of 2°. The metal counterpart on the other side has an angle of 5° leading to a gap between Zerodur and metal, which we fill with a heat-curing low outgassing epoxy (EPO-TEK 353ND). While the connection is therefore non-detachable, the small contact area of Zerodur and metal minimizes the risk of breaking the Zerodur and the design allows further miniaturization.

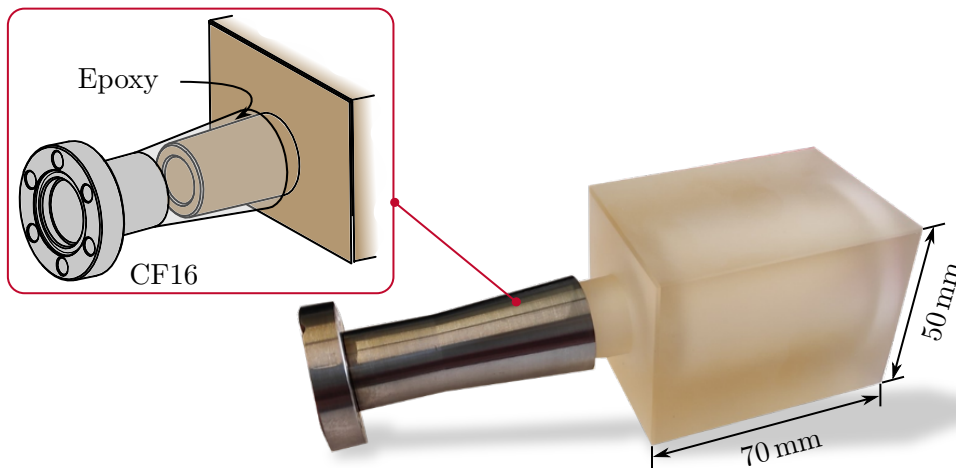


**Figure 4.5:** Illustration of the conical flange and photo of the Zerodur chamber with mounted metal adapter, the cuboid dimensions being 50 mm  $\times$  50 mm  $\times$  70 mm. Photo reprinted from reference [119].

We again used NOA 63 to glue the window before we mounted the flange. The low outgassing epoxy needs two days gelling at room temperature before curing for minimum 8 h at 80 °C. Although we glued NOA 63 before the epoxy and thereby exceeded the critical temperature of NOA 63, a background pressure of  $2 \times 10^{-8}$  mbar corresponding to the reference pressure was achieved after three days of bake-out at 60 °C. However, the measured leak rate of  $4 \times 10^{-10}$  mbar l/s at the window was slightly increased compared to the reference leak rate of  $1 \times 10^{-10}$  mbar l/s without sprayed helium. In contrast, the leak rate at the flange connection showed no deviation from the reference leak rate.

Two flange designs were presented, one detachable and one non-detachable but miniaturizable. With achieved background pressures in the HV/UHV range, both designs proved suitable for Zerodur-based vacuum applications. Moreover, in addition to the flange connections, the window connections appeared vacuum-tight (provided that the critical temperature of the adhesive is not exceeded). We are now turning to integrated systems, where we apply these findings to a flange-less quantum sensor demonstrator.

#### 4.2.2 Zerodur MOT chamber

Nearly all cold atom experiments start with a MOT, the design of which typically includes a vacuum chamber with optical ports for laser cooling, coils for atom trapping as well as an atomic source and pumps. We have developed a flange-less Zerodur vacuum chamber for a rubidium MOT to prove the maturity of our technology. We use passive pumps which do not require a flange connection to maintain a sufficiently low background pressure. The design of our chamber is introduced first before presenting the atomic source and passive pumps. Lastly, the procedure of sealing the chamber within a vacuum environment is discussed.

##### Chamber design

The basic shape of the chamber body is an octagon with 60 mm diameter and 40 mm height, machined from one piece of Zerodur. A photo of the chamber body is depicted in figure 4.6.



**Fig. 4.6:** Photo of the Zerodur MOT chamber body with 60 mm diameter and 40 mm height. Reprinted from reference [120].

Six windows of one inch diameter provide optical access for laser cooling in all three spatial dimensions. Four of the windows are mounted in pairs on opposite side surfaces, the remaining two on the top and bottom side. Rectangular glass inlets of size 24 mm × 17 mm are inserted in the other four side surfaces. The atomic source and passive pumps are mounted on one of the inlets each, while the remaining two provide optical access for the MOT detection. For gluing the windows and inlets we use NOA 63, based on our experience with the chambers presented above. The coils for trapping the atoms are mounted on circular recesses on the top and bottom side of the chamber body.

##### Atomic source and passive pumps

Our atomic sources are alkali metal dispensers (AMDs) containing rubidium chromate with a reducing agent. Heating the dispensers under vacuum starts a reduction reaction which causes the rubidium to evaporate. The reducing agent being a getter material, it sorbs unwanted gases produced during this reaction, thus preventing contamination of the rubidium vapor [128]. Alkali metals evaporate in the temperature range 550 °C–850 °C,

where the evaporation rate scales with temperature. To protect the Zerodur, the glass inlet and especially the adhesive from the high temperatures during activation, the dispensers are mounted on a Macor support instead of directly on the inlet. Macor is a glass ceramic that can withstand high temperatures and provides good thermal insulation.

We use three linear AMDs (SAES RB/NF/3.4/12 FT10+10) with 12 mm active length and terminals of 10 mm length at both ends for electrical connection. The terminals are shortened to the size of the inlet and mounted on the Macor support with molybdenum wire. As the chamber has no flange connection and no feedthroughs, we focus four laser diodes with an output power of approximately 4.5 W each around 450 nm through the glass inlet on the AMDs for activation.

To maintain a sufficiently low background pressure inside the flange-less chamber, we use non-evaporable getters (NEGs). Based on sorption, gas molecules react with the getter material and form stable chemical compounds [129]. However, while rare gases cannot be sorbed at all, the sorption process is reversible e.g. for  $H_2$  depending on temperature and pressure. A special type of NEGs with high porosity and large specific surface area are sintered porous getters. The porous structure allows gases to diffuse into the bulk material and thus exploiting the entire getter mass. Sintered porous getters are typically based on a mixture of powders including zirconium powder, sintered at high temperature under vacuum.

When first exposed to the atmosphere after sintering, a thin passivating oxide layer forms on the getter surface and prevents sorption. The getter is activated by heating under vacuum, whereby the passivating layer diffuses into the bulk material and leaves a clean surface. This process also involves a release of gases which leads to an increase in pressure. Although the gases can be re-pumped by the getter, it is advised to perform the initial activation under pumping to leave this to the main pump [129]. The gettering rate deteriorates over time, but can be recovered by a reactivation, i.e. another heat treatment. This process can be repeated several times to maintain a low background pressure over long periods of time.

We use four sintered porous NEGs (SAES ST172/LHI/3-7/200) of cylindrical shape with a length of 7.1 mm and a diameter of 3 mm. Like the AMDs, the getters are also mounted on a Macor support using a wire running through each NEG for electrical activation. The minimum activation temperature is 200 °C, but it is crucial to activate all four NEGs at the same time [129]. With the same laser diodes we also use to activate the AMDs, we reach temperatures of 500 °C–700 °C. A photo of the two inlets with mounted AMDs and NEGs is shown in figure 4.7.

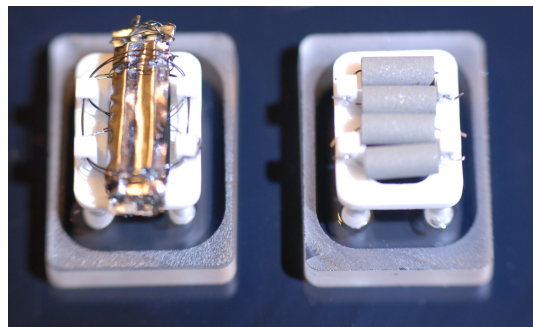


**Fig. 4.7:** Photo of the two inlets with mounted AMDs (left) and NEGs (right). The footprint of the inlets is 24 mm × 17 mm each. Reprinted from reference [120].

### Sealing procedure

The final assembly starts with gluing all inlets and all but one window. A photo of the Zerodur MOT chamber with glued side windows and mounted AMDs is shown in figure 4.8.

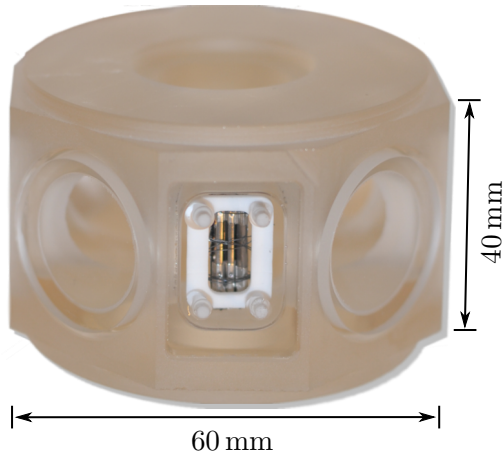


**Fig. 4.8:** Photo of the Zerodur MOT chamber with mounted AMDs. Reprinted from reference [120].

tuned to the  $D_2$  transition, we were able to check for fluorescent light in the Zerodur chamber during activation. When the fluorescent light was observed, the background pressure in the bigger chamber with connected turbomolecular pump (Pfeiffer TMH 071 P, pumping speed 331/s) showed an increase from  $4 \times 10^{-8}$  mbar to  $1 \times 10^{-4}$  mbar indicating a successful activation.

We used two ways of monitoring the activation of the getters. First, we estimated a temperature of  $600^\circ\text{C}$  based on the color of the glowing metal. Second, the background pressure increased as expected (see previous section) from  $4.6 \times 10^{-8}$  mbar to  $3 \times 10^{-4}$  mbar before falling back to  $4.6 \times 10^{-8}$  mbar. Both indicators point to a successful activation.

We have chosen the top window to be the one connected under vacuum using a dedicated setup (see reference [119]). Remotely controlled servomotors press the window onto the Zerodur chamber once a sufficiently low background pressure is reached in the bigger chamber. We use NOA 63 to seal the chamber due to the measured low leak rates of this adhesive (see previous section). However, as we do not know the outgassing behavior of the adhesive prior to curing, we seal at a background pressure of maximum  $1 \times 10^{-4}$  mbar.

To initially activate dispensers and getters under vacuum and under pumping, the Zerodur chamber must be placed in a vacuum environment, i.e. inside a bigger vacuum chamber. Due to the omission of feedthroughs in the Zerodur and the associated possibility of electrical activation, monitoring without direct access is a particular challenge here. After the activation and still inside the bigger chamber, the Zerodur chamber must be sealed remotely. The strategies for monitoring the activation and the sealing procedure are briefly discussed, for more details see reference [119].

To monitor the activation of the dispensers, we take advantage of the spectroscopic properties of rubidium. Using a laser



### Results and outlook

After allowing NOA 63 to wet the contact area of window and Zerodur, we cured the adhesive before venting the bigger chamber. In doing so, a yellowish glow of the NEGs indicated a chemical reaction with oxygen and thus an insufficient seal. Also, a blue low viscosity adhesive (Hysol Tra-Bond F112) we applied afterwards unveiled an air duct in the sealing (see figure 4.9). While for a vacuum-tight seal we would expect the blue adhesive not to enter the sealing layer, it clearly reached the chamber volume.

With the NOA 63 already cured, the chamber could not be used for another sealing test. Due to the long lead times in the production and assembly of the chamber, no further attempt to successfully seal a Zerodur vacuum chamber could be made within the scope of this thesis. However, we have identified critical points to be improved in the next iteration. First and foremost, the alignment of the window when pressed on the chamber must be self-adjusting to avoid tilting. The sealing assembly used features a piston that presses the window with a flat surface. Variations in surface flatness might cause a slight tilting of the window and the flat piston head should therefore be replaced by a (half-) sphere. Also, the outgassing behavior of NOA 63 in comparison with other adhesives should be investigated. Not least, we should better take advantage of sealing with a light-curing adhesive by checking for air ducts before curing.

Building on the experience with the flange-based chambers, we have made an attempt to set up a flange-less and compact Zerodur vacuum chamber. Designed as quantum sensor demonstrator based on a MOT, the chamber features optical ports for laser cooling and detection, mounting options for coils as well as a rubidium atomic source and passive pumps. The atomic source and passive pumps were successfully activated remotely under vacuum.

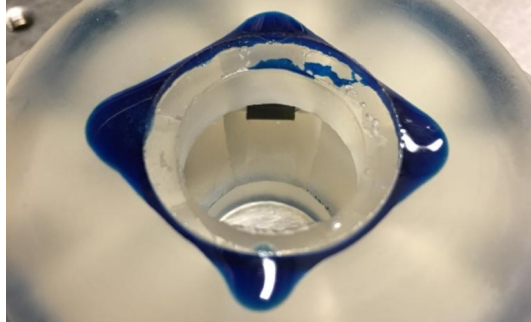


**Fig. 4.9:** Photo of the Zerodur MOT chamber's top window. The blue adhesive unveils an air duct in the sealing. Reprinted from reference [119].



# CHAPTER 5

---

## Impact

---

Since publication, the developments presented have had various impacts. The beam separator introduced in publication I will be implemented on the Zerodur-based optical modules for the BECCAL experiment on the International Space Station. Publication II has attracted attention beyond the QUANTUS consortium which resulted in a cooperation with a research group of the Physikalisch-Technische Bundesanstalt (PTB). To this end, a Zerodur-based optical module for a transportable  $\text{Al}^+/\text{Ca}^+$  quantum logic optical clock was assembled. Last but not least, the technique presented in publication III has been identified for a frequency reference demonstrator satellite mission [130, 131]. According to the proposal, two ECDLs are independently stabilized on different hyperfine transitions of the  $^{85}\text{Rb}$   $5\text{S}_{1/2} \rightarrow 5\text{D}_{5/2}$  two-photon transition at 778 nm by detecting the fluorescence light via the  $6\text{P}_{3/2}$  state at 420 nm. Our technique can help saving power and space by using only one optical setup instead of one for each laser.

The Zerodur-based optical modules for the BECCAL apparatus as well as the module for the transportable quantum logic optical clock are briefly presented in the following.

### 5.1 Zerodur-based optical modules for BECCAL

The Bose-Einstein Condensate and Cold Atom Laboratory (BECCAL) serves as a platform for a wide range of experiments based on ultra-cold or condensed clouds of potassium and rubidium atoms. The payload design and capabilities are described in detail in reference [40]. Building upon the heritage of the MAIUS missions, the laser system again incorporates fiber-coupled Zerodur-based optical modules. However, adjustments and improvements are made at both component and module level.

While at component level the optical isolators are replaced by more compact ones, the dichroic mirror and the beam separator, both introduced for MAIUS-2/-3, are retained. The dichroic mirror is also used here for the superposition of light at 767 nm and 780 nm in the same polarization state. The beam separator is retained to facilitate SWaP budget compliance.

Following the nomenclature introduced before, improvements at module level relate mainly to the “scientific modules”. To minimize the footprint of the modules, optics is mounted on both sides and light guided through holes in the baseplates. In addition, there are now only two optical bench form factors. Four modules each employ baseplates with the dimensions  $125\text{ mm} \times 120\text{ mm} \times 30\text{ mm}$  and  $125\text{ mm} \times 100\text{ mm} \times 30\text{ mm}$ . All eight modules are mounted in a rack assembly using a clamp-like support structure, a CAD rendering of which is shown in figure 5.1.

In summary, the Zerodur-based optical modules for BECCAL are the next logical step in development. We now also transfer the technological know-how to projects outside the QUANTUS collaboration, as presented below.

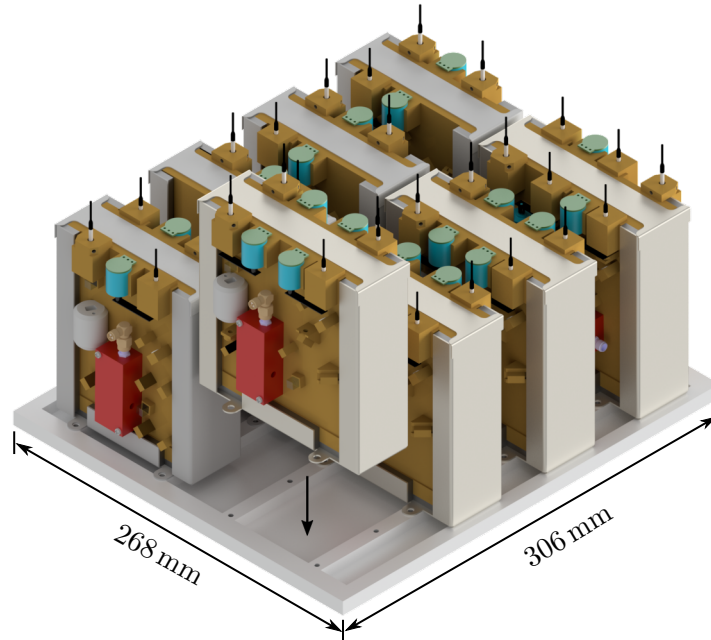


**Figure 5.1:** CAD rendering of the scientific Zerodur-based optical modules for BECCAL and their rack mounting. The baseplate dimensions of four modules each are  $125\text{ mm} \times 120\text{ mm} \times 30\text{ mm}$  and  $125\text{ mm} \times 100\text{ mm} \times 30\text{ mm}$ . Adapted from reference [40].

## 5.2 Zerodur-based optical module for an $\text{Al}^+/\text{Ca}^+$ quantum logic optical clock

In the course of releasing publication II, we have established a cooperation with a research group of PTB to assemble a Zerodur-based optical module for a transportable  $\text{Al}^+/\text{Ca}^+$  quantum logic optical clock. The module reduces space requirements and alignment time after transport, compared to conventional breadboard solutions, to the benefit of measurement time.

$^{27}\text{Al}^+$  has a 8 mHz narrow clock transition, but no suitable cooling transition (for more details, see e.g. references [132–134]). However, the clock ion can be cooled sympathetically by quantum logic spectroscopy with an ion of another species (the logic ion). The logic ion should have closed transitions for Doppler cooling and a similar mass as the clock ion to allow for fast cooling.  $^{40}\text{Ca}^+$  provides a good trade-off between mass ratio, Doppler cooling linewidth and easily addressable wavelengths [135]. The wavelengths include 422 nm for resonant excitation, 375 nm for photo ionization, 397 nm for Doppler cooling and 866 nm for re-pumping. Light at 854 nm is used to clear the upper  $^2\text{D}_{5/2}$  level for sideband cooling with light at 729 nm. A reduced level scheme of  $^{40}\text{Ca}^+$  including transition wavelengths is shown in figure 5.2.

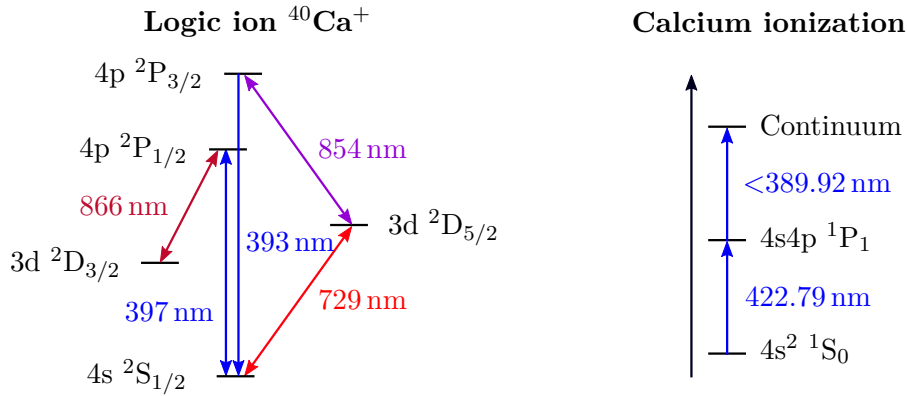


**Figure 5.2:** Reduced  $^{40}\text{Ca}^+$  level scheme, not to scale. Adapted from reference [134].

The developments in the fields of both optical atomic clocks and distant frequency comparisons have leveraged new applications in astronomy and geodesy. They are based on the idea of deriving gravitational potential differences by comparing frequencies of distant clocks, known as relativistic geodesy or chronometric leveling [136]. The method is all the more revealing the more flexibly the measurement locations can be chosen. However, leaving the laboratory environment requires transportable, i.e. compact and robust devices. Based on our laser system technology, we have assembled a Zerodur-based optical module to couple light of all required wavelengths for ionization, cooling and re-pumping of  $\text{Ca}^+$  except for  $729\text{ nm}^1$  into a large mode area (LMA) polarization maintaining (PM) photonic crystal fiber (PCF). A photo of the module with marked beam paths is shown in figure 5.3.

As can be seen in figure 5.3, the module is built on a baseplate with a footprint of  $150\text{ mm} \times 150\text{ mm}$ . Light is guided to the module via four optical PM fibers, coupled out and superimposed in free space with three (commercial) dichroic mirrors. The superimposed light is coupled into the LMA PCF, while an additional fiber coupler is provided for light at  $422\text{ nm}$  only. The ratio of light at  $422\text{ nm}$  coupled into the LMA PCF and the additional fiber can be adjusted with a unit of half-wave plate and polarizing beam splitter.

<sup>1</sup> Light at  $729\text{ nm}$  requires its own distribution for sideband cooling and clock operation and is therefore not implemented on this module.

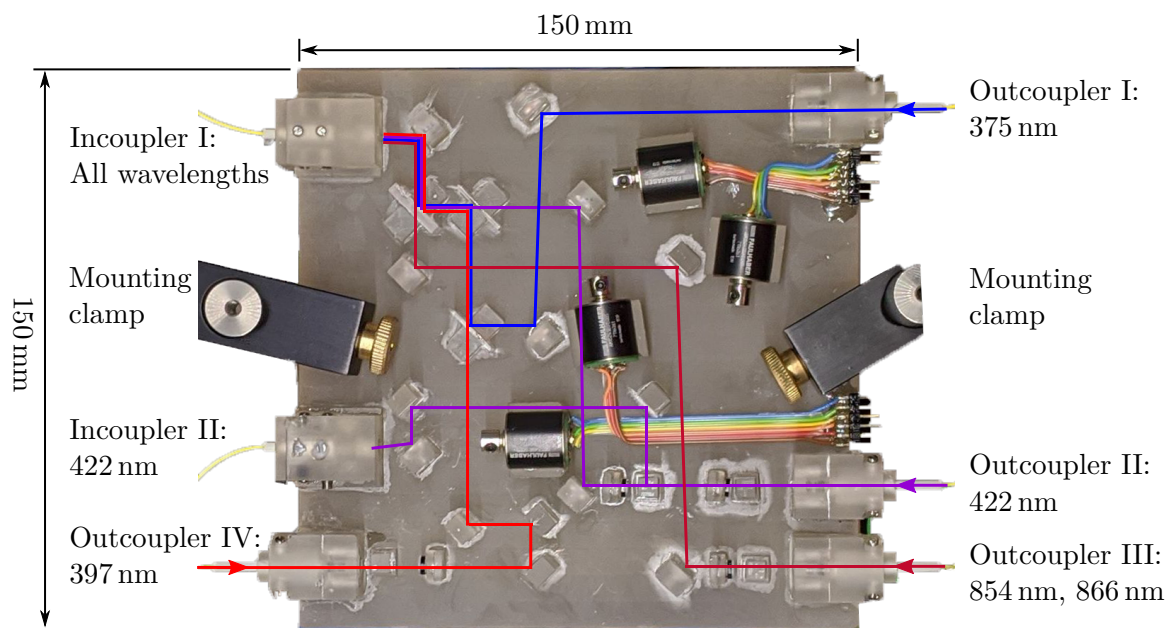


**Figure 5.3:** Photo of the Zerodur-based optical module for an  $\text{Al}^+/\text{Ca}^+$  quantum logic optical clock with marked beam paths. The baseplate dimensions are  $150\text{ mm} \times 150\text{ mm} \times 25\text{ mm}$ .

# CHAPTER 6

---

## Conclusion and outlook

---

50 years after the first laser took off into space on Apollo 15, we are on the verge of bringing a laboratory-filling experiment on two successive sounding rocket missions – MAIUS-2 and MAIUS-3. During the approximately 6 min in reduced gravity on each flight, atom interferometry with BECs of potassium and rubidium is performed sequentially and simultaneously to test the weak equivalence principle. Cooling, manipulating and imaging of the atomic clouds requires a laser system, i.e. an optical system for beam guidance and manipulation in addition to the laser light sources.

The entire payload including the laser system must withstand motor vibrations of  $< 2 g_{\text{RMS}}$ , accelerations of maximum 12.5 g and temperature variations of several degrees. The laser system itself must fit into a housing with a diameter of only 46 cm and a height of 32 cm. In addition to the actual components, it must accommodate more than 100 m optical fiber and over 50 splice connections with bulky splice protections.

To meet the requirements of mechanical and thermal stability in a small package, I presented a technology for robust and miniaturized fiber-coupled optical modules. By gluing various optical elements onto a Zerodur baseplate, modules can be assembled for a variety of applications. Although introduced elsewhere, the contributions presented in this thesis facilitated the use of the technology within the MAIUS program by further reducing the package size. This applies in particular to the beam separator, which makes it possible to separate superimposed beams of different diffraction orders directly behind AOMs, while the conventional approach of spatial separation requires a beam path of the order of at least 10 cm. The beam separator's operating principle and key figures were originally presented in publication I, the actual design and functionality of the optical modules for the MAIUS missions in publication II.

While preparations for the upcoming flights are still ongoing, important milestones within the project have already been achieved. An overview of milestones with (scheduled) dates (as of August 2020) is given in table 6.1. On 19 October 2018, the entire scientific payload passed the critical design review (CDR) after each subsystem had passed an individual one. The critical design review marks the design freeze before production, assembly and integration of the flight hardware.

**Table 6.1:** Important milestones of the missions MAIUS-2 and MAIUS-3 with (scheduled) dates.

Milestone	Date
Critical design review scientific payload	19 October 2018
Delivery laser system	17 November 2020
Flight readiness review MAIUS-2	10 August 2021
Completion flight campaign MAIUS-2	1 October 2021
Flight readiness review MAIUS-3	7 September 2022
Completion flight campaign MAIUS-3	13 October 2022

The delivery of the laser system is scheduled for 17 November 2020. The laser system is currently being integrated, i.e. all components are installed in the system, electrical connections are established and fibers spliced. With respect to the Zerodur-based optical modules, photodiodes are attached for monitoring and troubleshooting purposes. Also, mechanical shutters are integrated to block residual light with high extinction ratio.

After delivery of the laser system, the entire scientific payload is integrated and the experiment performance optimized, among other things, by adjusting the splitting ratios at the PBS on the optical modules. A subsequent series of payload operational tests is concluded by the flight readiness review for the missions MAIUS-2 and MAIUS-3 on 10 August 2021 and 7 September 2022, respectively. The payload is then carried to the launch site for the corresponding flight campaigns, which should be finished by 1 October 2021 and 13 October 2022.

The innovations developed for the MAIUS laser system are a trailblazer for future projects like BECCAL, a cold atom experiment to be operated on board the International Space Station. I also introduced a technique that is not used in MAIUS, but has been identified for a demonstrator satellite mission and that enables a further reduction of the package size in multi-species experiments. While multi-species experiments usually rely on a separate optical setup for every species and transition to generate a frequency discriminant, the presented technique permits laser frequency stabilization on multiple transitions of different atomic species with a single optical setup. The principle was originally presented in publication III.

Paving the way to highly robust and fully integrated quantum optical systems such as quantum sensor applications, I showcased procedures for building Zerodur-based vacuum systems. To this end, two vacuum chambers with different flange designs were initially set up to investigate vacuum-tight connections of optical components with Zerodur. Building on these findings, a flange-less Zerodur vacuum chamber with the footprint of a coffee cup was assembled. Designed as quantum sensor demonstrator based on a magneto-optical trap, the chamber features a rubidium atomic source and passive pumps that have been successfully activated remotely under vacuum. The next step is to seal the chamber and combine it with the laser system technology to build a fully integrated quantum optical system on a single technological basis.



As space-qualified technology is also suitable for other applications in harsh environments, we have teamed up with a research group of the Physikalisch-Technische Bundesanstalt (PTB) to develop a Zerodur-based optical module for a transportable quantum logic optical clock. By using this clock in the field and comparing the frequency with another clock, gravitational potential differences can be derived for applications such as geodesy. With the assembly being completed, the module currently undergoes extensive characterization before being integrated into the experiment. Results will be published in reference [137].

As the example of transportable optical clock demonstrates, there are many more possible applications for the technologies and techniques presented in this thesis, not least when integrating the vacuum systems – in space and beyond.



---

Publication I

---

Highly angular resolving beam separator based on total internal reflection

Moritz Mihm, Ortwin Hellmig, André Wenzlawski, Klaus Sengstock, and Patrick Windpassinger

Published in *Appl. Opt.* (July 2019), vol. 58(21): pp. 5770–5773.  
<https://doi.org/10.1364/AO.58.005770>





# Highly angular resolving beam separator based on total internal reflection

MORITZ MIHM,<sup>1,\*</sup> ORTWIN HELLMIG,<sup>2</sup> ANDRÉ WENZLAWSKI,<sup>1</sup> KLAUS SENGSTOCK,<sup>2</sup> AND PATRICK WINDPASSINGER<sup>1</sup>

<sup>1</sup>Johannes Gutenberg-Universität Mainz, Staudingerweg 7, 55128 Mainz, Germany

<sup>2</sup>Institut für Laserphysik/Zentrum für optische Quantentechnologien, Universität Hamburg, Luruper Chaussee 149, 22761 Hamburg, Germany

\*Corresponding author: mmihm@uni-mainz.de

Received 25 March 2019; revised 22 May 2019; accepted 26 June 2019; posted 27 June 2019 (Doc. ID 363153); published 19 July 2019

We present an optical element for the separation of superimposed beams that only differ in angle. The beams are angularly resolved and separated by total internal reflection at an air gap between two prisms. As a showcase application, we demonstrate the separation of superimposed beams of different diffraction orders directly behind acousto-optic modulators for an operating wavelength of 800 nm. The wavelength as well as the component size can easily be adapted to meet the requirements of a wide variety of applications. The presented optical element allows one to reduce the lengths of beam paths and thus to decrease laser system size and complexity. © 2019 Optical Society of America

<https://doi.org/10.1364/AO.58.005770>

## 1. INTRODUCTION

Obtaining high angular resolution, i.e., separating light beams, which stem from the same source but propagate under slightly different angles, is a common challenge when designing optical systems. Typically, for a given design concept, one can improve the angular resolution by adapting the beam waist or its wavelength and extended propagation distances. However, if waist and wavelength are fixed and system compactness and simplicity are a design goal, alternative approaches need to be considered.

A very common example in this context are acousto-optic modulators (AOMs). AOMs are very well established and widely used devices, e.g., for fast switching, frequency shifting, and intensity modulation of laser beams and are applied in numerous present-day experiments. Their functional principle relies on light scattering on an acoustic density wave in a crystal. In a typical application, the deflected beam, the undeflected beam, or both beams are exploited and thus need to be well separated. As the deflection angle between two diffraction orders is only in the range of 1° for an 80 MHz-AOM in the near-infrared spectrum (IR-A), a beam path of 6 cm is required to separate beams of waist 0.5 mm ( $1/e^2$  radius) by twice their waist (2.3% overlap).

For applications where compactness of the systems is crucial, like quantum gas experiments in space [1], portable optical clocks [2,3], or highly complex laser systems with many parallel optical paths like quantum computers [4], beam separation by distance is infeasible. We have therefore developed a highly angular resolving optical beam splitter (“beam separator”) for

the specific example of separating undiffracted and first diffraction order beams of an AOM whose functional principle relies entirely on the angular dependence of total internal reflection.

The wavelength dependencies of our device only stem from the wavelength dependencies of the antireflective (AR) coatings; the element can thus be produced for a wide range of wavelengths. Moreover, as the optical element only relies on standard optical elements, it can easily be produced in various sizes and be adapted to different beam diameters.

## 2. OPERATING PRINCIPLE

A schematic top view of the beam separator is depicted in Fig. 1(a), a photo in Fig. 1(b). Two right-angle prisms with opposite hypotenuses form a cube with an air gap of approximately 125  $\mu\text{m}$ . Total internal reflection can occur at the interface between the first prism with index of refraction  $n_1$  and the air gap with index of refraction  $n_2 < n_1$  at an incidence angle larger than the critical angle. The critical angle can easily be derived from Snell's law and is given by

$$\theta_c = \arcsin\left(\frac{n_2}{n_1}\right). \quad (1)$$

In AOMs, light is diffracted at a sound wave propagating in a crystal. The first order intensity becomes maximum for light incident at the Bragg angle, given by

$$\theta_B = \frac{\lambda f}{2v}, \quad (2)$$

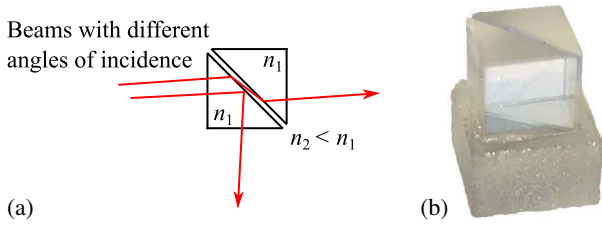


**Fig. 1.** Two right-angle prisms with index of refraction  $n_1$  form a cube with an air gap (index of refraction  $n_2 < n_1$ ) at which total internal reflection can occur. When fine-tuned to the critical angle, the beam of one diffraction order is reflected, while the other is transmitted through the beam separator. (a) Schematic top view of the beam separator, (b) beam separator on a Zerodur base.

with  $\lambda = \lambda_0/n$  being the wavelength of the light in the crystal,  $v$  the acoustic velocity, and  $f$  the radio frequency (RF). The angle between undiffracted and first diffraction order beams is twice the Bragg angle.

In order to separate the beams of different diffraction orders, the beam separator has to be tuned to the critical angle of total internal reflection so that the beam of one diffraction order is reflected while the other is refracted according to Snell's law. When entering the second prism, this beam is refracted again in the original direction of propagation and therefore transmitted through the optical element.

### 3. IMPLEMENTATION

To build a beam separator, the two prisms made of N-BK7 with 5 mm long legs (Thorlabs PS909) are glued on a Zerodur base to ensure a fixed width of the air gap. The use of a light-curing adhesive (NOA63) allows for precise alignment of the prisms prior to curing. An optical fiber (without coating) is placed between both prisms as a spacer to ensure the surfaces are parallel. All prism interfaces have an AR coating made in-house for an operating wavelength of 800 nm. This wavelength has been chosen by way of example and can easily be adapted. At this wavelength, N-BK7 has an index of refraction of 1.5108, leading to a critical angle of  $\theta_c = 41.45^\circ$ .

While the beam of one diffraction order is completely ("totally") reflected (independent of the polarization), the transmitted beam is not only refracted but also reflected according to Fresnel equations when leaving the first prism and entering the second (see Fig. 1). We have developed an AR coating with five alternating layers of magnesium fluoride ( $\text{MgF}_2$ ,  $n = 1.4$ ) and zinc sulfide ( $\text{ZnS}$ ,  $n = 2.4$ ) to reduce these unwanted reflections in the vicinity of the critical angle from over 60% to below 1%. The calculated reflectance for s-polarized light as a function of the angle of incidence at a glass-air interface ( $R_1$  in Fig. 2) with and without AR coating is depicted in Fig. 3. The reflectance at the air-glass interface ( $R_2$ ) is equally high because the refraction angle of prism one is equal to the angle of incidence of prism two while the refractive indices are inverted. Therefore, the same coating is applied to both prisms.

The width of the air gap between the two prisms is a trade-off between the influence of beam profile deformation and a potential etalon effect. Due to the large refraction angle, the

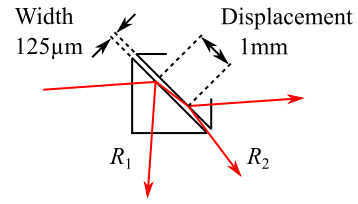


**Fig. 2.** Beam displacement and unwanted reflections  $R_1$  and  $R_2$  of the transmitted beam, which are suppressed by AR coatings.

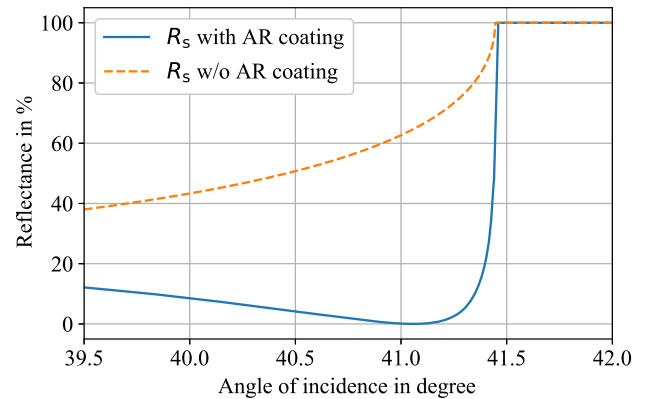


**Fig. 3.** Calculated reflectance for s-polarized light at a glass ( $n = 1.5108$ ) to air interface as a function of the angle of incidence according to Fresnel equations (" $R_s$  without AR coating" in orange) and with AR coating (blue).

beam profile is squeezed in one axis, which leads to an elliptical profile. Only for small distances between the prisms, there is no need to compensate for this aberration. On the other hand, the distance must be large enough to prevent reflections in itself and thus the occurrence of etalon effects. Since the coupling of light into an optical fiber is very sensitive to changes in the beam profile, we use the fiber coupling efficiency as a figure of merit for the influence of the beam profile squeezing. Etalon effects in turn lead to power fluctuations, so we use power stability as a figure of merit in this case. At the selected width of the air gap of 125  $\mu\text{m}$ , the beam displacement is approximately 1 mm (see Fig. 2) for a refraction angle of  $41.1^\circ$ . In this configuration, we see neither a drop in fiber coupling efficiency nor in power stability compared to beams resolved by a sufficiently long beam path.

### 4. CHARACTERIZATION

A schematic of our characterization measurement setup is depicted in Fig. 4. The light of a tunable diode laser (TOPTICA Photonics DL pro) is guided with an optical fiber to the setup. The collimated beam (waist  $\approx 400 \mu\text{m}$ ; divergence angle within the tolerable range of the beam separator; see below) passes a half-wave plate and a polarizing beam splitter for intensity adjustment and polarization cleaning. A wavelength meter (HighFinesse WS6-200) is used to monitor the wavelength in the fraction of the beam transmitted at the polarizing

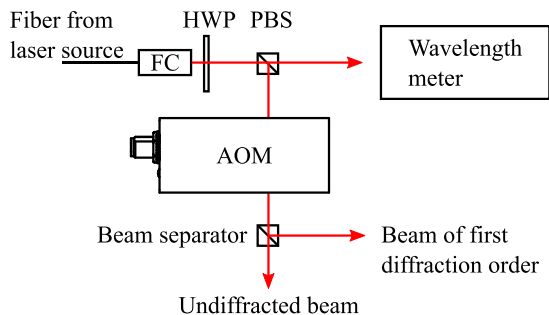


**Fig. 4.** Schematic setup for characterization measurements of the beam separator. FC, fiber collimator; HWP, half-wave plate; PBS, polarizing beam splitter; AOM, acousto-optic modulator.

beam splitter. The *s*-polarized reflected part passes the AOM (A-A MT80-A1.5-IR) with a tellurium dioxide crystal having a material-acoustic mode velocity of  $v = 4200$  m/s and an index of refraction of  $n = 2.26$  [5]. The AOM is operated at  $f = 80$  MHz; the Bragg angle at 800 nm therefore is [see Eq. (2)]  $\theta_B = 0.19^\circ$ , and the angle between undiffracted and first-order beams is  $0.86^\circ$  outside the AOM, according to Snell's law.

For characterization, the beam separator is placed on a tip, tilt, and rotation stage (Thorlabs TTR001/M) and tuned to the critical angle of total internal reflection. The transmittance spectrum is recorded with respect to a reference power measured between the AOM and the beam separator. The spectrum is shown in Fig. 5 together with the calculated spectrum, given by the squared transmittance of the AR coating for *s*-polarized light at an angle of incidence of  $41.1^\circ$ . Despite the already mentioned unwanted reflections plus the losses when entering the first and leaving the second prism, we achieve a maximum transmittance of over 90% (see inset in Fig. 5).

So far, we have only discussed beams with long Rayleigh ranges compared to the propagation distances. To reduce the switching times, however, the beam can also be focused into the AOM. As the divergence increases with smaller focus spot size, the question arises about which divergence is tolerable by the beam separator and which switching time is therefore

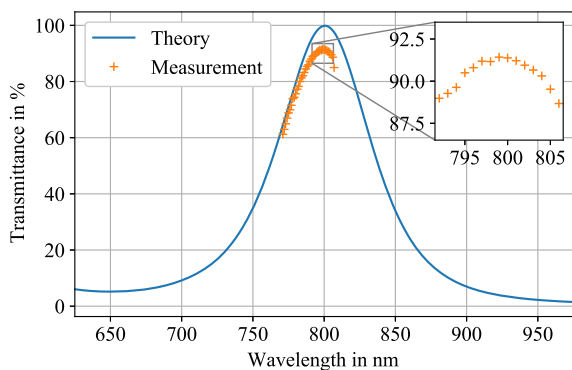


**Fig. 5.** Calculated transmittance spectrum (blue), given by the squared transmittance of the AR coating for *s*-polarized light at an angle of incidence of  $41.1^\circ$ , and measured spectrum (orange). Coating spectrum calculated using OpenFilters [6].

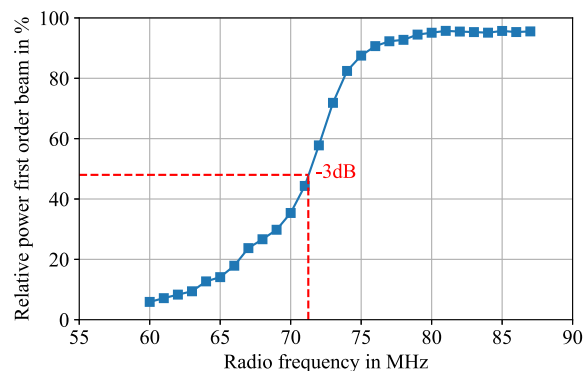


**Fig. 6.** Power of the first-order beam with respect to a reference power measured without beam separator as a function of RF. The beam separator was aligned at 80 MHz.

achievable. Based on the assumption that both the undiffracted and the first-order beam are to be used, both beams should still be separated, and no losses should occur. The angle of  $0.86^\circ$  between the two beams outside the AOM corresponds to an angle of  $0.57^\circ$  inside the beam separator ( $n = 1.5108$ ). With the undiffracted beam adjusted to the incidence angle of minimum reflectance at  $41.1^\circ$  (see Fig. 3), this results in an incidence angle of just under  $41.7^\circ$  for the beam of the first diffraction order. Thus, a divergence angle of  $0.1^\circ$  seems to be achievable without the first-order beam entering the range of transmittance, which starts just below  $41.5^\circ$ . As only the undiffracted beam is entering prism two, there is no comparable criterion for the angular tolerance at this interface. The divergence angle of  $0.1^\circ$  allows for a minimum beam waist of approximately  $150 \mu\text{m}$ , corresponding to a rise time (10%–90%) of 50 ns compared to 160 ns for a 1 mm beam. The rise time can be further reduced if only the undiffracted or the first diffraction order beam is to be used.

Since the deflection angle of the first-order beam also correlates with the RF [see Eq. (2)], the angular tolerance of the beam separator also allows one to tune the frequency of the AOM, e.g., for optical heterodyning. Assuming that the angle between the undiffracted and first-order beam outside the AOM is  $0.86^\circ$  at 80 MHz RF, the tolerable angle of  $0.1^\circ$  corresponds to 9 MHz RF. This value is in good agreement with the value obtained by measuring the relative power of the first-order beam as a function of RF if the beam separator were aligned at 80 MHz (see Fig. 6). For small RFs, the first-order beam moves into the range of transmittance, while for higher frequencies, it is always in the range of total internal reflection.

## 5. CONCLUSION

The optical element presented here separates superimposed beams that differ only by a very small angle. The beams are separated by total internal reflection at an air gap between two prisms. We successfully demonstrated the separation of undiffracted and first diffraction order beams behind AOMs as an example application. The beam separator can be placed directly behind the AOM where the two orders still fully

overlap. While the beam of one diffraction order is reflected, the other is refracted twice and therefore transmitted through the optical element. Although the double refraction is theoretically associated with high losses, in practice we achieve transmittances over 90% thanks to our AR coatings. This transmittance requires already accuracies of the coating layer thicknesses in the subnanometer range and can only be improved by an even better control of the coating process. The coating also determines the operating wavelength and can easily be adapted, as can the size of the beam separator.

The beam separator enables the development of compact laser system modules and is ideally suited for an implementation in highly stable Zerodur-based optical systems [7] for space or other field applications. We have already implemented three of the elements in the follow-up system [8] of the successful sounding rocket mission MAIUS-1, which created the first Bose–Einstein condensate in space [1,9]. Moreover, before building the flight hardware, a test bench including the beam separator has been assembled and undergone thermal tests as well as shaker tests, imposing vibrations with loads of  $8.8 g_{\text{RMS}}$ . During and after these tests, no damages or malfunctions of the beam separator have occurred. The beam separator is thus well qualified for use in compact and robust laser systems.

**Funding.** Deutsches Zentrum für Luft- und Raumfahrt (DLR) (50 WP 1433, 50 WP 1703).

**Acknowledgment.** Our work is supported by the German Space Agency DLR, with funds provided by the Federal Ministry for Economic Affairs and Energy (BMWi) under grant numbers 50 WP 1433 and 50 WP 1703.

## REFERENCES

1. D. Becker, M. D. Lachmann, S. T. Seidel, H. Ahlers, A. N. Dinkelaker, J. Grosse, O. Hellmig, H. Müntinga, V. Schkolnik, T. Wendrich, A. Wenzlawski, B. Weps, R. Corgier, T. Franz, N. Gaaloul, W. Herr, D. Lüdtkke, M. Popp, S. Amri, H. Duncker, M. Erbe, A. Kohfeldt, A. Kubelka-Lange, C. Braxmaier, E. Charron, W. Ertmer, M. Krutzik, C. Lämmerzahl, A. Peters, W. P. Schleich, K. Sengstock, R. Walsler, A. Wicht, P. Windpassinger, and E. M. Rasel, “Space-borne Bose-Einstein condensation for precision interferometry,” *Nature* **562**, 391–395 (2018).
2. A. D. Ludlow, “An optical clock to go,” *Nat. Phys.* **14**, 431–432 (2018).
3. J. Grotti, S. Koller, S. Vogt, S. Häfner, U. Sterr, C. Lisdat, H. Denker, C. Voigt, L. Timmen, A. Rolland, F. N. Baynes, H. S. Margolis, M. Zampaolo, P. Thourmany, M. Pizzocaro, B. Rauf, F. Bregolin, A. Tampellini, P. Barbieri, M. Zucco, G. A. Costanzo, C. Clivati, F. Levi, and D. Calonico, “Geodesy and metrology with a transportable optical clock,” *Nat. Phys.* **14**, 437–441 (2018).
4. H. Häffner, C. Roos, and R. Blatt, “Quantum computing with trapped ions,” *Phys. Rep.* **469**, 155–203 (2008).
5. E. H. Young and S. K. Yao, “Design considerations for acousto-optic devices,” *Proc. IEEE* **69**, 54–64 (1981).
6. S. Larouche and L. Martinu, “Openfilters: open-source software for the design, optimization, and synthesis of optical filters,” *Appl. Opt.* **47**, C219–C230 (2008).
7. H. Duncker, O. Hellmig, A. Wenzlawski, A. Grote, A. J. Rafipoor, M. Rafipoor, K. Sengstock, and P. Windpassinger, “Ultrastable, Zerodur-based optical benches for quantum gas experiments,” *Appl. Opt.* **53**, 4468–4474 (2014).
8. O. Anton, K. Döringshoff, V. Schkolnik, S. Kanthak, C. Kürbis, J. Grosse, M. Elsen, A. Wenzlawski, M. Mihm, P. Windpassinger, M. Krutzik, and A. Peters, “Design of a compact diode laser system for dual-species atom interferometry with rubidium and potassium in space,” in *Conference on Lasers and Electro-Optics Pacific Rim (CLEO-PR)* (2017), pp. 1–4.
9. V. Schkolnik, O. Hellmig, A. Wenzlawski, J. Grosse, A. Kohfeldt, K. Döringshoff, A. Wicht, P. Windpassinger, K. Sengstock, C. Braxmaier, M. Krutzik, and A. Peters, “A compact and robust diode laser system for atom interferometry on a sounding rocket,” *Appl. Phys. B* **122**, 217 (2016).



---

Publication II

---

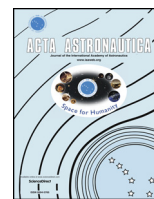
ZERODUR® based optical systems for quantum gas experiments in space

Moritz Mihm, Jean Pierre Marburger, André Wenzlawski, Ortwin Hellmig, Oliver Anton, Klaus Döringshoff, Markus Krutzik, Achim Peters, Patrick Windpassinger

Published in *Acta Astronautica* (2019), vol. 159: pp. 166–169.

<https://doi.org/10.1016/j.actaastro.2019.03.060>



ZERODUR<sup>®</sup> based optical systems for quantum gas experiments in space

Moritz Mihm<sup>a,\*</sup>, Jean Pierre Marburger<sup>a</sup>, André Wenzlawski<sup>a</sup>, Ortwin Hellmig<sup>f</sup>, Oliver Anton<sup>b</sup>, Klaus Döringshoff<sup>b</sup>, Markus Krutzik<sup>b</sup>, Achim Peters<sup>b</sup>, Patrick Windpassinger<sup>a</sup>, the MAIUS Team<sup>a,b,c,d,e,f</sup>



<sup>a</sup> Institute of Physics, Johannes Gutenberg University Mainz, Staudingerweg 7, 55128, Mainz, Germany

<sup>b</sup> Department of Physics, Humboldt University of Berlin, Newtonstraße 15, 12489, Berlin, Germany

<sup>c</sup> Institute of Quantum Optics, University of Hanover, Welfengarten 1, 30167, Hannover, Germany

<sup>d</sup> Ferdinand-Braun-Institut, Leibniz-Institut für Höchstfrequenztechnik, Gustav-Kirchhoff-Str. 4, 12489, Berlin, Germany

<sup>e</sup> The Center of Applied Space Technology and Microgravity (ZARM), University of Bremen, Am Fallturm 2, 28359, Bremen, Germany

<sup>f</sup> Institute of Laser Physics, Universität Hamburg, Luruper Chaussee 149, 22761, Hamburg, Germany

## ARTICLE INFO

## Keywords:

Microgravity  
Optical bench  
Laser system  
Integrated optics  
Glass ceramic  
ZERODUR<sup>®</sup>

## ABSTRACT

Numerous quantum technologies make use of a microgravity environment e.g. in space. Operating in this extreme environment makes high demands on the experiment and especially the laser system regarding miniaturization and power consumption as well as mechanical and thermal stability. In our systems, optical modules consisting of ZERODUR<sup>®</sup> based optical benches with free-space optics are combined with fiber components. Suitability of the technology has been demonstrated in the successful sounding rocket missions FOKUS, KALEXUS and MAIUS-1. Here, we report on our toolkit for stable optical benches including mounts, fixed and adjustable mirrors as well as polarization maintaining fiber collimators and couplers made from ZERODUR<sup>®</sup>. As an example, we present the optical modules for the scientific rocket payload of MAIUS-2, a quantum gas experiment performing dual-species atom interferometry with Bose-Einstein condensates. The modules are used on the one hand to stabilize the laser frequencies and on the other hand to distribute, overlap and switch the laser beams. This includes the overlap and joint fiber coupling of beams at 767 nm and 780 nm in the same polarization state to cool and manipulate atoms of both species simultaneously. Future projects include the development of a platform for experiments with cold atoms onboard the International Space Station. The laser system again involves ZERODUR<sup>®</sup> based optical benches in conjunction with fiber optical components. The experiment is planned as multi-user facility and currently in the design phase. The next step is to build the training, test and flight hardware.

## 1. Introduction

Numerous applications of quantum technologies benefit from a microgravity environment. The operation under rough conditions makes high demands on the experiment and especially the laser system regarding miniaturization and power consumption as well as mechanical and thermal stability. We have developed a technology for stable optical benches to overcome these difficulties. Our optical modules are based on ZERODUR<sup>®</sup>, a glass ceramic providing high mechanical and thermal stability with a thermal expansion coefficient as low as  $\pm 0.007 \cdot 10^{-6}/\text{K}$  in the range between 0 °C and 50 °C.

Here, we report on our toolkit for stable optical benches including

mounts, fixed and adjustable mirrors as well as polarization maintaining fiber collimators and couplers made from ZERODUR<sup>®</sup>. Systems based on our toolkit can fulfil all sorts of functions including laser frequency stabilization, switching and distribution of laser light. Fast switching is achieved by acousto-optic modulators (AOMs), perfect extinction by integrated mechanical shutters. As the newest tool, we have implemented an overlap and joint fiber coupling of beams at 767 nm and 780 nm in the same polarization state.

Our technology has been developed in the context of atom interferometry in space. Like numerous quantum technologies, atom interferometry benefits from a microgravity environment. On ground, the time of the matter wave in the interferometer is naturally limited by the

\* Corresponding author.

E-mail addresses: [mmihm@uni-mainz.de](mailto:mmihm@uni-mainz.de) (M. Mihm), [jemarbur@uni-mainz.de](mailto:jemarbur@uni-mainz.de) (J.P. Marburger), [awenzlaw@uni-mainz.de](mailto:awenzlaw@uni-mainz.de) (A. Wenzlawski), [ohellmig@physnet.uni-hamburg.de](mailto:ohellmig@physnet.uni-hamburg.de) (O. Hellmig), [oliver.anton@physik.hu-berlin.de](mailto:oliver.anton@physik.hu-berlin.de) (O. Anton), [klaus.doeringshoff@physik.hu-berlin.de](mailto:klaus.doeringshoff@physik.hu-berlin.de) (K. Döringshoff), [markus.krutzik@physik.hu-berlin.de](mailto:markus.krutzik@physik.hu-berlin.de) (M. Krutzik), [achim.peters@physik.hu-berlin.de](mailto:achim.peters@physik.hu-berlin.de) (A. Peters), [windpass@uni-mainz.de](mailto:windpass@uni-mainz.de) (P. Windpassinger).

<https://doi.org/10.1016/j.actaastro.2019.03.060>

Received 7 January 2019; Received in revised form 28 February 2019; Accepted 19 March 2019

Available online 22 March 2019

0094-5765/ © 2019 IAA. Published by Elsevier Ltd. All rights reserved.

free-fall time of the atoms. Longer interrogation times can be achieved on various microgravity platforms providing different quality and duration of microgravity. Common platforms include parabolic flights [1], drop towers [2,3], sounding rockets [4], the International Space Station and satellites. Suitability of our technology has been demonstrated in the successful sounding rocket missions MAIUS-1 [5], KALEXUS [6] and FOKUS [7].

As an exemplary application of our technology, we present the optical modules for the scientific rocket payload of MAIUS-2, a quantum gas experiment performing dual-species atom interferometry with Bose-Einstein condensates. Future projects include the development of the multi-user facility BECCAL, a platform for experiments with cold atoms aboard the International Space Station. From the experiences on sounding rockets, ZERODUR® based optical benches are again the technology of choice for the laser system.

After introducing the environmental and experimental requirements, we discuss our jointing techniques and toolkit for stable ZERODUR® based optical benches. Finally, the optical modules for the rocket payload of MAIUS-2 are presented.

## 2. Requirements

Quantum optical experiments usually require the possibility to manipulate, overlap, distribute and switch laser light in free space with low losses. Guiding the light to and from the modules is typically realized by optical fibers. One of the main challenges when working with fibers is the coupling of light into the fiber. Due to the small mode field diameters, positioning accuracy in the sub-micrometer range and high stability is required. We use polarization-maintaining single-mode fibers (Nufern PM780-HP). In order to minimize system losses, the non-angled end-faces have antireflective coatings.

During launch phase, our sounding rocket payloads undergo typical accelerations up to 13 g and vibrations up to 1.8 g<sub>RMS</sub>. We perform environmental tests imposing vibrations both on component and system level with loads of 5.4 g<sub>RMS</sub> and 8.1 g<sub>RMS</sub>, respectively [5].

## 3. Jointing technique

The assembly of stable optical benches requires jointing techniques providing stable bonds and allowing for precise alignment of the components. Common techniques include hydroxide-catalysis bonding and adhesive bonding.

The hydroxide-catalysis bonding technique was patented at Stanford University [8,9]. It is performed in cleanroom environments between flat polished surfaces with an overall global flatness of at least  $\lambda/10$ . Once applied, the alignment of components must be done in approximately 120 s and therefore requires an alignment jig. On the other hand, achieving full bonding strength takes four weeks at ambient temperature [10].

Adhesive bonding using e.g. the two-component epoxy Hysol EA 9313 from Henkel can be realized on matte surfaces in a laboratory environment [11]. Handling strength is achieved after 8 h (1 h with external heating), full strength after five days at ambient temperature.

Our technology takes advantage of the long processing times (several hours) of two light-curing adhesives while curing can be achieved within 1 min once radiated at the appropriate wavelengths [12]. The ZERODUR® itself is optically transparent at these wavelengths allowing to build components sequentially i.e. curing outer parts of complex components without affecting inner parts. In this way, we can assemble and integrate components before aligning and locking inner parts in place. For example, we can align the polarization and beam pointing by adjusting the fiber inside the collimator even after the housing of the fiber collimator has already been glued onto the baseplate. To glue optical elements on ZERODUR® we use Norland 63 that cures at wavelengths around 365 nm. For gluing ZERODUR® on ZERODUR® we use Fusion Flo, a nanocomposite that cures at wavelengths around 460 nm.

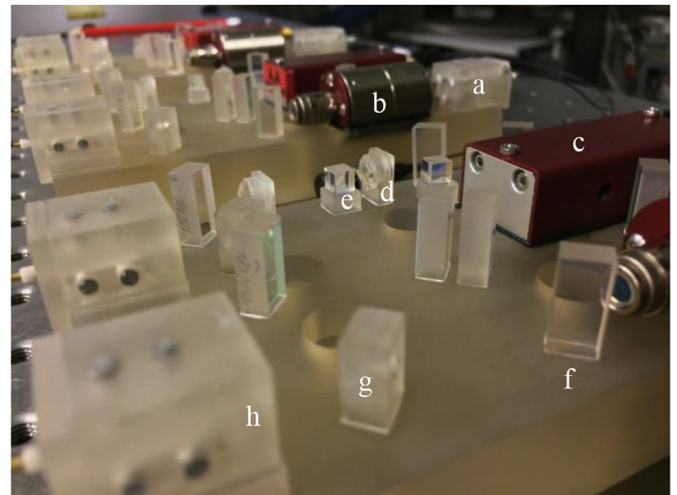


Fig. 1. Picture of a ZERODUR® based optical module showing our toolkit of components including fiber collimator (a), optical isolator (b), AOM (c), rotation mount (d), beam splitting cube (e), fixed (f) and adjustable mirror (g) and fiber coupler (h).

As third adhesive, we apply Crystalbond 509 to components designated to be realigned after being glued on the optical bench (waveplates/adjustable mirrors). Crystalbond 509 is solid at room temperature and gets viscous when heated (softening point at 71 °C). This is a reversible process allowing to conveniently realign components whenever necessary.

When gluing Non-ZERODUR® components on ZERODUR®, the mismatch in thermal expansion has to be considered. Whereas the surface area/shape of Non-ZERODUR® components changes with temperature, the coefficient of thermal expansion of ZERODUR® is negligible. This can lead to a weakened connection or even cause components to break down. The mismatch applies in particular to active components and is reinforced by the fact that ZERODUR® is a poor thermal conductor. We use the two-component epoxy Hysol Tra-Bond F112 which can endure thermal stress to mount active components like e.g. AOMs but also to lock optical isolators into position.

## 4. Toolkit

Fig. 1 gives an overview of our toolkit for stable optical benches including fiber collimators, optical isolators, AOMs, rotation mounts, beam splitting cubes, fixed and adjustable mirrors and fiber couplers.

Baseline for the assembly of an optical module is to glue all free-space components sequentially (from fiber collimator to coupler) on the ZERODUR® baseplate. Consequently, the following component can compensate for misalignments of the previous component. Exceptions are components with predefined positions such as AOMs and optical isolators as well as the very last components in the beam paths (fiber couplers). The fiber coupler is specifically designed to compensate for all misalignments on the way whereas our fiber collimator is designed to define a fix starting point for beam paths. To account for misalignments when securing the fiber ferrule inside a fiber coupler, an adjustable mirror is placed right in front.

The design of our fixed and adjustable mirrors, beam splitting cubes, rotation mounts, fiber collimators and couplers has already been introduced in Ref. [12].

To integrate free-space optical isolators (Medium Power Faraday Isolator from Electro-Optics Technology, Inc.) and AOMs (MT80-A1.5-IR from AA Sa), cut-outs are milled into the baseplates to maintain the beam height on the modules. In the case of the cylindrical isolators, the cut-outs are also cylindrical, while the cut-outs for the AOMs are flat. Both the optical isolators and the AOMs are fixed with Fusion Flo in the

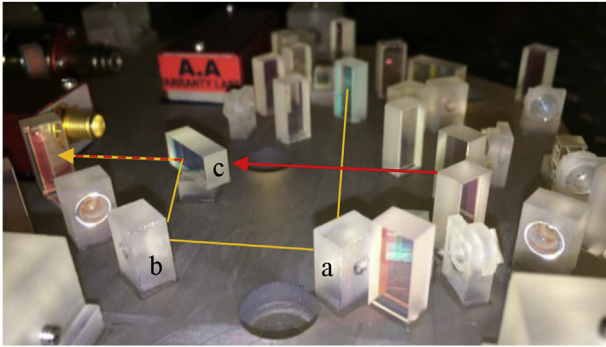


Fig. 2. Picture of a configuration to overlap beams at the wavelengths 767 nm (yellow) and 780 nm (red) including two adjustable mirrors (a, b) and a dichroic mirror (c). (For interpretation of the references to colour in this figure legend, the reader is referred to the Web version of this article.)

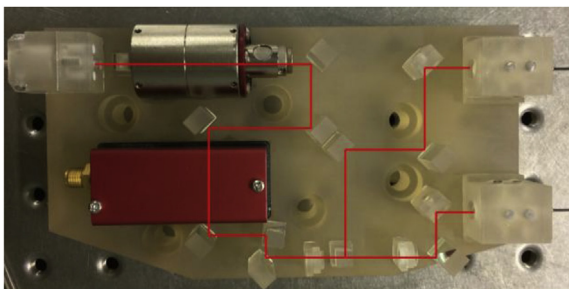


Fig. 3. Picture of one of the three ZERODUR® based single-input modules for the scientific rocket payload of MAIUS-2.

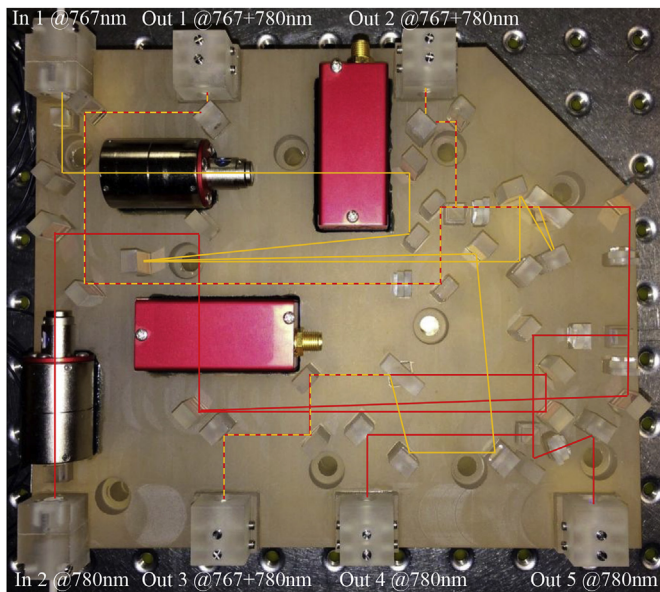


Fig. 4. Picture of one of the two ZERODUR® based double-input modules for the scientific rocket payload of MAIUS-2. The beam paths of light at the wavelengths 767 nm (yellow) and 780 nm (red) are shown. After splitting light at 780 nm off (output 4 and 5), beams are overlapped (dashed) with light at 767 nm at dichroic mirrors and jointly fiber coupled (output 1 to 3). (For interpretation of the references to colour in this figure legend, the reader is referred to the Web version of this article.)

first place before filling purposive gaps underneath with Hysol Tra-Bond F112. This adhesive can endure the thermal stress produced by the AOMs. Prior to integration, components are characterized. Results of the characterization of ten AOMs are an average first order

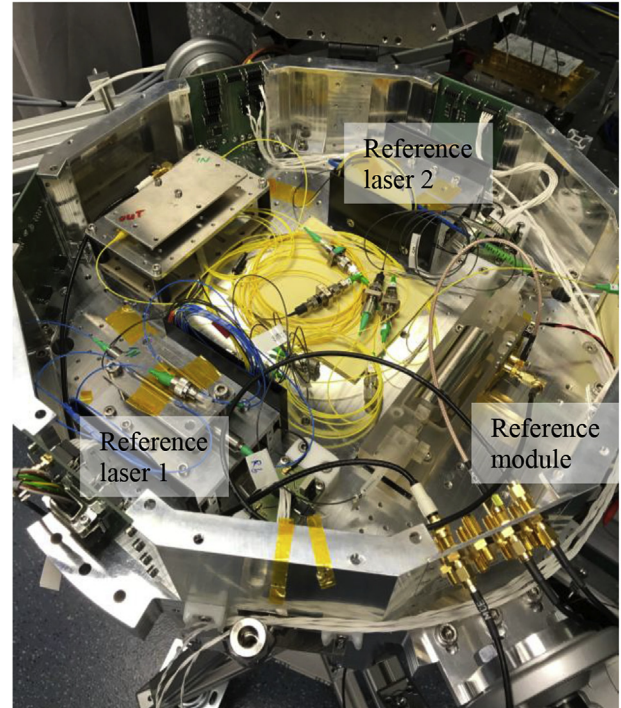


Fig. 5. Picture of one of the two ZERODUR® based frequency reference modules (right) in the laser system housing during integration test and frequency stability measurement.

diffraction efficiency at 1.3 W RF power (reference value of the manufacturer) of  $(95 \pm 1)\%$  and an average rise time (10%–90%; 0.95 mm  $1/e^2$  beam diameter) of  $(149.5 \pm 1.3)$  ns. Due to our mounting concept we have all degrees of freedom to reproduce these values on the optical modules.

On the modules for the payload of MAIUS-2 (see Sec. 5), we have implemented the overlap and joint fiber coupling of beams at 767 nm and 780 nm. Furthermore, to allow for polarization cleaning behind the optical fibers, all beams are in the same polarization state. We use dichroic mirrors to overlap the beams of different wavelengths. The coatings are applied on polished ZERODUR® substrates. When gluing the components with Fusion Flo on the baseplate, the dichroic mirror is aligned for minimal reflection of the transmitted beam at 780 nm. Losses below 3% are achieved. With the dichroic mirror locked into position, two adjustable mirrors are glued on the baseplate in the beam path of light at 767 nm to overlap beams of both wavelengths (see Fig. 2). It is crucial that these two mirrors are glued with centrally aligned beams to prevent displacements when realigning. Afterwards, beam walks are performed with the adjustable mirrors to achieve the best overlap possible. To couple the light of both wavelengths into an optical fiber, the fiber ferrule position is aligned radially with light at 780 nm. Due to the chromatic aberration of the coupling lens (Thorlabs 355230-B), the focal difference at 767 nm and 780 nm is approximately 4  $\mu$ m and the fiber end-face is aligned laterally in-between the two foci. After securing the fiber ferrule, the beam walk is repeated to maximize the coupling efficiency at 767 nm. In practice, average coupling efficiencies of 86% at both wavelengths are achieved, where we define the efficiency as the ratio of power in the optical fiber to the power in front of the fiber coupler. The chromatic shift causes a theoretical loss of efficiency of approximately 1% while we observe a loss in the range of 3%–5% in practice. The fibers have an anti-reflective coating to reduce reflections at the fiber end-faces.

## 5. Optical benches

MAIUS-2 is a quantum gas experiment performing dual-species atom interferometry with Bose-Einstein condensates on sounding rockets. The light provided by the laser system is guided via optical fibers to the physics package for 2D/3D-MOT and interferometry with Bose-Einstein condensates of potassium and rubidium atoms. MAIUS-2 is the follow-up to the MAIUS-1 experiment which successfully created the first Bose-Einstein condensate in space during a sounding rocket flight on the 23rd of January 2017 [4].

The laser system of MAIUS-2 contains in total ten diode lasers on a water-cooled platform. Five lasers at 767 nm are dedicated to transitions of potassium atoms, four lasers at 780 nm to transitions of rubidium atoms. Another laser at 1064 nm is used for a dipole trap. With the exception of the dipole laser, all lasers are fiber connected to overall seven ZERODUR® based optical modules. For each of the two species, one module provides an atomic frequency reference. Two lasers are frequency stabilized on the atomic transitions, seven science lasers are frequency stabilized w.r.t. the two reference lasers via offset beat notes. The science lasers in turn are connected to three ZERODUR® based single-input modules and two double-input modules to distribute, overlap and switch the laser beams. The layout of these modules is further discussed in the following sections.

### 5.1. Single-input module

A picture of one of the three single-input modules is shown in Fig. 3. Each of the three modules has one input and two output ports. Optical isolators are integrated behind the fiber collimators to prevent back reflections. Zeroth and first diffraction order of the AOMs are separated and the first order is split for the two output ports while the zeroth order is used for intensity monitoring. The intensity ratio between the two output ports can be adjusted using a waveplate and polarizing beam splitter cube. Two modules are dedicated to potassium and one to rubidium.

### 5.2. Double-input module

One of the two double-input modules is depicted in Fig. 4. At each of the two input ports, one laser dedicated to transitions of potassium and rubidium atoms is connected. The beam paths of light at the respective wavelengths 767 nm (yellow) and 780 nm (red) are shown. Behind both fiber collimators, optical isolators are integrated to prevent back reflections and AOMs to switch the beams. Following the beam path of light at 780 nm, light of the first diffraction order is split off (output 4 and 5) with adjustable intensity using a waveplate and polarizing beam splitter cube. Afterwards the beam is overlapped (indicated by dashed lines) with light at 767 nm at a dichroic mirror and jointly fiber coupled (output 1 and 2). The zeroth diffraction order is directly overlapped and fiber coupled with light at 767 nm (output 3).

## 6. Conclusion

We introduced our toolkit for stable optical modules consisting of ZERODUR® based optical benches with free-space optics. Providing high mechanical and thermal stability, the technology is ideally suited for laser systems in space or other field applications.

As an example of use, the layout and purpose of the optical modules for the scientific rocket payload MAIUS-2 have been presented. The modules are currently characterized and prepared for integration into the complete laser system. A picture of one of the two ZERODUR® based frequency reference modules in the laser system housing during an integration test and frequency stability measurement is shown in Fig. 5. The next steps include the completion of characterization tests, final integration and the linkage with the other experiment subsystems.

## Acknowledgements

Our work is supported by the German Space Agency DLR with funds provided by the Federal Ministry for Economic Affairs and Energy (BMWi) under grant numbers 50 WP 1433 and 50 WP 1703.

Special thanks to Klaus Sengstock from the University of Hamburg for supporting the development of the ZERODUR® Technology.

## References

- [1] B. Barrett, L. Antoni-Micollier, L. Chichet, B. Battelier, T. Lévêque, A. Landragin, P. Bouyer, Dual matter-wave inertial sensors in weightlessness, *Nat. Commun.* 7 (2016).
- [2] T. van Zoest, N. Gaaloul, Y. Singh, H. Ahlers, W. Herr, S.T. Seidel, W. Ertmer, E. Rasel, M. Eckart, E. Kajari, S. Arnold, G. Nandi, W.P. Schleich, R. Walser, A. Vogel, K. Sengstock, K. Bongs, W. Lewoczko-Adamczyk, M. Schiemangk, T. Schuldt, A. Peters, T. Könemann, H. Müntinga, C. Lämmerzahl, H. Dittus, T. Steinmetz, T.W. Hänsch, J. Reichel, Bose-Einstein condensation in microgravity, *Science* 328 (2010) 1540–1543.
- [3] H. Müntinga, H. Ahlers, M. Krutzik, A. Wenzlawski, S. Arnold, D. Becker, K. Bongs, H. Dittus, H. Duncker, N. Gaaloul, C. Gherasim, E. Giese, C. Grzeschik, T.W. Hänsch, O. Hellmig, W. Herr, S. Herrmann, E. Kajari, S. Kleinert, C. Lämmerzahl, W. Lewoczko-Adamczyk, J. Malcolm, N. Meyer, R. Nolte, A. Peters, M. Popp, J. Reichel, A. Roura, J. Rudolph, M. Schiemangk, M. Schneider, S.T. Seidel, K. Sengstock, V. Tamma, T. Valenzuela, A. Vogel, R. Walser, T. Wendrich, P. Windpassinger, W. Zeller, T. van Zoest, W. Ertmer, W.P. Schleich, E.M. Rasel, Interferometry with Bose-Einstein condensates in microgravity, *Phys. Rev. Lett.* 110 (2013).
- [4] M.D. Lachmann, H. Ahlers, D. Becker, S.T. Seidel, T. Wendrich, E.M. Rasel, W. Ertmer, Creating the first Bose-Einstein condensate in space, *Proc. SPIE* 10549 (2018).
- [5] V. Schkolnik, O. Hellmig, A. Wenzlawski, J. Grosse, A. Kohfeldt, K. Döringshoff, A. Wicht, P. Windpassinger, K. Sengstock, C. Braxmaier, M. Krutzik, A. Peters, A compact and robust diode laser system for atom interferometry on a sounding rocket, *Appl. Phys. B* 122 (2016) 217.
- [6] A.N. Dinkelaker, M. Schiemangk, V. Schkolnik, A. Kenyon, K. Lampmann, A. Wenzlawski, P. Windpassinger, O. Hellmig, T. Wendrich, E.M. Rasel, M. Giunta, C. Deutsch, C. Kürbis, R. Smol, A. Wicht, M. Krutzik, A. Peters, Autonomous frequency stabilization of two extended-cavity diode lasers at the potassium wavelength on a sounding rocket, *Appl. Opt.* 56 (2017) 1388–1396.
- [7] M. Lezius, T. Wilken, C. Deutsch, M. Giunta, O. Mandel, A. Thaller, V. Schkolnik, M. Schiemangk, A. Dinkelaker, A. Kohfeldt, A. Wicht, M. Krutzik, A. Peters, O. Hellmig, H. Duncker, K. Sengstock, P. Windpassinger, K. Lampmann, T. Hülsing, T.W. Hänsch, R. Holzwarth, Space-borne frequency comb metrology, *Optica* 3 (2016) 1381–1387.
- [8] D.-H. Gwo, Ultra precision and reliable bonding method, US Patent 6 (2001) 284 085 B1.
- [9] D.-H. Gwo, Hydroxide-catalyzed bonding, US Patent 6 (2003) 548 176 B1.
- [10] S. Ressel, M. Gohlke, D. Rauen, T. Schuldt, W. Kronast, U. Mescheder, U. Johann, D. Weise, C. Braxmaier, Ultrastable assembly and integration technology for ground- and space-based optical systems, *Appl. Opt.* 49 (2010) 4296–4303.
- [11] M. Gohlke, T. Schuldt, K. Döringshoff, A. Peters, U. Johann, D. Weise, C. Braxmaier, Adhesive bonding for optical metrology systems in space applications, *J. Phys. Conf. Ser.* 610 (2015).
- [12] H. Duncker, O. Hellmig, A. Wenzlawski, A. Grote, A.J. Rafipoor, M. Rafipoor, K. Sengstock, P. Windpassinger, Ultrastable, Zerodur-based optical benches for quantum gas experiments, *Appl. Opt.* 53 (2014) 4468–4474.

---

Publication III

---

Simultaneous modulation transfer spectroscopy on transitions of multiple atomic species for compact laser frequency reference modules

Moritz Mihm, Kai Lampmann, André Wenzlawski, and Patrick Windpassinger

Published in Review of Scientific Instruments (2018), vol. 89(9): p. 096101.

<https://doi.org/10.1063/1.5041782>





## Note: Simultaneous modulation transfer spectroscopy on transitions of multiple atomic species for compact laser frequency reference modules

Moritz Mihm,<sup>a)</sup> Kai Lampmann, André Wenzlawski, and Patrick Windpassinger  
*Johannes Gutenberg-Universität Mainz, Staudingerweg 7, 55128 Mainz, Germany*

(Received 26 May 2018; accepted 17 August 2018; published online 4 September 2018)

We present a technique for simultaneous laser frequency stabilization on transitions of multiple atomic species with a single optical setup. The method is based on modulation transfer spectroscopy, and the signals are separated by modulating at different frequencies and electronically filtered. As a proof of concept, we demonstrate simultaneous spectroscopy of the potassium D<sub>1</sub>, D<sub>2</sub> and rubidium D<sub>2</sub> transitions. The technique can be extended in principle to other atomic species given the availability of optics and cells and allows the development of versatile and compact frequency reference modules. *Published by AIP Publishing.* <https://doi.org/10.1063/1.5041782>

Lasers, referenced to a well defined frequency like that of an atomic transition or an ultra-stable optical resonator, are key elements in a variety of quantum technology applications. For instance, atom interferometers,<sup>1</sup> optical clocks,<sup>2</sup> or ion based quantum computers<sup>3</sup> require a number of frequency stabilized lasers, e.g., for laser cooling and trapping or state interrogation. While techniques for stabilizing lasers to atomic vapor samples are in general well established<sup>4,5</sup> and used in atomic physics labs around the world, the field application and further exploitation of aforementioned quantum technologies require miniaturized, compact, and robust technical realizations. One key aspect in this context is, e.g., the reduction of complexity to reduce the probability of failure and the reduction of components to decrease the system size and to limit costs.

One main issue in connection with the system size, cost, and complexity is that especially in the case of multi-species experiments, several optical spectroscopy setups which require independent alignment are run in parallel, i.e., individual setups for every atomic species and every atomic transition frequency are usually implemented. To counter this approach, we have as a proof of concept implemented simultaneous dual species (potassium, rubidium), multi-transition line (D<sub>1</sub>, D<sub>2</sub>), and single beam modulation transfer spectroscopy in a single dual species atomic vapor cell for three separate lasers. By multi-frequency modulation/demodulation in a Pound-Drever-Hall type<sup>4</sup> setup for each laser, we isolate the spectroscopy signals of the different sources electronically after detection on a single photodiode and generate the individual laser's error signal. The number of involved optical components is thereby reduced significantly compared to three stand-alone setups. This approach can easily be extended to more lasers and more atomic species according to the needs of the respective application.

To generate an error signal, we employ modulation transfer spectroscopy; the overall approach would however work just as well with standard frequency modulation spectroscopy.

Modulation transfer spectroscopy has been discussed individually for potassium and rubidium.<sup>6–9</sup> In order to excite the different optical transitions simultaneously, three lasers at wavelengths of 770.1 nm (<sup>39</sup>K D<sub>1</sub>), 766.7 nm (<sup>39</sup>K D<sub>2</sub>), and 780.2 nm (<sup>85,87</sup>Rb D<sub>2</sub>) are required. To overlap the optical paths and to induce the required phase modulation of the laser light, we use a fiber-based system. This also keeps the experiment clear and compact. A general schematic of our setup is depicted in Fig. 1.

The light of the three lasers [two home-built distributed feedback (DFB) lasers with diodes by eagleyard Photonics and one TOPTICA Photonics DL pro] is initially coupled into polarization maintaining fibers. Separation of pump and probe beams is achieved by 2 × 2 fiber splitters (FS) (Evanescence Optics 954P). One output port of each of the three splitters is directly connected to another splitter (4 × 4) for combination of all probe light. Each of the other ports is connected to a fiber electro-optic phase modulator [electro-optic modulator (EOM); Photline NIR-MPX800] for frequency sideband generation. The modulated beams are overlapped with another splitter (4 × 2) to generate the combined pump light. With this arrangement, the power ratios between pump and probe ex fibers are equal, apart from the individual losses of the EOMs. However, the power ratios can be optimized with conventional free space optics.

To separate the photodetector signals of the three lasers, the EOMs are driven at modulation frequencies of 4.5 MHz, 11.5 MHz, and 16 MHz. This takes advantage of standard Mini-Circuits bandpass filter windows between ≈7 MHz and ≈15 MHz, and the frequencies are chosen such that they are no multiples of each other. The frequencies are generated by three dual-channel direct digital synthesis (DDS) based frequency generators (Rigol DG1022) which allow us to adjust the phase between the local oscillator (LO) and the spectroscopy signal from the radio-frequency (RF) photodiode. The collimated beams for the pump and probe are guided through a quartz spectroscopy cell with conventional free space optics in a counter-propagating fashion. The vapor cell (Sacher Lasertechnik VC-K-09-50-Q) is intended for potassium spectroscopy but also contains atomic

<sup>a)</sup>mmihm@uni-mainz.de

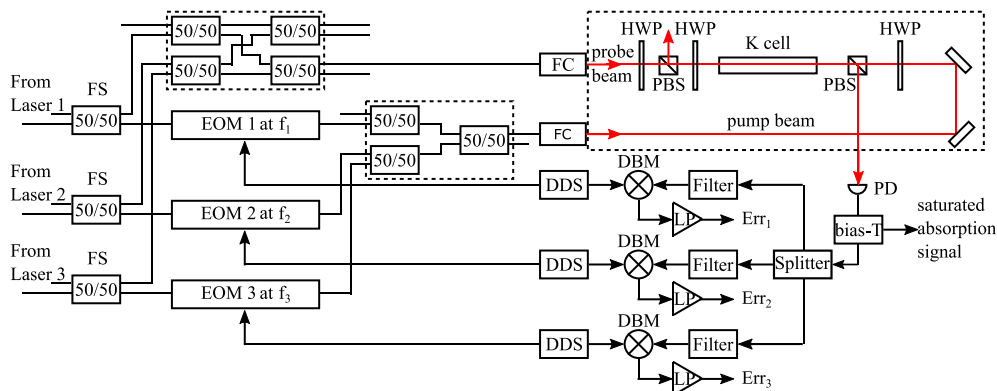


FIG. 1. Schematic setup for simultaneous modulation transfer spectroscopy of the potassium  $D_1$ ,  $D_2$  and rubidium  $D_2$  transitions. DBM: double-balanced mixer; DDS: direct digital synthesis; EOM: electro-optic modulator; FC: fiber collimator; FS: fiber splitter; 50/50: splitting ratio; HWP: half-wave plate; LP: low-pass filter; PBS: polarizing beam splitter; PD: photodiode.

rubidium. A home-built heating around the cell is used to increase the vapor pressure and hereby the signal strength. The cell is heated to temperatures around  $65^\circ\text{C}$  at the windows.

The probe beam is detected on a silicon photodiode with 150 MHz bandwidth (Thorlabs PDA10A-EC). The low- and high-frequency components of the photodiode signal are separated using a bias-T (Mini-Circuits ZFBT-6GW+). The low-frequency component represents the saturated absorption spectrum and is directly monitored. The high-frequency component is split using a three way power splitter (Mini-Circuits ZFSC-3-1W-S+) and electronically separated by low, high, and bandpass filters (Mini-Circuits BLP-5+, SHP-20+, SBP-10.7+) according to the modulation frequencies. The signal of each channel is amplified (Mini-Circuits ZFL-500+), mixed down (Mini-Circuits ZFM-3-S+) with the corresponding local oscillator, and filtered using a low pass filter with cutoff frequency 1.9 MHz (Mini-Circuits SLP-1.9+).

To show the capabilities of the setup, we frequency scan the three lasers simultaneously across the atomic transitions in question. When we scan with  $\approx 470\text{ MHz/ms}$  ( $K D_1$ ),  $\approx 1.7\text{ GHz/ms}$  ( $K D_2$ ), and  $\approx 1.1\text{ GHz/ms}$  ( $Rb D_2$ ) in an appropriate range, we observe the saturated absorption spectrum, as displayed in Fig. 2(a). As indicated in the plot, the spectrum is an overlap of three individual saturated absorption spectra.

In our setup, the relative pump and probe powers of the different lasers' ex fiber are fixed due to the chosen fiber splitter ratios but can be optimized individually, e.g., by choosing appropriate splitting ratios of the first fiber splitter. In our setup, the power ratios are adjusted with conventional free space optics for all lasers simultaneously. These powers are in general a trade-off between the power broadening and the signal-to-noise ratio (SNR) of the associated error signals. When maximizing the probe power to increase the SNR, we achieve pump and probe powers of approximately  $0.5\text{ mW}/1\text{ mW}$  for  $KD_1$  and  $1\text{ mW}/2\text{ mW}$  for  $KD_2$  and  $Rb D_2$  with beam diameters of 1.2 mm. For the chosen trade-off in Fig. 2, the  $D_1$  and  $D_2$  transitions for the most abundant naturally occurring isotope of potassium ( $^{39}\text{K}$ ) can easily be identified in the saturated absorption spectrum. For the  $D_2$  transition of rubidium, we set the scan range such that only the  $F = 2 \rightarrow F'$

of  $^{87}\text{Rb}$  and  $F = 3 \rightarrow F'$  of  $^{85}\text{Rb}$  set of transitions are displayed to avoid confusion. We use the notation  $F = x \rightarrow F'$  for the set of transitions from state  $x$  in the manifold of excited states.

With optimized phases of the respective local oscillators at the mixers in the high-frequency components of the

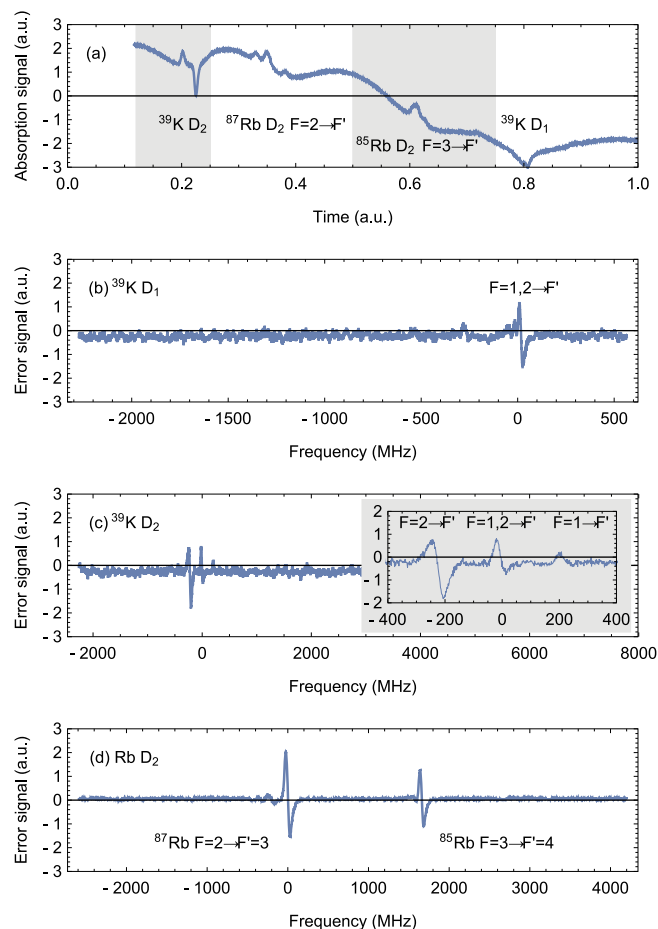


FIG. 2. Saturated absorption spectrum and associated error signals of the potassium  $D_1$ ,  $D_2$  and rubidium  $D_2$  transitions. Please note that all spectra were acquired simultaneously, and for the sake of clearness, the chosen pump and probe powers are a trade-off between power broadening of the absorption spectrum and signal-to-noise ratio (SNR) of the error signals.

photodetector signal, we obtain the desired individual error signal for each of the three lasers separately, as shown in Figs. 2(b)–2(d). The error signals' x-axes are frequency calibrated with the respective absorption spectrum. The main peak in the error signal of potassium D<sub>1</sub> is the crossover transition  $F = 1, 2 \rightarrow F'$ . As part of the calibration, this transition is used as zero-frequency reference. The error signal of potassium D<sub>2</sub> shows three peaks which can be identified as the set of ground state crossover transitions  $F = 1, 2 \rightarrow F'$  (at zero) as well as the set of transitions  $F = 2 \rightarrow F'$  (left peak) and  $F = 1 \rightarrow F'$  (right peak). The two peaks in the rubidium error signal stem from the closed transition  $F = 2 \rightarrow F' = 3$  of <sup>87</sup>Rb (left peak at zero) and the closed transition  $F = 3 \rightarrow F' = 4$  of <sup>85</sup>Rb (right peak). These signals can now be used for frequency stabilization with standard servo amplifiers.

By temporarily blocking the light from two lasers at a time, we can directly compare the error signals of single and multi-species spectroscopy for each species. Figure of merit is the SNR which is a measure for the signal quality with respect to the noise floor. Taking the peak-to-peak amplitude of the largest signal divided by the standard deviation of the noise floor as SNR, we achieve the values summarized in Table I. The values of single and multi-species spectroscopy are in the same order of magnitude. While the maximum SNR for both potassium transitions is slightly better for single species operation due to marginal cross talk, the inverted maximum SNR of the rubidium signal stems from an electronic artifact.

We successfully demonstrated a technique for simultaneous modulation transfer spectroscopy of multiple atomic species. Isolating the individual signals by modulating at different frequencies and electronic filtering, we were able to generate three error signals at the potassium D<sub>1</sub>, D<sub>2</sub> and rubidium D<sub>2</sub> transitions. The obtained signals are comparable to former frequency reference modules<sup>10–12</sup> used for different space missions. Our concept is especially applicable in dual species experiments using potassium and rubidium atoms,<sup>13,14</sup> taking new hybrid cooling schemes<sup>15–17</sup> into account by including the potassium D<sub>1</sub> transition. Our technique can easily be extended to other atomic species.

TABLE I. Error signal signal-to-noise ratios (SNR) of single and multi-species spectroscopy for each species.

SNR	K D <sub>1</sub>	K D <sub>2</sub>	Rb D <sub>2</sub>
Single species spectroscopy	33	69	109
Multi-species spectroscopy	28	59	121

At the same time, our technique only requires a single optical setup saving optical components and weight and reducing complexity. This allows the development of compact frequency reference modules for experiments with multiple atomic species. The approach is, for instance, ideally suited for implementation in highly stable ZERODUR<sup>®</sup> based optical benches<sup>18</sup> for space or other field applications.

Our work is supported by the German Space Agency DLR with funds provided by the Federal Ministry for Economic Affairs and Energy (BMWi) under Grant Nos. 50 WP 1433 and 50 WP 1703.

- <sup>1</sup>M. Kasevich and S. Chu, *Phys. Rev. Lett.* **67**, 181 (1991).
- <sup>2</sup>A. D. Ludlow, M. M. Boyd, J. Ye, E. Peik, and P. O. Schmidt, *Rev. Mod. Phys.* **87**, 637 (2015).
- <sup>3</sup>H. Häffner, C. Roos, and R. Blatt, *Phys. Rep.* **469**, 155 (2008).
- <sup>4</sup>R. W. P. Drever, J. L. Hall, F. V. Kowalski, J. Hough, G. M. Ford, A. J. Munley, and H. Ward, *Appl. Phys. B: Photophys. Laser Chem.* **31**, 97 (1983).
- <sup>5</sup>G. C. Bjorklund, M. D. Levenson, W. Lenth, and C. Ortiz, *Appl. Phys. B: Photophys. Laser Chem.* **32**, 145 (1983).
- <sup>6</sup>L. Mudarikwa, K. Pahwa, and J. Goldwin, *J. Phys. B: At., Mol. Opt. Phys.* **45**, 065002 (2012).
- <sup>7</sup>H.-R. Noh, S. E. Park, L. Z. Li, J.-D. Park, and C.-H. Cho, *Opt. Express* **19**, 23444 (2011).
- <sup>8</sup>J. Zhang, D. Wei, C. Xie, and K. Peng, *Opt. Express* **11**, 1338 (2003).
- <sup>9</sup>D. J. McCarron, S. A. King, and S. L. Cornish, *Meas. Sci. Technol.* **19**, 105601 (2008).
- <sup>10</sup>M. Lezius, T. Wilken, C. Deutsch, M. Giunta, O. Mandel, A. Thaller, V. Schkolnik, M. Schiemangk, A. Dinkelaker, A. Kohfeldt, A. Wicht, M. Krutzik, A. Peters, O. Hellmig, H. Duncker, K. Sengstock, P. Windpassinger, K. Lampmann, T. Hülsing, T. W. Hänsch, and R. Holzwarth, *Optica* **3**, 1381 (2016).
- <sup>11</sup>A. N. Dinkelaker, M. Schiemangk, V. Schkolnik, A. Kenyon, K. Lampmann, A. Wenzlawski, P. Windpassinger, O. Hellmig, T. Wendrich, E. M. Rasel, M. Giunta, C. Deutsch, C. Kürbis, R. Smol, A. Wicht, M. Krutzik, and A. Peters, *Appl. Opt.* **56**, 1388 (2017).
- <sup>12</sup>V. Schkolnik, O. Hellmig, A. Wenzlawski, J. Grosse, A. Kohfeldt, K. Döringshoff, A. Wicht, P. Windpassinger, K. Sengstock, C. Braxmaier, M. Krutzik, and A. Peters, *Appl. Phys. B* **122**, 217 (2016).
- <sup>13</sup>S. Kulas, C. Vogt, A. Resch, J. Hartwig, S. Ganske, J. Matthias, D. Schlipfert, T. Wendrich, W. Ertmer, E. Maria Rasel, M. Damjanic, P. Weßels, A. Kohfeldt, E. Luvsandamin, M. Schiemangk, C. Grzeschik, M. Krutzik, A. Wicht, A. Peters, S. Herrmann, and C. Lämmerzahl, *Microgravity Sci. Technol.* **29**, 37 (2017).
- <sup>14</sup>V. Ménot, R. Geiger, G. Stern, N. Zahzam, B. Battelier, A. Bresson, A. Landragin, and P. Bouyer, *Opt. Lett.* **36**, 4128 (2011).
- <sup>15</sup>D. Nath, R. K. Easwaran, G. Rajalakshmi, and C. S. Unnikrishnan, *Phys. Rev. A* **88**, 053407 (2013).
- <sup>16</sup>G. Salomon, L. Fouché, P. Wang, A. Aspect, P. Bouyer, and T. Bourdel, *Europhys. Lett.* **104**, 63002 (2013).
- <sup>17</sup>H. Z. Chen, X. C. Yao, Y. P. Wu, X. P. Liu, X. Q. Wang, Y. X. Wang, Y. A. Chen, and J. W. Pan, *Phys. Rev. A* **94**, 033408 (2016).
- <sup>18</sup>H. Duncker, O. Hellmig, A. Wenzlawski, A. Grote, A. J. Rafipoor, M. Rafipoor, K. Sengstock, and P. Windpassinger, *Appl. Opt.* **53**, 4468 (2014).



---

## Bibliography

---

1. Smullin, L. D. and G. Fiocco: ‘Optical Echoes from the Moon’. *Nature* (1962), vol. 194(4835): p. 1267. DOI: 10.1038/1941267a0 (cit. on p. 1).
2. Maiman, T. H.: ‘Stimulated Optical Radiation in Ruby’. *Nature* (1960), vol. 187(4736): pp. 493–494. DOI: 10.1038/187493a0 (cit. on p. 1).
3. Yu, A. W. et al.: ‘Overview of space qualified solid state lasers development at NASA Goddard Space Flight Center’. *Solid State Lasers XVIII: Technology and Devices*. Ed. by Clarkson, W. A., N. Hodgson, and R. K. Shori. Vol. 7193. International Society for Optics and Photonics. SPIE, 2009: pp. 24–30. DOI: 10.1117/12.814954 (cit. on p. 1).
4. Guilhot, D. and P. Ribes-Pleguezuelo: ‘Laser Technology in Photonic Applications for Space’. *Instruments* (2019), vol. 3(3). DOI: 10.3390/instruments3030050 (cit. on p. 1).
5. Aguilera, D. N. et al.: ‘STE-QUEST—test of the universality of free fall using cold atom interferometry’. *Classical and Quantum Gravity* (May 2014), vol. 31(11): p. 115010. DOI: 10.1088/0264-9381/31/11/115010 (cit. on p. 1).
6. Loriani, S. et al.: ‘Atomic source selection in space-borne gravitational wave detection’. *New Journal of Physics* (June 2019), vol. 21(6): p. 063030. DOI: 10.1088/1367-2630/ab22d0 (cit. on p. 1).
7. Carraz, O., C. Siemes, L. Massotti, R. Haagmans, and P. Silvestrin: ‘A Spaceborne Gravity Gradiometer Concept Based on Cold Atom Interferometers for Measuring Earth’s Gravity Field’. *Microgravity Science and Technology* (2014), vol. 26(3): pp. 139–145. DOI: 10.1007/s12217-014-9385-x (cit. on p. 1).
8. Duncker, H.: ‘Ultrastable Laser Technologies and Atom-Light Interactions in Hollow Fibers’. Dissertation. University of Hamburg, 2013 (cit. on pp. 1, 25, 28).
9. Duncker, H. et al.: ‘Ultrastable, Zerodur-based optical benches for quantum gas experiments’. *Appl. Opt.* (July 2014), vol. 53(20): pp. 4468–4474. DOI: 10.1364/AO.53.004468 (cit. on pp. 1, 25).
10. Eötvös, R. v., D. Pekár, and E. Fekete: ‘Beiträge zum Gesetze der Proportionalität von Trägheit und Gravität’. *Annalen der Physik* (1922), vol. 373(9): pp. 11–66. DOI: 10.1002/andp.19223730903 (cit. on p. 2).
11. Haslett, J. W.: ‘Phase Waves of Louis deBroglie’. *American Journal of Physics* (1972), vol. 40(9). Translation of the first chapter of Louis de Broglie’s dissertation ‘Recherches sur la théorie des quanta’, Univ. of Paris (1924).: pp. 1315–1320. DOI: 10.1119/1.1986821 (cit. on p. 2).

12. Linskens, A. F., I. Holleman, N. Dam, and J. Reuss: ‘Two-photon Rabi oscillations’. *Phys. Rev. A* (6 Dec. 1996), vol. 54: pp. 4854–4862. DOI: 10.1103/PhysRevA.54.4854 (cit. on p. 2).
13. Kasevich, M. and S. Chu: ‘Atomic interferometry using stimulated Raman transitions’. *Phys. Rev. Lett.* (2 July 1991), vol. 67: pp. 181–184. DOI: 10.1103/PhysRevLett.67.181 (cit. on p. 3).
14. Schmidt, M. et al.: ‘A mobile high-precision absolute gravimeter based on atom interferometry’. *Gyroscopy and Navigation* (2011), vol. 2(3): p. 170. DOI: 10.1134/S2075108711030102 (cit. on p. 3).
15. Bidel, Y. et al.: ‘Absolute marine gravimetry with matter-wave interferometry’. *Nature Communications* (2018), vol. 9(1): p. 627. DOI: 10.1038/s41467-018-03040-2 (cit. on p. 3).
16. Bidel, Y. et al.: ‘Absolute airborne gravimetry with a cold atom sensor’. *Journal of Geodesy* (2020), vol. 94(2): p. 20. DOI: 10.1007/s00190-020-01350-2 (cit. on p. 3).
17. Bongs, K. et al.: ‘Taking atom interferometric quantum sensors from the laboratory to real-world applications’. *Nature Reviews Physics* (2019), vol. 1(12): pp. 731–739. DOI: 10.1038/s42254-019-0117-4 (cit. on pp. 3, 8).
18. Rosi, G. et al.: ‘Quantum test of the equivalence principle for atoms in coherent superposition of internal energy states’. *Nature Communications* (June 2017), vol. 8: p. 15529 (cit. on p. 4).
19. Schlippert, D. et al.: ‘Quantum Test of the Universality of Free Fall’. *Phys. Rev. Lett.* (20 May 2014), vol. 112: p. 203002. DOI: 10.1103/PhysRevLett.112.203002 (cit. on p. 4).
20. Tarallo, M. G. et al.: ‘Test of Einstein Equivalence Principle for 0-Spin and Half-Integer-Spin Atoms: Search for Spin-Gravity Coupling Effects’. *Phys. Rev. Lett.* (2 July 2014), vol. 113: p. 023005. DOI: 10.1103/PhysRevLett.113.023005 (cit. on p. 4).
21. Williams, J., S.-w. Chiow, N. Yu, and H. Müller: ‘Quantum test of the equivalence principle and space-time aboard the International Space Station’. *New Journal of Physics* (Feb. 2016), vol. 18(2): p. 025018. DOI: 10.1088/1367-2630/18/2/025018 (cit. on p. 4).
22. Battelier, B. et al.: *Exploring the Foundations of the Universe with Space Tests of the Equivalence Principle*. 2019. arXiv: 1908.11785 [physics.space-ph] (cit. on p. 4).
23. Seidel, S. T.: ‘Eine Quelle für die Interferometrie mit Bose-Einstein-Kondensaten auf Höhenforschungsraketen’. Dissertation. Leibniz University Hannover, 2014 (cit. on pp. 4, 11, 21).

- 
24. Schlamminger, S., K.-Y. Choi, T. A. Wagner, J. H. Gundlach, and E. G. Adelberger: ‘Test of the Equivalence Principle Using a Rotating Torsion Balance’. *Phys. Rev. Lett.* (4 Jan. 2008), vol. 100: p. 041101. DOI: 10.1103/PhysRevLett.100.041101 (cit. on p. 4).
  25. Williams, J. G., S. G. Turyshev, and D. H. Boggs: ‘Lunar laser ranging tests of the equivalence principle’. *Classical and Quantum Gravity* (Aug. 2012), vol. 29(18): p. 184004. DOI: 10.1088/0264-9381/29/18/184004 (cit. on p. 4).
  26. Peters, A., K. Y. Chung, and S. Chu: ‘Measurement of gravitational acceleration by dropping atoms’. *Nature* (1999), vol. 400(6747): pp. 849–852. DOI: 10.1038/23655 (cit. on p. 4).
  27. Merlet, S. et al.: ‘Comparison between two mobile absolute gravimeters: optical versus atomic interferometers’. *Metrologia* (June 2010), vol. 47(4): pp. L9–L11. DOI: 10.1088/0026-1394/47/4/101 (cit. on p. 4).
  28. Zhou, L. et al.: ‘Test of Equivalence Principle at  $10^{-8}$  Level by a Dual-Species Double-Diffraction Raman Atom Interferometer’. *Phys. Rev. Lett.* (1 July 2015), vol. 115: p. 013004. DOI: 10.1103/PhysRevLett.115.013004 (cit. on p. 4).
  29. Fray, S., C. A. Diez, T. W. Hänsch, and M. Weitz: ‘Atomic Interferometer with Amplitude Gratings of Light and Its Applications to Atom Based Tests of the Equivalence Principle’. *Phys. Rev. Lett.* (24 Dec. 2004), vol. 93: p. 240404. DOI: 10.1103/PhysRevLett.93.240404 (cit. on p. 4).
  30. Bonnin, A., N. Zahzam, Y. Bidel, and A. Bresson: ‘Simultaneous dual-species matter-wave accelerometer’. *Phys. Rev. A* (4 Oct. 2013), vol. 88: p. 043615. DOI: 10.1103/PhysRevA.88.043615 (cit. on p. 4).
  31. Asenbaum, P., C. Overstreet, M. Kim, J. Curti, and M. A. Kasevich: *Atom-interferometric test of the equivalence principle at the  $10^{-12}$  level*. 2020. arXiv: 2005.11624 [physics.atom-ph] (cit. on p. 4).
  32. Thomas, V., N. Prasad, and C. Reddy: ‘Microgravity research platforms - A study’. *Current science* (Aug. 2000), vol. 79: pp. 336–340 (cit. on p. 5).
  33. Louchet-Chauvet, A. et al.: ‘The influence of transverse motion within an atomic gravimeter’. *New Journal of Physics* (June 2011), vol. 13(6): p. 065025. DOI: 10.1088/1367-2630/13/6/065025 (cit. on p. 5).
  34. Schkolnik, V., B. Leykauf, M. Hauth, C. Freier, and A. Peters: ‘The effect of wavefront aberrations in atom interferometry’. *Applied Physics B* (2015), vol. 120(2): pp. 311–316. DOI: 10.1007/s00340-015-6138-5 (cit. on p. 5).
  35. Anderson, M. H., J. R. Ensher, M. R. Matthews, C. E. Wieman, and E. A. Cornell: ‘Observation of Bose-Einstein Condensation in a Dilute Atomic Vapor’. *Science* (1995), vol. 269(5221): pp. 198–201. DOI: 10.1126/science.269.5221.198 (cit. on p. 5).

36. Davis, K. B. et al.: ‘Bose-Einstein Condensation in a Gas of Sodium Atoms’. *Phys. Rev. Lett.* (22 Nov. 1995), vol. 75: pp. 3969–3973. DOI: 10.1103/PhysRevLett.75.3969 (cit. on p. 5).
37. Müntinga, H. et al.: ‘Interferometry with Bose-Einstein Condensates in Microgravity’. *Phys. Rev. Lett.* (9 Feb. 2013), vol. 110: p. 093602. DOI: 10.1103/PhysRevLett.110.093602 (cit. on pp. 5–7).
38. Rudolph, J. et al.: ‘A high-flux BEC source for mobile atom interferometers’. *New Journal of Physics* (June 2015), vol. 17(6): p. 065001. DOI: 10.1088/1367-2630/17/6/065001 (cit. on pp. 5, 7, 11).
39. Pahl, J. et al.: ‘Compact and robust diode laser system technology for dual-species ultracold atom experiments with rubidium and potassium in microgravity’. *Appl. Opt.* (July 2019), vol. 58(20): pp. 5456–5464. DOI: 10.1364/AO.58.005456 (cit. on p. 5).
40. Frye, K. et al.: *The Bose-Einstein Condensate and Cold Atom Laboratory*. Submitted for publication in European Physical Journal Quantum Technology. 2019. arXiv: 1912.04849 [physics.atom-ph] (cit. on pp. 6, 8, 53, 54).
41. Touboul, P. et al.: ‘MICROSCOPE Mission: First Results of a Space Test of the Equivalence Principle’. *Phys. Rev. Lett.* (23 Dec. 2017), vol. 119: p. 231101. DOI: 10.1103/PhysRevLett.119.231101 (cit. on p. 6).
42. Barrett, B. et al.: ‘Dual matter-wave inertial sensors in weightlessness’. *Nature Communications* (Dec. 2016), vol. 7: p. 13786 (cit. on p. 6).
43. Geiger, R. et al.: ‘Detecting inertial effects with airborne matter-wave interferometry’. *Nature Communications* (Sept. 2011), vol. 2: p. 474 (cit. on p. 6).
44. Elliott, E. R., M. C. Krutzik, J. R. Williams, R. J. Thompson, and D. C. Aveline: ‘NASA’s Cold Atom Lab (CAL): system development and ground test status’. *npj Microgravity* (2018), vol. 4(1): p. 16. DOI: 10.1038/s41526-018-0049-9 (cit. on pp. 6, 12).
45. Aveline, D. C. et al.: ‘Observation of Bose-Einstein condensates in an Earth-orbiting research lab’. *Nature* (2020), vol. 582(7811): pp. 193–197. DOI: 10.1038/s41586-020-2346-1 (cit. on p. 6).
46. Le Coq, Y., J. A. Retter, S. Richard, A. Aspect, and P. Bouyer: ‘Coherent matter wave inertial sensors for precision measurements in space’. *Applied Physics B* (2006), vol. 84(4): pp. 627–632. DOI: 10.1007/s00340-006-2363-2 (cit. on p. 6).
47. Selig, H., H. Dittus, and C. Lämmerzahl: ‘Drop Tower Microgravity Improvement Towards the Nano-g Level for the MICROSCOPE Payload Tests’. *Microgravity Science and Technology* (2010), vol. 22(4): pp. 539–549. DOI: 10.1007/s12217-010-9210-0 (cit. on p. 7).
48. Zoest, T. van et al.: ‘Bose-Einstein Condensation in Microgravity’. *Science* (2010), vol. 328(5985): pp. 1540–1543. DOI: 10.1126/science.1189164 (cit. on p. 7).



- 
49. Hänsel, W., P. Hommelhoff, T. W. Hänsch, and J. Reichel: ‘Bose–Einstein condensation on a microelectronic chip’. *Nature* (2001), vol. 413(6855): pp. 498–501. DOI: 10.1038/35097032 (cit. on p. 7).
  50. Chu, S., J. E. Bjorkholm, A. Ashkin, J. P. Gordon, and L. W. Hollberg: ‘Proposal for optically cooling atoms to temperatures of the order of  $10^{-6}$  K’. *Opt. Lett.* (Feb. 1986), vol. 11(2): pp. 73–75. DOI: 10.1364/OL.11.000073 (cit. on p. 7).
  51. Ammann, H. and N. Christensen: ‘Delta Kick Cooling: A New Method for Cooling Atoms’. *Phys. Rev. Lett.* (11 Mar. 1997), vol. 78: pp. 2088–2091. DOI: 10.1103/PhysRevLett.78.2088 (cit. on p. 7).
  52. Morinaga, M., I. Bouchoule, J.-C. Karam, and C. Salomon: ‘Manipulation of Motional Quantum States of Neutral Atoms’. *Phys. Rev. Lett.* (20 Nov. 1999), vol. 83: pp. 4037–4040. DOI: 10.1103/PhysRevLett.83.4037 (cit. on p. 7).
  53. Abend, S. et al.: ‘Atom-Chip Fountain Gravimeter’. *Phys. Rev. Lett.* (20 Nov. 2016), vol. 117: p. 203003. DOI: 10.1103/PhysRevLett.117.203003 (cit. on p. 7).
  54. Becker, D. et al.: ‘Space-borne Bose–Einstein condensation for precision interferometry’. *Nature* (2018), vol. 562(7727): pp. 391–395. DOI: 10.1038/s41586-018-0605-1 (cit. on p. 7).
  55. Piest, B. et al.: ‘MAIUS-B: A system for two-species atom interferometry in space’. *ESA Symposium on European ROCKET & BALLOON programmes and related research*. Essen, Germany, 2019 (cit. on pp. 7, 11, 17).
  56. Elsen, M. et al.: *Towards a Dual-Species Atom Interferometer Payload for Operation on Sounding Rockets*. In preparation. 2020 (cit. on pp. 7, 11, 17).
  57. Lezius, M. et al.: ‘Space-borne frequency comb metrology’. *Optica* (Dec. 2016), vol. 3(12): pp. 1381–1387. DOI: 10.1364/OPTICA.3.001381 (cit. on p. 8).
  58. Dinkelaker, A. N. et al.: ‘Autonomous frequency stabilization of two extended-cavity diode lasers at the potassium wavelength on a sounding rocket’. *Appl. Opt.* (Feb. 2017), vol. 56(5): pp. 1388–1396. DOI: 10.1364/AO.56.001388 (cit. on p. 8).
  59. Prevedelli, M. et al.: ‘Trapping and cooling of potassium isotopes in a double-magneto-optical-trap apparatus’. *Phys. Rev. A* (1 Jan. 1999), vol. 59: pp. 886–888. DOI: 10.1103/PhysRevA.59.886 (cit. on p. 12).
  60. Lett, P. D. et al.: ‘Observation of Atoms Laser Cooled below the Doppler Limit’. *Phys. Rev. Lett.* (2 July 1988), vol. 61: pp. 169–172. DOI: 10.1103/PhysRevLett.61.169 (cit. on p. 12).
  61. Landini, M. et al.: ‘Sub-Doppler laser cooling of potassium atoms’. *Phys. Rev. A* (4 Oct. 2011), vol. 84: p. 043432. DOI: 10.1103/PhysRevA.84.043432 (cit. on p. 12).
  62. Palmerio, A. F., J. P. C. Peres da Silva, P. Turner, and W. Jung: ‘The development of the VSB-30 sounding rocket vehicle’. 2003: pp. 137–140 (cit. on p. 12).

63. Stamminger, A. et al.: ‘MAIUS-1- Vehicle, Subsystems Design and Mission Operations’. *22nd ESA Symposium on European Rocket and Balloon Programmes and Related Research*. Ed. by Ouwehand, L. Vol. 730. ESA Special Publication. Sept. 2015: p. 183 (cit. on pp. 12, 95).
64. Garcia, A. et al.: ‘VSB-30 sounding rocket: history of flight performance’. *Journal of Aerospace Technology and Management* (2011), vol. 3(3): pp. 325–330. DOI: 10.5028/jatm.2011. (cit. on p. 13).
65. Palmerio, A. F., E. D. Roda, P. Turner, and W. Jung: ‘Results from the first flight of the VSB-30 sounding rocket’. 2005: pp. 345–349 (cit. on p. 13).
66. Grosse, J.: ‘Thermal and Mechanical Design and Simulation for the first High Precision Quantum Optics Experiment on a Sounding Rocket’. Dissertation. University of Bremen, 2016 (cit. on pp. 13, 19).
67. Duarte, J. A. A., J. G. Damilano, F. E. de Almeida, and P. K. Odaguiri: ‘Flight data used on the evaluation of the acceptance testing specifications for the VSB-30 sounding rocket’. *17th ESA Symposium on European Rocket and Balloon Programmes and Related Research*. Ed. by Warmbein, B. Vol. 590. ESA Special Publication. Aug. 2005: pp. 351–355 (cit. on pp. 14, 15).
68. Grosse, J. Personal conversation. Oct. 2018 (cit. on p. 15).
69. Elsen, M. et al.: ‘Final Design of the MAIUS-2/-3 Payload - An Atom Interferometer on a Sounding Rocket’. *International Astronautical Congress (IAC)*. Bremen, Germany, 2018 (cit. on pp. 16–18).
70. Grosse, J. et al.: ‘Design and qualification of an UHV system for operation on sounding rockets’. *Journal of Vacuum Science & Technology A* (2016), vol. 34(3): p. 031606. DOI: 10.1116/1.4947583 (cit. on p. 18).
71. Metcalf, H. J. and P. van der Straten: *Laser Cooling and Trapping*. Springer, New York, 1999 (cit. on pp. 18, 36).
72. Dieckmann, K., R. J. C. Spreeuw, M. Weidemüller, and J. T. M. Walraven: ‘Two-dimensional magneto-optical trap as a source of slow atoms’. *Phys. Rev. A* (5 Nov. 1998), vol. 58: pp. 3891–3895. DOI: 10.1103/PhysRevA.58.3891 (cit. on p. 18).
73. Corgier, R. et al.: ‘Fast manipulation of Bose–Einstein condensates with an atom chip’. *New Journal of Physics* (May 2018), vol. 20(5): p. 055002. DOI: 10.1088/1367-2630/aabdfc (cit. on p. 18).
74. Reichel, J., W. Hänsel, and T. W. Hänsch: ‘Atomic Micromanipulation with Magnetic Surface Traps’. *Phys. Rev. Lett.* (17 Oct. 1999), vol. 83: pp. 3398–3401. DOI: 10.1103/PhysRevLett.83.3398 (cit. on p. 18).
75. Giese, E., A. Roura, G. Tackmann, E. M. Rasel, and W. P. Schleich: ‘Double Bragg diffraction: A tool for atom optics’. *Phys. Rev. A* (5 Nov. 2013), vol. 88: p. 053608. DOI: 10.1103/PhysRevA.88.053608 (cit. on p. 18).
76. Ahlers, H. et al.: ‘Double Bragg Interferometry’. *Phys. Rev. Lett.* (17 Apr. 2016), vol. 116: p. 173601. DOI: 10.1103/PhysRevLett.116.173601 (cit. on p. 18).

- 
77. Lévêque, T., A. Gauguet, F. Michaud, F. Pereira Dos Santos, and A. Landragin: ‘Enhancing the Area of a Raman Atom Interferometer Using a Versatile Double-Diffraction Technique’. *Phys. Rev. Lett.* (8 Aug. 2009), vol. 103: p. 080405. DOI: 10.1103/PhysRevLett.103.080405 (cit. on p. 18).
  78. Kubelka-Lange, A. et al.: ‘A three-layer magnetic shielding for the MAIUS-1 mission on a sounding rocket’. *Review of Scientific Instruments* (2016), vol. 87(6): p. 063101. DOI: 10.1063/1.4952586 (cit. on p. 19).
  79. Döringshoff, K., M. Mihm, A. Wenzlawski, O. Hellmig, and C. Kürbis: *Laser system for dual species atom-interferometry with Rubidium and Potassium on a sounding rocket*. In preparation. 2020 (cit. on pp. 22, 24).
  80. Wicht, A. et al.: ‘Narrow linewidth diode laser modules for quantum optical sensor applications in the field and in space’. *Components and Packaging for Laser Systems III*. Ed. by Glebov, A. L. and P. O. Leisher. Vol. 10085. International Society for Optics and Photonics. SPIE, 2017: pp. 103–118. DOI: 10.1117/12.2253655 (cit. on p. 23).
  81. Kürbis, C. et al.: ‘Extended cavity diode laser master-oscillator-power-amplifier for operation of an iodine frequency reference on a sounding rocket’. *Appl. Opt.* (Jan. 2020), vol. 59(2): pp. 253–262. DOI: 10.1364/AO.379955 (cit. on pp. 23, 36).
  82. Schiemangk, M. et al.: ‘High-power, micro-integrated diode laser modules at 767 and 780 nm for portable quantum gas experiments’. *Appl. Opt.* (June 2015), vol. 54(17): pp. 5332–5338. DOI: 10.1364/AO.54.005332 (cit. on p. 23).
  83. *Directional fiber optic power monitors*. OZ Optics Ltd. 2018. URL: [http://www.ozoptics.com/ALLNEW\\_PDF/DTS0042.pdf](http://www.ozoptics.com/ALLNEW_PDF/DTS0042.pdf) (visited on 04/21/2020) (cit. on p. 23).
  84. Bach, H. and D. Krause, eds.: *Low Thermal Expansion Glass Ceramics*. Second Edition. Schott Series on Glass and Glass Ceramics. Springer Berlin Heidelberg, 2005 (cit. on pp. 25, 45).
  85. *ZERODUR® Zero Expansion Glass Ceramic*. SCHOTT AG. URL: [https://www.schott.com/d/advanced\\_optics/f7ae3c11-0226-4808-90c7-59d6c8816daf/1.3/schott\\_zerodur\\_katalog\\_july\\_2011\\_en.pdf](https://www.schott.com/d/advanced_optics/f7ae3c11-0226-4808-90c7-59d6c8816daf/1.3/schott_zerodur_katalog_july_2011_en.pdf) (visited on 04/09/2020) (cit. on p. 25).
  86. *Thermal Expansion of ZERODUR®*. SCHOTT AG. URL: [https://www.schott.com/d/advanced\\_optics/4f6298b5-9f89-4da8-8d8c-3e5190dca4b4/1.3/schott-zerodur-cte-classes-may-2013-eng.pdf](https://www.schott.com/d/advanced_optics/4f6298b5-9f89-4da8-8d8c-3e5190dca4b4/1.3/schott-zerodur-cte-classes-may-2013-eng.pdf) (visited on 06/15/2020) (cit. on p. 25).
  87. Gwo, D.-H.: *Ultra precision and reliable bonding method*. US Patent 6,284,085 B1. 2001 (cit. on p. 25).
  88. Gwo, D.-H.: *Hydroxide-catalyzed bonding*. US Patent 6,548,176 B1. 2003 (cit. on p. 25).
  89. Gwo, D.-H. et al.: ‘The Gravity Probe-B star-tracking telescope’. *Advances in Space Research* (2003), vol. 32(7). Fundamental Physics in Space: pp. 1401–1405. DOI: [https://doi.org/10.1016/S0273-1177\(03\)90353-X](https://doi.org/10.1016/S0273-1177(03)90353-X) (cit. on p. 25).

90. Robertson, D. I. et al.: ‘Construction and testing of the optical bench for LISA Pathfinder’. *Classical and Quantum Gravity* (Mar. 2013), vol. 30(8): p. 085006. DOI: 10.1088/0264-9381/30/8/085006 (cit. on p. 25).
91. Schwarze, T. S. et al.: ‘Picometer-Stable Hexagonal Optical Bench to Verify LISA Phase Extraction Linearity and Precision’. *Phys. Rev. Lett.* (8 Feb. 2019), vol. 122: p. 081104. DOI: 10.1103/PhysRevLett.122.081104 (cit. on p. 25).
92. Elliffe, E. J. et al.: ‘Hydroxide-catalysis bonding for stable optical systems for space’. *Classical and Quantum Gravity* (Apr. 2005), vol. 22(10): S257–S267. DOI: 10.1088/0264-9381/22/10/018 (cit. on p. 25).
93. Ressel, S. et al.: ‘Ultrastable assembly and integration technology for ground- and space-based optical systems’. *Appl. Opt.* (Aug. 2010), vol. 49(22): pp. 4296–4303. DOI: 10.1364/AO.49.004296 (cit. on p. 25).
94. Gohlke, M. et al.: ‘Adhesive Bonding for Optical Metrology Systems in Space Applications’. *Journal of Physics: Conference Series* (May 2015), vol. 610: p. 012039. DOI: 10.1088/1742-6596/610/1/012039 (cit. on p. 25).
95. Schkolnik, V. et al.: ‘JOKARUS - design of a compact optical iodine frequency reference for a sounding rocket mission’. *EPJ Quantum Technology* (2017), vol. 4(1): p. 9. DOI: 10.1140/epjqt/s40507-017-0063-y (cit. on p. 25).
96. Döringshoff, K. et al.: ‘Iodine Frequency Reference on a Sounding Rocket’. *Phys. Rev. Applied* (5 May 2019), vol. 11: p. 054068. DOI: 10.1103/PhysRevApplied.11.054068 (cit. on p. 25).
97. Drougakis, G. et al.: ‘Precise and robust optical beam steering for space optical instrumentation’. *CEAS Space Journal* (2019), vol. 11(4): pp. 589–595. DOI: 10.1007/s12567-019-00271-x (cit. on p. 25).
98. Schkolnik, V. et al.: ‘A compact and robust diode laser system for atom interferometry on a sounding rocket’. *Applied Physics B* (2016), vol. 122(8): p. 217. DOI: 10.1007/s00340-016-6490-0 (cit. on p. 26).
99. Bach, H. and N. Neuroth, eds.: *The Properties of Optical Glass*. Schott Series on Glass and Glass Ceramics. Springer Berlin Heidelberg, 1998 (cit. on p. 27).
100. Adams, C. S. and I. G. Hughes: *Optics 2f*. Oxford University Press, 2019 (cit. on p. 28).
101. *D-ZLaF52LA*. CDGM Glass. URL: <http://www.cdgm.com/webapp/pdf/D-ZLaF52LA.pdf> (visited on 07/02/2020) (cit. on p. 28).
102. *Molded Glass Aspheric Lenses*. Thorlabs, Inc. URL: <https://www.thorlabs.de/thorproduct.cfm?partnumber=355230-B> (visited on 07/30/2020) (cit. on p. 28).
103. Marcuse, D.: ‘Loss analysis of single-mode fiber splices’. *The Bell System Technical Journal* (1977), vol. 56(5): pp. 703–718 (cit. on p. 28).
104. Marburger, J. P. et al.: *Determining the stability and coupling efficiency degradation of ultrastable optical benches under load*. Submitted for publication in Review of Scientific Instruments. 2020 (cit. on p. 28).

- 
105. Franzen, A.: *ComponentLibrary*. Licensed under a Creative Commons Attribution-NonCommercial 3.0 Unported License: <https://creativecommons.org/licenses/by-nc/3.0/>. 2006. URL: <http://www.gwoptics.org/ComponentLibrary/> (cit. on pp. 29, 30).
  106. Bjorklund, G. C., M. D. Levenson, W. Lenth, and C. Ortiz: ‘Frequency modulation (FM) spectroscopy’. *Applied Physics B* (1983), vol. 32(3): pp. 145–152. DOI: 10.1007/BF00688820 (cit. on p. 32).
  107. Drever, R. W. P. et al.: ‘Laser phase and frequency stabilization using an optical resonator’. *Applied Physics B* (1983), vol. 31(2): pp. 97–105. DOI: 10.1007/BF00702605 (cit. on p. 32).
  108. Black, E. D.: ‘An introduction to Pound–Drever–Hall laser frequency stabilization’. *American Journal of Physics* (2001), vol. 69(1): pp. 79–87. DOI: 10.1119/1.1286663 (cit. on p. 32).
  109. Mudarikwa, L., K. Pahwa, and J. Goldwin: ‘Sub-Doppler modulation spectroscopy of potassium for laser stabilization’. *Journal of Physics B: Atomic, Molecular and Optical Physics* (Mar. 2012), vol. 45(6): p. 065002. DOI: 10.1088/0953-4075/45/6/065002 (cit. on pp. 32, 34).
  110. McCarron, D. J., S. A. King, and S. L. Cornish: ‘Modulation transfer spectroscopy in atomic rubidium’. *Measurement Science and Technology* (Aug. 2008), vol. 19(10): p. 105601. DOI: 10.1088/0957-0233/19/10/105601 (cit. on p. 32).
  111. Zhang, J., D. Wei, C. Xie, and K. Peng: ‘Characteristics of absorption and dispersion for rubidium D2 lines with the modulation transfer spectrum’. *Opt. Express* (June 2003), vol. 11(11): pp. 1338–1344. DOI: 10.1364/OE.11.001338 (cit. on p. 32).
  112. Noh, H.-R., S. E. Park, L. Z. Li, J.-D. Park, and C.-H. Cho: ‘Modulation transfer spectroscopy for  $^{87}\text{Rb}$  atoms: theory and experiment’. *Opt. Express* (Nov. 2011), vol. 19(23): pp. 23444–23452. DOI: 10.1364/OE.19.023444 (cit. on p. 32).
  113. Nakanishi, S., H. Ariki, H. Itoh, and K. Kondo: ‘Frequency-modulation spectroscopy of rubidium atoms with an AlGaAs diode laser’. *Opt. Lett.* (Nov. 1987), vol. 12(11): pp. 864–866. DOI: 10.1364/OL.12.000864 (cit. on p. 32).
  114. Lampmann, K.: ‘Entwicklung hochstabiler Lasertechnologie für Weltraumanwendungen’. Dissertation. Johannes Gutenberg University Mainz, 2019 (cit. on p. 35).
  115. Tiecke, T.: *Properties of Potassium*. Version 1.03, June 2019. URL: <https://tobiastiecke.nl/archive/PotassiumProperties.pdf> (visited on 08/14/2020) (cit. on p. 36).
  116. Steck, D. A.: *Rubidium 85 D Line Data*. Version 2.2.1, 21 November 2019. URL: <https://steck.us/alkalidata/rubidium85numbers.pdf> (visited on 08/14/2020) (cit. on p. 36).
  117. Riley, W. and Physics Laboratory (U.S.). Time and Frequency Division: *Handbook of Frequency Stability Analysis*. NIST special publication. U.S. Department of Commerce, National Institute of Standards and Technology, 2008 (cit. on p. 37).

118. Larouche, S. and L. Martinu: ‘OpenFilters: open-source software for the design, optimization, and synthesis of optical filters’. *Appl. Opt.* (May 2008), vol. 47(13): pp. C219–C230. DOI: 10.1364/AO.47.00C219 (cit. on p. 39).
119. Boles, S.: ‘Zerodur based Vacuum Systems for Quantum Technology Applications’. Master thesis. Johannes Gutenberg University Mainz, 2019 (cit. on pp. 45–47, 50, 51).
120. Mihm, M. et al.: ‘Stable optical and vacuum systems for quantum technology applications in space’. *International Astronautical Congress (IAC)*. Washington, D.C., United States, 2019 (cit. on pp. 45, 48–50).
121. *Vacuum technology — Vocabulary — Part 1: General terms*. ISO 3529-1:2019. 2019 (cit. on p. 45).
122. Weng, K. et al.: ‘Compact magneto-optical trap with a quartz vacuum chamber for miniature gravimeters’. *J. Opt. Soc. Am. B* (June 2020), vol. 37(6): pp. 1637–1642. DOI: 10.1364/JOSAB.390512 (cit. on p. 45).
123. Heo, M. et al.: ‘Continuous cold atomic beam in a Zerodur chamber for atom interferometry’. *2017 Joint Conference of the European Frequency and Time Forum and IEEE International Frequency Control Symposium (EFTF/IFCS)*. July 2017: pp. 629–630. DOI: 10.1109/FCS.2017.8088981 (cit. on p. 45).
124. Biedermann, G.: ‘Gravity tests, differential accelerometry and interleaved clocks with cold atom interferometers’. Dissertation. Stanford University, 2007 (cit. on p. 45).
125. Rushton, J. A., M. Aldous, and M. D. Himsforth: ‘Contributed Review: The feasibility of a fully miniaturized magneto-optical trap for portable ultracold quantum technology’. *Review of Scientific Instruments* (2014), vol. 85(12): p. 121501. DOI: 10.1063/1.4904066 (cit. on p. 45).
126. Schwindt, P. D. D. et al.: ‘A highly miniaturized vacuum package for a trapped ion atomic clock’. *Review of Scientific Instruments* (2016), vol. 87(5): p. 053112. DOI: 10.1063/1.4948739 (cit. on p. 45).
127. Jedamzik, R. and T. Westerhoff: ‘Advices for the use of ZERODUR at higher temperatures’. *Advances in Optical and Mechanical Technologies for Telescopes and Instrumentation III*. Ed. by Navarro, R. and R. Geyl. Vol. 10706. International Society for Optics and Photonics. SPIE, 2018: pp. 924–933. DOI: 10.1117/12.2311648 (cit. on p. 47).
128. *Alkali Metal Dispensers*. SAES Getters Group. 2007. URL: [https://www.saesgetters.com/sites/default/files/AMD%20Brochure\\_0.pdf](https://www.saesgetters.com/sites/default/files/AMD%20Brochure_0.pdf) (visited on 04/03/2020) (cit. on p. 48).
129. *St 171<sup>®</sup> and St 172 - Sintered Porous Getters*. SAES Getters Group. 2007. URL: [https://www.saesgetters.com/sites/default/files/St%20171%20-%20172\\_Sintered%20Porous%20Getters\\_1.pdf](https://www.saesgetters.com/sites/default/files/St%20171%20-%20172_Sintered%20Porous%20Getters_1.pdf) (visited on 04/03/2020) (cit. on p. 49).
130. Barschke, M. F. et al.: ‘Optical Quantum Technology in Space using Small Satellites’. *International Astronautical Congress (IAC)*. Adelaide, Australia, 2017 (cit. on p. 53).

- 
131. Dinkelaker, A. N. et al.: ‘Optical Quantum Technologies for Compact Rubidium Vapor-cell Frequency Standards in Space Using Small Satellites’. *Journal of the British Interplanetary Society* (2019), vol. 72(3): pp. 74–82 (cit. on p. 53).
  132. Schmidt, P. O. et al.: ‘Spectroscopy Using Quantum Logic’. *Science* (2005), vol. 309(5735): pp. 749–752. DOI: 10.1126/science.1114375 (cit. on p. 54).
  133. Hannig, S.: ‘Development and characterization of a transportable aluminum ion quantum logic optical clock setup’. Dissertation. Leibniz University Hannover, 2018 (cit. on p. 54).
  134. Hannig, S. et al.: ‘Towards a transportable aluminium ion quantum logic optical clock’. *Review of Scientific Instruments* (2019), vol. 90(5): p. 053204. DOI: 10.1063/1.5090583 (cit. on pp. 54, 55).
  135. Wübbena, J. B., S. Amairi, O. Mandel, and P. O. Schmidt: ‘Sympathetic cooling of mixed-species two-ion crystals for precision spectroscopy’. *Phys. Rev. A* (4 Apr. 2012), vol. 85: p. 043412. DOI: 10.1103/PhysRevA.85.043412 (cit. on p. 54).
  136. Mehlstäubler, T. E., G. Grosche, C. Lisdat, P. O. Schmidt, and H. Denker: ‘Atomic clocks for geodesy’. *Reports on Progress in Physics* (Apr. 2018), vol. 81(6): p. 064401. DOI: 10.1088/1361-6633/aab409 (cit. on p. 55).
  137. Hannig, S. et al.: *Zerodur-based Optical Systems for Transportable Quantum Sensors in the UV*. In preparation. 2020 (cit. on p. 59).





---

## List of Figures

---

1.1	Building blocks of an atom interferometer . . . . .	3
1.2	Space missions of the QUANTUS consortium with (scheduled) launch dates	8
2.1	Illustration of main flight events . . . . .	13
2.2	Accelerations and Rotation rate during the launch phase of MAIUS-1 . . .	15
2.3	Payload accelerations during the re-entry of MAIUS-1 . . . . .	15
2.4	CAD rendering of the scientific payload for MAIUS-2/-3 . . . . .	17
2.5	CAD rendering of the physics package for MAIUS-2/-3 . . . . .	18
3.1	Schematic structure of the laser system for MAIUS-2/-3 . . . . .	22
3.2	CAD rendering of the laser system for MAIUS-2/-3 . . . . .	24
3.3	The required power ratio of the $2D^+$ MOT cannot be realized by splitters .	27
3.4	Schematic layouts of the optical modules on the Zerodur level . . . . .	29
3.5	Photo of one scientific module together with its schematic layout . . . . .	30
3.6	Technical drawing of the single-input modules with marked beam paths . .	30
3.7	Schematic MTS setup and signals using potassium as example . . . . .	33
3.8	Schematic FMS setup and signals using potassium as example . . . . .	34
3.9	Photo of the frequency reference modules for MAIUS-2/-3 . . . . .	35
3.10	Normalized excitation rate of a two-level system as a function of detuning .	36
3.11	Allan deviations of the reference systems for MAIUS-2/-3 . . . . .	37
3.12	Schematic top view and photo of the beam separator . . . . .	38
3.13	Unwanted reflections of the beam separator . . . . .	38
3.14	Calculated and measured transmittance spectrum of the beam separator . .	39
4.1	Setup for simultaneous MTS of the K $D_1$ , $D_2$ and Rb $D_2$ transitions . . . . .	42
4.2	Modulation frequencies and filter spectra to separate PD signals . . . . .	42
4.3	Simultaneous MTS signals of the K $D_1$ , $D_2$ and Rb $D_2$ transitions . . . . .	44
4.4	Illustration of the screw-based flange and photo of the Zerodur chamber . .	46
4.5	Illustration of the conical flange and photo of the Zerodur chamber . . . . .	47
4.6	Photo of the Zerodur MOT chamber body . . . . .	48
4.7	Photo of the two inlets with mounted AMDs and NEGs . . . . .	49
4.8	Photo of the Zerodur MOT chamber with mounted AMDs . . . . .	50
4.9	Photo of the Zerodur MOT chamber's top window with insufficient sealing .	51
5.1	CAD rendering of the scientific Zerodur modules for BECCAL . . . . .	54
5.2	Reduced $^{40}\text{Ca}^+$ level scheme . . . . .	55

5.3	Photo of the Zerodur module for a transportable optical clock . . . . .	56
-----	---	----

---

## List of Tables

---

1.1	Overview of state of the art WEP test experiments . . . . .	4
1.2	Comparison of microgravity research platforms . . . . .	5
1.3	Overview of WEP test experiments on different microgravity platforms . . . .	6
2.1	Mechanical loads during launch and re-entry . . . . .	15
2.2	Thermal loads generated within the payload for MAIUS-2/-3 . . . . .	16
2.3	Power spectral densities and frequency ranges of vibration test levels . . . .	19
3.1	Optical powers required at the physics package for the 2D <sup>+</sup> MOT . . . . .	27
3.2	Estimated and measured power budget of beam path 1 of a single-input module	31
3.3	Estimated and measured power budget of beam path 2 of a single-input module	31
6.1	Milestones of the missions MAIUS-2/-3 with (scheduled) dates . . . . .	58
A.1	Main events of flight for MAIUS-1 . . . . .	95



## A Main flight events

**Table A.1:** Main events of flight with calculated times and altitudes for MAIUS-1 [63].

Event	Time in s	Altitude in km
Lift-off	0.0	0.33
Burnout of first stage	13.5	4.30
Ignition of second stage	15.0	5.00
Burnout of second stage	44.0	43.40
Yo-Yo de-spin	55.0	64.90
Nosecone ejection	58.0	70.56
Motor/payload separation	60.0	74.29
Attitude and rate control system on	61.0	
Beginning of microgravity phase	75.0	101.02
Attitude and rate control system off	91.0	
Attitude and rate control system on	180.0	
Attitude and rate control system off	190.0	
Payload apogee	260.0	258.30
Attitude and rate control system on	300.0	
Attitude and rate control system off	310.0	
Beginning of atmospheric re-entry	446.0	100.00
Maximum deceleration	487.0	27.00
Heat shield ejection and stab chute activation		4.70
Main parachute activation		2.90
Power-off for experiment	900.0	



## Curriculum vitae

### Personal details

Name	Moritz Mihm
Date of birth	03.03.1989
Place of birth	Kassel, Germany

### Postgraduate studies

Since 2015	Doctoral studies in physics, Johannes Gutenberg University, Mainz, Germany
2018	Graduate Certificate in Space Studies, University of South Australia, Adelaide, Australia
2011-2014	Master of Science in Physics, Georg-August University, Göttingen, Germany

### Undergraduate studies

2008-2011	Bachelor of Science in Physics, Georg-August University, Göttingen, Germany
-----------	---

### Formal education

1999-2008	Albert-Schweitzer-Schule, Kassel, Germany
-----------	---











